Theses and Dissertations

Fall 2012

Dynamic interactions of electromagnetic and mechanical fields in electrically conductive anisotropic composites

Amir Barakati
University of Iowa

www.manaraa.com

DYNAMIC INTERACTIONS OF ELECTROMAGNETIC AND MECHANICAL

FIELDS IN ELECTRICALLY CONDUCTIVE ANISOTROPIC COMPOSITES

by

Amir Barakati

<u>An Abstract</u>

Of a thesis submitted in partial fulfillment
of the requirements for the Doctor of
Philosophy degree in Mechanical Engineering
in the Graduate College of
The University of Iowa

December 2012

Thesis Supervisor: Assistant Professor Olesya I. Zhupanska

ABSTRACT

Recent advances in manufacturing of multifunctional materials have provided opportunities to develop structures that possess superior mechanical properties with other concurrent capabilities such as sensing, self-healing, electromagnetic and heat functionality. The idea is to fabricate components that can integrate multiple capabilities in order to develop lighter and more efficient structures. In this regard, due to their combined structural and electrical functionalities, electrically conductive carbon fiber reinforced polymer (CFRP) matrix composites have been used in a wide variety of applications in most of which they are exposed to unwanted impact-like mechanical loads. Experimental data have suggested that the application of an electromagnetic field at the moment of the impact can significantly reduce the damage in CFRP composites. However, the observations still need to be investigated carefully for practical applications. Furthermore, as the nature of the interactions between the electro-magneto-thermo-mechanical fields is very complicated, no analytical solutions can be found in the literature for the problem.

In the present thesis, the effects of coupling between the electromagnetic and mechanical fields in electrically conductive anisotropic composite plates are studied. In particular, carbon fiber polymer matrix (CFRP) composites subjected to an impact-like mechanical load, pulsed electric current, and immersed in the magnetic field of constant magnitude are considered. The analysis is based on simultaneous solving of the system of nonlinear partial differential equations, including equations of motion and Maxwell's equations. Physics-based hypotheses for electro-magneto-mechanical coupling in transversely isotropic composite plates and dimension reduction solution procedures for the nonlinear system of the governing equations have been used to reduce the three-dimensional system to a two-dimensional (2D) form. A numerical solution procedure for

the resulting 2D nonlinear mixed system of hyperbolic and parabolic partial differential equations has been developed, which consists of a sequential application of time and spatial integrations and quasilinearization. Extensive computational analysis of the response of the CFRP composite plates subjected to concurrent applications of different electromagnetic and mechanical loads has been conducted. The results of this work verify the results of the previous experimental studies on the subject and yield some suggestions for the characteristics of the electromagnetic load to create an optimum impact response of the composite.

Abstract Approved:_____

Thesis Supervisor

_____

Title and Department

_____

Date

DYNAMIC INTERACTIONS OF ELECTROMAGNETIC AND MECHANICAL

FIELDS IN ELECTRICALLY CONDUCTIVE ANISOTROPIC COMPOSITES

by

Amir Barakati

A thesis submitted in partial fulfillment
of the requirements for the Doctor of
Philosophy degree in Mechanical Engineering
in the Graduate College of
The University of Iowa

December 2012

Thesis Supervisor: Assistant Professor Olesya I. Zhupanska

Graduate College
The University of Iowa
Iowa City, Iowa

CERTIFICATE OF APPROVAL

_____

PH.D. THESIS

_____

This is to certify that the Ph.D. thesis of

Amir Barakati

has been approved by the Examining Committee
for the thesis requirement for the Doctor of
Philosophy degree in Mechanical Engineering at
the December 2012 graduation.

Thesis Committee: _____
                  Olesya I. Zhupanska, Thesis Supervisor

                  _____
                  Kyung K. Choi

                  _____
                  Jia Lu

                  _____
                  Shaoping Xiao

                  _____
                  M. Asghar Bhatti

To My Family

ii

ACKNOWLEDGMENTS

ABSTRACT

Recent advances in manufacturing of multifunctional materials have provided opportunities to develop structures that possess superior mechanical properties with other concurrent capabilities such as sensing, self-healing, electromagnetic and heat functionality. The idea is to fabricate components that can integrate multiple capabilities in order to develop lighter and more efficient structures. In this regard, due to their combined structural and electrical functionalities, electrically conductive carbon fiber reinforced polymer (CFRP) matrix composites have been used in a wide variety of applications in most of which they are exposed to unwanted impact-like mechanical loads. Experimental data have suggested that the application of an electromagnetic field at the moment of the impact can significantly reduce the damage in CFRP composites. However, the observations still need to be investigated carefully for practical applications. Furthermore, as the nature of the interactions between the electro-magneto-thermo-mechanical fields is very complicated, no analytical solutions can be found in the literature for the problem.

In the present thesis, the effects of coupling between the electromagnetic and mechanical fields in electrically conductive anisotropic composite plates are studied. In particular, carbon fiber polymer matrix (CFRP) composites subjected to an impact-like mechanical load, pulsed electric current, and immersed in the magnetic field of constant magnitude are considered. The analysis is based on simultaneous solving of the system of nonlinear partial differential equations, including equations of motion and Maxwell's equations. Physics-based hypotheses for electro-magneto-mechanical coupling in transversely isotropic composite plates and dimension reduction solution procedures for the nonlinear system of the governing equations have been used to reduce the three-dimensional system to a two-dimensional (2D) form. A numerical solution procedure for

iv

the resulting 2D nonlinear mixed system of hyperbolic and parabolic partial differential equations has been developed, which consists of a sequential application of time and spatial integrations and quasilinearization. Extensive computational analysis of the response of the CFRP composite plates subjected to concurrent applications of different electromagnetic and mechanical loads has been conducted. The results of this work verify the results of the previous experimental studies on the subject and yield some suggestions for the characteristics of the electromagnetic load to create an optimum impact response of the composite.

TABLE OF CONTENTS

LIST OF FIGURES

xi

xii

CHAPTER 1

INTRODUCTION

1.1 Background Information

Today's technology relies heavily on the use of the so-called hybrid materials that allow for achieving advanced structural and functional capabilities. In this respect, composite materials are particularly recognized as ones that have a significant impact on the development of a variety of industries, energy conservation efforts, and many other aspects of our lives. In particular, composite materials are widely used in the aerospace industry. Over the last several decades, major advances have been achieved in improving strength-to-weight and stiffness-to-weight ratios of aerospace structures through improvements in the material properties of composite constituents, manufacturing and fabrication techniques, as well as structural analysis and design optimization. As a result, significant cost savings were attained, for instance, in the space structures where the structural mass was reduced from more than 20% of the total mass to less than 5% of the total mass in the last several decades. At the same time, further improvements in structure weight savings due to the use of composite materials are limited, and new technologies are required for subsequent improvements in aerospace systems efficiency.

The next major breakthrough in aerospace technologies is anticipated to occur with the emergence of a new generation of multifunctional materials and structural systems, which are envisioned as being able to perform simultaneously a set of specialized functions, traditionally designated to separate subcomponents. Of particular interest to aerospace applications are materials that, in addition to carrying out structural functions, can provide sensing and self-healing capabilities, radiation and electromagnetic interference (EMI) protection, energy storage and conversion, damage

protection, vibrations damping, etc. Composite materials lend themselves naturally to the concept of multifunctionality because of their multiphase nature and inherent tailorability. At the same time, advancements in the design of the multifunctional composite structures require significant strengthening of the scientific base and expanding of our understanding of complex interactions of multiple physical phenomena, which lead to the desired multifunctionality. In this context, composite materials present rich possibilities for development of multifunctional and functionally adaptive structures where multifunctionality can be achieved through interaction of mechanical, electromagnetic, thermal, and other fields.

<u>1.2 Motivation</u>

This thesis is motivated by studies of Telitchev et al. [1, 2] and Sierakowski et al. [3], who investigated the impact response of electrified carbon fiber polymer matrix composites and showed that impact resistance of composites can be improved by subjecting them to electrical load at the moment of impact. It was noticed that the magnitude of the applied electric current had a considerable effect on the propagation of impact damage in the composite: the stronger was the applied current, the less impact damage was observed in the experiments. These experimental observations stimulated the present study on the modeling of dynamic interactions of electromagnetic and mechanical fields in anisotropic electrically conductive composites.

1.3 Thesis Objectives

The main goal of this thesis was to develop a mathematical framework and solution procedures for solving nonlinear coupled problems in electrically conductive anisotropic composites subjected to electromagnetic and mechanical fields.

Specific research objectives were the following:

1. To develop the mathematically rigorous formulation for the response of anisotropic electrically conductive composite plates subjected to dynamic mechanical and electromagnetic loads.

2. To develop efficient numerical solution procedures for solving nonlinear coupled dynamic problems in the anisotropic electrically conductive composite plates subjected to mechanical and electromagnetic loads.

3. To elucidate the effects of dynamic interactions of mechanical, electromagnetic, and associated thermal fields in carbon fiber polymer matrix composites through extensive computational analysis.

CHAPTER 2

LITERATURE REVIEW

2.1 Multifunctionality

Since the last decade, the tendency of the engineering community has turned towards the development of materials that have the capability of performing multiple tasks simultaneously and can be employed in different applications. The need of manufacturing such efficient multifunctional structures has resulted in developing advanced materials such as smart materials, Micro-Electro-Mechanicals systems (MEMs), multifunctional materials, nano-materials, bio-composites, environmentally-friendly composites, Nano-Electro-Mechanical systems (NEMs), etc. The efforts to develop high performance systems have been followed by two major criteria: attaining of maximum specific load-carrying capability and incorporation of multiple functionalities in the structure with minimum weight penalties. Apart from these two goals, engineers are also being challenged by the affordability and environmentally friendliness of products.

Multifunctional structures have been developed in desire to reach superior combinations of better performance, higher strength, and lower weight together with other specific properties such as corrosion resistance, energy absorption, sensing, heat resistance, radiation protection, thermal and electrical conductivity, power generation, and so forth. In other words, a single component is designed such that it can serve several primary functions simultaneously or sequentially, mainly to improve efficiency and reduce size and weight in critical systems by the elimination of redundancies. The major trusts in this area are in the direction of creating lighter and smaller automatic systems, adaptive structures and self-sustaining systems.

According to the definition, composite materials are the combination of at least two materials with different properties that form a new material with new desired properties which are not independently obtainable by each constituent. Taking into account the presence of discrete phases and the intrinsic anisotropy in such materials, it is reasonable to consider a composite or hybrid of several materials to have the tremendous potential to achieve multifunctionality. In other words, composites are ideal candidates for structural components with several integrated functionalities and it can be claimed that multifunctional materials have to be composite materials [4].

The integrated functionalities of the multifunctional materials can be categorized into multiple structural functionalities and the combination of structural and non-structural functionalities [4].

2.2 Multi-Structural Functionalities

In many applications, the structure needs to simultaneously provide a combination of two or multiple high level structural functions such as tensile/compression strength, fracture toughness, elastic modulus, interfacial and/or interlaminar shear strength, durability, vibration damping, oxidation resistance and so forth. For this purpose, the material can be constructed as conventional composites with micron-scale reinforcement or new mutiscale hybrid micro/nanocomposites which incorporate nano-reinforcements as well as conventional fiber or particle reinforcements [4].

In a wide variety of applications, structural damping is a critical issue to control the dynamic stability, increase the fatigue life, and improve maneuverability. Simultaneous improvements in laminate strength and stiffness as well as structural damping were reported by Koratkar et al. [5] by incorporating nanofilm inter-layers within a composite laminate. Each thin nanofilm is comprised of a dense network of

highly interlinked multi-walled carbon mamotubes (MWNTs) that fabricated employing the catalytic chemical vapor deposition (CVD) technique. The experiments on bending properties of the composite beam showed that the powerful interactions between the nanotube clusters produce significant energy dissipation which results in up to 200% increase in the structural damping. The bending stiffness is also improved about 30% due to the corsslinks between the MWNTs that simplify the load transferring within the films.

It is suggested to add nanoscale reinforcements to a polymer matrix to provide enhanced mechanical, electrical and thermal properties. In this respect, carbon nanotubes (CNTs), first discovered by Iijima [6], have been widely utilized in fabrication of nanocomposites due to their extraordinary properties such as high aspect ratio, high specific strength and stiffness, thermal and electrical conductivities, flexibility, exceptional resilience, high stability, etc. [7-11]. Carbon nanotubes are cylindrical sheets of graphite with a very high aspect ratio (>1000) that can be synthesized in two forms of single-walled and multi-walled [7, 12, 13]. The elastic modulus of CNTs can be five times of the modulus of steel [13-16], the tensile strength may be up to 200 times larger [13, 17, 18]. The thermal conductivity of MWNTs (about $3000\,\mathrm{W/mK}$ measured by Kim et al. [19]) can be more than seven times larger than that of copper while this value is more than sixteen times for SWNTs (about $6600\,\mathrm{W/mK}$ reported by Berber et al. [20]). Moreover, CNTs can be fabricated to be electrically semiconductive or conductive [13, 21]. The addition of very small amount of carbon nanotubes to a polymer matrix can considerably enhance the properties of the composite [16]. Moreover, the mechanical properties of a nanocomposite such as stiffness, yield strength and fracture toughness can be improved by increasing the CNT content [13], but this is not always effective [11, 16]. The stress transfer and failure mechanisms of such CNT-based composites are very complex and still under investigation although some aspects are comparable to those of fiber reinforced composites [22]. Furthermore, in order to take full advantage of the properties of CNTs, two main factors should be considered carefully during the

fabrication processing of nanocomposites: dispersion and alignment of the nanotubes in the matrix [23, 24]. It is important to homogenously disperse the carbon nanotubes throughout the matrix while the integrity of the CNTs is preserved [10, 11]. Moreover, the alignment of nanotubes can highly enhance some properties of the nanocomposite, especially the thermal and electrical conductivities. Nanotubes can be further aligned by employing some techniques such as magnetic field processing [24]. Allaoui et al. [16] demonstrated that increasing the content of carbon nanotubes in the random distribution form would not improve the mechanical properties of the polymer matrix.

By using nanoscale reinforcements in combination with microscale fibers, it is made possible for scientists to add the extraordinary properties of the nanomaterials to those of a conventional composite and obtain a multiscale hybrid composite material. In this regard, many researchers have investigated and proposed new techniques to grow carbon nanotubes on different substrates such as carbon fibers, carbon cloth, carbon mat/felt, graphite coil to fabricate new hybrid composites with desired properties [25-31]. It is proved that he amount and growth pattern of the CNTs introduced to the hybrid composite, which influence the mechanical behavior of the multiscale composite, highly depends on the type of the substrate [31]. Moreover, the interfacial bonding between the CNTs and the polymer matrix governs the effectiveness of the load transfer mechanism.

Figure 1 shows the scanning electron microscopy (SEM) and transmission electron microscopy (TEM) image of a uniform long and entangled MWNT layer grown on a carbon fiber at $900°C$.

An example of such attempts to tailor the mechanical properties of composites is the multiscale hybrid material developed by Thostenson et al. [32]. They used the chemical vapor decomposition (CVD) technique in order to grow carbon nanotubes on carbon fibers in a polymer matrix composite. They reported a 15% increase in the interfacial shear strength of the multiscale hybrid composite although the corresponding surface treatment with no nanotube growth results in a significant degradation in the

interface strength. This improvement was attributed to the increase in the fiber/matrix interface provided by the carbon nanotubes deposited on the fibers.
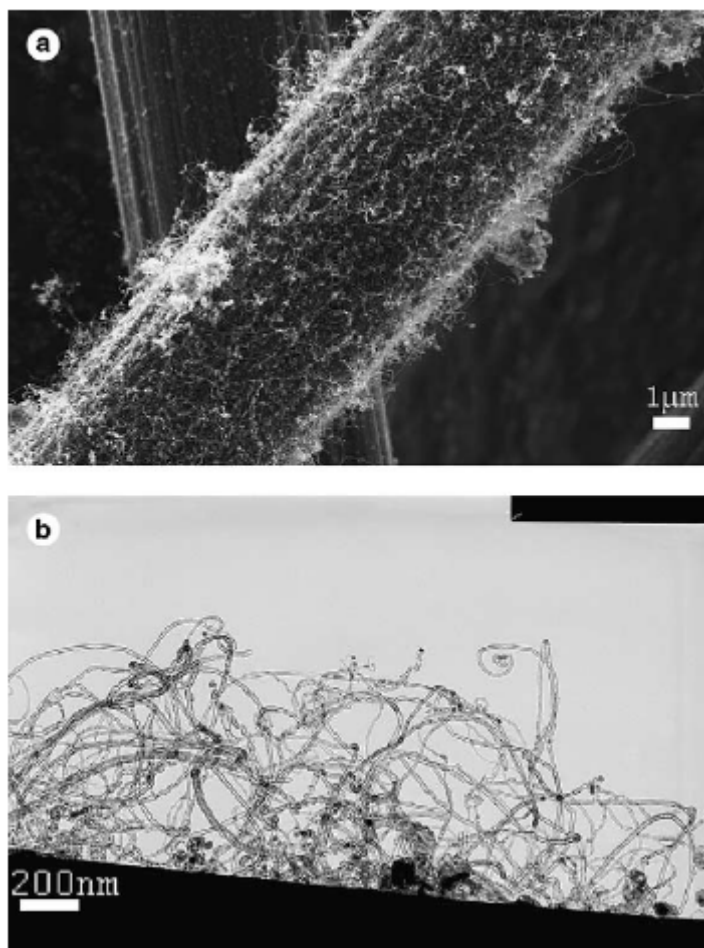
Figure 1. MWNTs grown on a carbon fiber (a) SEM and (b) TEM images

Source: Zhao, Z.G.; Ci, L.J.; Cheng, H.M.; Bai, J.B. *Carbon*, **2005**, *43(3)*, 663-665.

Another method to fabricate mutiscale hybrid composites is to replace the matrix with nanocomposite materials; for instance, Vlasveld et al. [33] developed a new three-phase hybrid composite which combined the novel properties of fibrous composites and

polymer nanocomposites (Fig. 2). In conventional unidirectional polymer matrix composites, the transverse properties which are dominated by the matrix are often poor. Therefore, Vlasveld et al. employed polymer nanocomposites instead of the conventional polymers to improve the matrix modulus and strength. The results they presented show significant improvement in flexural strength both for glass and carbon fiber hybrid composites. It is interesting to note that the increase in the high temperature and moisture-conditioned properties of the new composite can be achieved with no change in melting temperature and processing conditions.
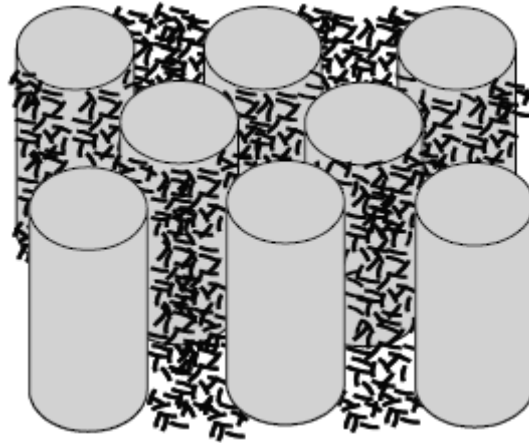
Figure 2. Schematic of a hybrid composite consisted of carbon fibers and a nanocomposite matrix

Source: Vlasveld, D.P.N.; Bersee, H.E.N.; Picken, S.J. *Polymer*, **2005**, *46(23)*, 10269-10278.

2.3 Integrated Structural and Non-Structural Functionalities

Another promising direction to achieve multifunctionality in the structures and reduce parasitic weight is to enhance structural and electromagnetic functionalities

simultaneously. In many applications, especially in aerospace industries, some parts need to be electrically conductive to provide electrostatic discharge (ESD), electromagnetic interference (EMI) shielding, or lightning strike protection. For instance, rather than using separate banks of capacitors in advanced aerospace systems to protect against power conditioning or rapid electrical discharge, significant weight saving can be achieved by employing multifunctional structural capacitors which simultaneously store electrostatic energy while carrying mechanical loads [34]. Good candidates for such multifunctional capacitors are polymer matrix composites with high dielectric constant ceramic fillers which offer excellent dielectric and mechanical properties by combining the advantages of their multiple phases [35-37]. In addition, dielectric and other properties can be designed for specific applications by various fabrication techniques such as adjusting the relative fraction of the composite constituents, treating the components with different chemical or physical methods and changing the processing conditions [38, 39].

As for electrostatic dissipation (ESD), electromagnetic interference (EMI) shielding, and lightning strike protection applications, the important material characteristic is electrical conductivity. The minimum requirement for the conductivity of the material to avoid electrostatic charging is 10^{-6} S/m [8]. Examples of conductive fillers for composite materials include metallic particles, carbon black, carbon nanotubes, and semiconductors. Recently, there is a growing tendency to use carbon nanotubes dispersed in polymer matrix composites instead of antistatic paints or adding conventional conductive fillers such as carbon black to an insulating matrix. The main reason is related to the high achievable electrical conductivity of the composite using very low volume fraction of CNTs [8, 40].

The conductivity of a polymer matrix composite material is a function of the volume fraction of the conductive filler. The percolation threshold predicts the minimum addition of conductive fillers to a non-conductive matrix in order to form a continuous

conductive network. Broadbent and Hammersley [41] were the first researchers who formally studied the percolation threshold and probability in 1957 and introduced a mathematical model of percolation threshold. Since then, many analytical and numerical studies have been proposed models for percolation thresholds in composites [41-42]. The CNT-reinforced nanocomposites possess much lower percolation threshold (as low as 0.0021 wt% [43]) than composites that contain other conventional fillers. This is related to the high aspect ratio and high specific surface area of CNTs [40]. Maximum conductivity of a CNT-reinforced polymer nanocomposite was reported for 10 wt% SWCNT-reinforced polymethylmethacrylate (PMMA) (about $10,000 \text{ S/m}$) [44]. It has been found that the percolation threshold of CNT-reinforced polymer matrix composites is mostly influenced by the aspect ratio, alignment and dispersion state of CNTS [40]. Kim et al. [23] used highly aligned CNTs to enhance the electrical conductivity and EMI shielding properties of a rubber sheet. Besides the electromagnetic properties, the elastic modulus and thermal conductivity of the rubber composite were improved as well.

Conductive nanocomposites find important applications in ESD, EMI shielding, and lightning strike protection. Electrostatic discharge is the transfer of static electric charge between bodies of different electrostatic potential which can be detrimental, e.g. for microchips during handling [45]. Furthermore, in many critical electronic devices, it is vital to reduce or eliminate the undesirable electromagnetic interference energy from external environment which might have an adverse effect on the performance of the electronic equipment. This suppression can be achieved by applying filtering or shielding in order to maintain the electromagnetic compatibility (EMC), which is defined as the capability of an electrical of electronic system to operate in its designed margin of safety [45]. With the rapid increase in the use of digital equipment and telecommunication, EMI shielding materials effectively limit the amount of the EMI radiation that penetrates into or escapes from an electronic circuit. In general, shielding effectiveness (SE), expressed in decibels (dB), is the main measure of shielding capability of the material used for EMI

shielding. It is defined as the ratio between the absolute value of the electric (or magnetic) field that is present at a given point beyond the shield and the absolute value of the electric (or magnetic) field that would have been present at the same point in the absence of the shield itself [45]. Traditional shielding materials include metallic, ferromagnetic, ferromagnetic, and ferroelectric materials [46]. Such materials have limitations such as heavy weight and low corrosion resistance. Nowadays, producing new materials that can offer other functionalities besides EMI shielding is an active field of research; among them, electrically conductive CNT-reinforced polymer matrix composites are among best options. The minimum shielding effectiveness for commercial applications is about 21 dB, while polymer matrix composite materials with conductive fillers can provide a shielding effectiveness of more than 40 dB [47].

Thermal protection is a critical issue in many applications including gas turbine blades [48], reentry space vehicles [49], electronic and optoelectronic devices [50]. There are different strategies to mitigate heat, among which are placement of thermal barriers [51], increasing thermal conductivity [52], and use of materials with low coefficient of thermal expansion [53].

Measurement of the thermal conductivity of micro/nanoscale materials is a challenging issue that has been studied in accord with the development of low-dimensional structures, such as carbon nanotubes, graphene, etc. Many techniques and approaches for accurate and high-resolution thermometry have been proposed in the literature [50, 54, 55].

One important feature of carbon nanotubes is their unusually high thermal conductivity [19, 20, 24, 56] that justifies the use of these nanoscale materials in new composites for advanced thermal management applications. Kim et al. [57] reached enhanced thermal conductivity in a carbon fiber polymer matrix composite by adding highly crystalline multi-walled carbon nanotubes (MWCNTs) as fillers. In fact, the nanotubes form thermal paths between adjacent carbon fibers and consequently, improve

the thermal conductivity of the multiscale composite. Similar improvement in thermal properties was observed by Biercuk et al. [9] in a single-walled carbon nanotubes (SWNTs) reinforced epoxy matrix composite. Ganguli et al. [58] studied the effects of chemically functionalization on exfoliated graphite filled epoxy composites. They reported a noticeable increase in thermal conductivity of the composite; however, the electrical properties of the material were deteriorated.

Structural health monitoring (SHM) is another application where functional capabilities of the materials are employed to assess the integrity of the structures. SHM is the process of acquisition and analysis of technical data for the purpose of damage detection in an engineering infrastructure in order to facilitate life-cycle management [59, 60]. In many cases, the damage caused by low-velocity impact is barely visible (known as barely visible impact damage or BVID) and cannot be easily detected. This is especially true for laminated composite materials since impact damage usually occurs in inner plies while the outer layers seem to be completely undamaged on visual inspection. To detect damage in such cases, various nondestructive evaluation techniques (NDT) and structural health monitoring systems such as X-ray, hydro-ultrasonics (C-scan), shearography, thermography and acoustic emission technique are employed [59, 61]. The inspection methods may be active, semiactive, passive, or hybrid [62]. Capezzuto et al. [61] developed a new smart multifunctional polymer nanocomposite layer that shows visible light emission when subjected to different wavelength UV-light excitation. Besides the electromagnetic functionality of the layer, it can be used to perform structural health monitoring in carbon fiber and sandwich composites as it can detect the damage caused by a low-velocity impact.

From the theoretical standpoint, all described functionalities are results of coupling of multi-physics fields i.e. interaction between the structural load-carrying performance and other as-needed functionalities (e.g. thermal, electrical, magnetic, chemical, optical, etc.).

2.4 Electromagnetic Effects

Electromagnetic solids encompass a broad class of materials in which the interaction between mechanical and electromagnetic loads has a pronounced effect on the deformed state. In the most general case, the behavior of electromagnetic materials is described by a system of equations of motion and Maxwell's equations. In the case of electrical conductors, these two sets of equations are coupled through the Lorentz force, and in the case of dielectrics (e.g., electrostrictive, magnetostrictive, piezoelectric, and piezomagnetic solids) by means of constitutive relations. Depending on the nature of coupling between electromagnetic and mechanical fields, different approximations to Maxwell's equations are used, which lead to starkly different mathematical formulations, varying from nonlinear systems of parabolic and hyperbolic partial differential equations (PDEs) to linear systems of elliptic PDEs. The scope of early studies [63-69] was mostly limited to isotropic linear elastic conductors, while recently the focus has shifted to the constitutive modeling of electro- and magnetostrictive solids (see, e.g., [70-75]). A special place among electromagnetic solids belongs to piezoelectric materials due to their various applications ranging from hydroacoustics to micro-electro-mechanical actuators and sensors [76-79]. As far as composite materials are concerned, substantial efforts have been devoted in the literature to studies of piezoelectric laminated composites (see, e.g., [80-82] among others) and effective properties of composites with piezoelectric phases [83-85], to name a few.

The main focus of this thesis is on electrically conductive anisotropic composites with a special emphasis on carbon fiber polymer matrix composites. Therefore, the term "electromagnetic effects" is used in this work with respect to the effects of an electromagnetic field on a solid electrical conductor. In electrical conductors, the interaction between mechanical and electromagnetic fields is due to the Lorentz ponderomotive force that is exerted by the electromagnetic field. Mathematically

speaking, the field interactions have to be analyzed by simultaneous solving of Maxwell's equations for the electromagnetic field and the equations of motion of continuous media. Basic milestones of the mechanics of solids with electromagnetic effects were formulated in works [63-69, 86-88]. Due to the complexity of the physical phenomenon as well as insuperable mathematical difficulties associated with simultaneous solving of a generally nonlinear system of equations of motion and Maxwell's equations, there are only a few accomplished solutions even to the problems of three-dimensional linear isotropic elasticity with electromagnetic effects. The situation is better for isotropic plates and shells where a number of solutions for coupled problems exist [69, 89-93]. A significant contribution to the theory of isotropic plates in the presence of an electromagnetic field was made by Ambartsumyan et al. [69], who introduced electromagnetic hypotheses regarding the behavior of the electromagnetic field in plates that complement the classic Kirchhoff hypothesis of nondeformable normals. These hypotheses allowed for reduction of a three-dimensional problem to a two-dimensional one that can be further linearized in certain situations using the small disturbance concept. Such an approach and its modifications were successfully used in the literature [91-96]. The aforementioned electromagnetic hypotheses and the small disturbance concept have been applied in [97-100] to solve magnetoelastic problems for anisotropic and laminated composite plates and shells. In recent work [101, 102] the effects of steady and slowly varying electromagnetic fields on the mechanical response of composite plates were studied. Two-dimensional (2D) approximations to Maxwell's equations and the Lorentz force were obtained by introducing additional hypotheses regarding the behavior of the electromagnetic field components. Within the developed 2D approximation, the problems of static and time-dependent mechanical response of DC and AC electric current-carrying composite plates subjected to mechanical load and immersed in the magnetic field were considered. It has been shown that an electromagnetic field, depending on the direction of its application and intensity, may

significantly enhance or reduce the stress state of the mechanically loaded composite plate. It is important to note that the approach used in [101, 102] differs from that of others [69, 91-99], where the small disturbance concept was utilized and is capable of treating highly dynamic problems. This approach is valid for both linear and geometrically nonlinear plate theory formulations as long as the Kirchhoff hypothesis of nondeformable normals is preserved.

An electromagnetic field in electrical conductors is also manifested by Joule heating. For instance, electrically conductive carbon fiber reinforced polymer matrix composites, which are the focus of this work, are adversely affected by heating. At temperatures above glass transition, a rapid degradation of the polymer matrix occurs, which leads to deterioration in composite strength and elastic moduli. Thus, thermal effects have to be considered in the analysis of the mechanical behavior of the composites subjected to even moderate electromagnetic fields. A problem of DC electric current-induced heating and the associated thermal stresses in the electrified carbon fiber polymer matrix composite plate was considered in [103]. It was shown that application of even moderate DC currents to the composites leads to considerable Joule heating, which, in turn, results in a considerable rise of the thermal stresses. These stresses seem to be avoidable if electromagnetic loads of high intensity but short duration (i.e., pulsed electromagnetic loads) are applied. If such electromagnetic loads are applied concurrently with a dynamic mechanical load of short duration, the resulting mechanical response of composites may be distinctly different (as compared to the case when only mechanical load is applied) due to electro-magneto-mechanical coupling. Owing to the high intensity of the electromagnetic field, the electromagnetic effects may be significant.

The present work aims to study the effects of electromagnetic fields on the dynamic mechanical response of anisotropic composites with a special focus on the carbon fiber reinforced polymer (CFRP) composites. CFRP composites consist of electrically conductive fibers and dielectric polymer matrix, and are electrically

anisotropic and conductive at the macroscale. The influence of an electromagnetic field on the mechanical response of electrically conductive composites is characterized by a complex array of factors among which are coupling of the mechanical and electromagnetic fields and electric current-induced heating. The mechanical behavior of CFRP composites in the presence of an electromagnetic field is a result of complex electro-magneto-thermo-mechanical interactions. The coupling between mechanical and electromagnetic fields is due to the Lorentz ponderomotive force that is exerted by the electromagnetic field [63-70], whereas coupling between electromagnetic and thermal fields is due to electric-current-induced heating [71-74]. Moreover, the electric-current-induced thermal field may lead to thermal deformation in the CFRP composites, which adds an additional layer of complexity to the coupling phenomenon. In general, the effect of an electromagnetic field on the mechanical deformation depends on the strength of the field as well as the electrical properties of the material: the higher the strength of the field and the electrical conductivity, the more distinct a mechanical response is observed as compared to the response when no electromagnetic field is present. This coupling mechanism can potentially lead to the development of structures amenable to active control by the electromagnetic field.

The present research is also directly related to the experimental studies of Telitchev et al. [1, 2] and Sierakowski et al. [3], who investigated the impact response of electrified CFRP composites. They performed a series of low velocity impact tests on electrified unidirectional and cross-ply CFRP composite plates. The tests were carried out under 0A, 25A, and 50A DC electric current applied to the composites plates. The results of measurements showed considerable dependence of the impact-induced damage upon the intensity of the electric field applied to the composite. In particular, when an electric current of 25 A and 50 A was applied to a unidirectional CFRP composite plate, the maximum load sustained by the plate had increased. Moreover, a direct relation was noticed between the field applied to the composite and the propagation of the impact

damage: the stronger was the applied field, the less damage was observed in the experiments. The aforementioned results were valid for the case when an electric current was applied immediately before the impact. Remarkably, it has been determined that a prolonged application of an electric current to the CFRP composites led to significant Joule heating that eliminated the positive effect of the short-term current application. One possible way to mitigate the negative effects of the current-induced heating observed in experiments on electrified composites subjected to a high DC current [103] is to apply electromagnetic loads of high intensity but short duration (i.e., pulsed electromagnetic loads).

CHAPTER 3

FIELD EQUATIONS

3.1 Governing Equations for Anisotropic Solids with

Electromagnetic Effects

Analysis of the electro-magneto-thermo-mechanical interactions in electrically conductive materials requires simultaneous solving of Maxwell's equations for the electromagnetic field, equations of motion, and heat transfer equation. In solids with electromagnetic effects, the interaction between mechanical and electromagnetic fields is due to the Lorentz ponderomotive force that is exerted by the electromagnetic field. Maxwell's equations for an electromagnetic field (see, e.g., [104]) have the form:

$$
\begin{aligned}
&\mathrm{div}\mathbf{D} = \rho_e, \\
&\mathrm{curl}\mathbf{E} = -\frac{\partial \mathbf{B}}{\partial t}, \\
&\mathrm{div}\mathbf{B} = 0, \\
&\mathrm{curl}\mathbf{H} = \mathbf{j} + \frac{\partial \mathbf{D}}{\partial t},
\end{aligned}
\tag{3-1}
$$

and equations of motion of continuous media are

$$
\nabla \cdot \mathbf{T} + \rho\left(\mathbf{F} + \mathbf{F}^L\right) = \rho\frac{\partial^2 \mathbf{u}}{\partial t^2}.
\tag{3-2}
$$

Here $\mathbf{E}$ and $\mathbf{D}$ are the electric field and electric displacement vectors, $\mathbf{B}$ and $\mathbf{H}$ are the magnetic induction and magnetic field vectors, ρ_e is the charge density, $\mathbf{j}$ is the electric current density vector, $\mathbf{T}$ represents the mechanical stress tensor, $\mathbf{F}$ is the body force per unit mass vector, $\mathbf{F}^L$ is the Lorentz ponderomotive force per unit mass vector, $\mathbf{u}$ is the

displacement vector, ρ is the material density of the solid body, t is time, and ∇ is the gradient operator. Moreover, it has been shown in [101, 102] that, in the case of an electrically anisotropic and linear but magnetically isotropic solid body, the constitutive relations for the electromagnetic field in Lagrangian coordinates and in the SI units have the form

$$
\begin{aligned}
\mathbf{D} &= \boldsymbol{\varepsilon}\mathbf{E} + \mu\left(\boldsymbol{\varepsilon} - \varepsilon_0 \cdot \mathbf{1}\right)\left(\frac{\partial \mathbf{u}}{\partial t} \times \mathbf{H}\right), \\
\mathbf{B} &= \mu\mathbf{H} - \mu\frac{\partial \mathbf{u}}{\partial t} \times \left(\left(\boldsymbol{\varepsilon} - \varepsilon_0 \cdot \mathbf{1}\right)\cdot\mathbf{E}\right), \\
\mathbf{j} &= \boldsymbol{\sigma}\left(\mathbf{E} + \frac{\partial \mathbf{u}}{\partial t} \times \mathbf{B}\right) + \rho_e\frac{\partial \mathbf{u}}{\partial t},
\end{aligned}
\tag{3-3}
$$

where $\boldsymbol{\varepsilon}$ and $\boldsymbol{\sigma}$ are the electric permittivity and conductivity tensors,

$$
\boldsymbol{\varepsilon} = \begin{bmatrix} \varepsilon_x & 0 & 0 \\ 0 & \varepsilon_y & 0 \\ 0 & 0 & \varepsilon_z \end{bmatrix},
\tag{3-4}
$$

$$
\boldsymbol{\sigma} = \begin{bmatrix} \sigma_x & 0 & 0 \\ 0 & \sigma_y & 0 \\ 0 & 0 & \sigma_z \end{bmatrix},
\tag{3-5}
$$

where μ is the magnetic permeability (single-value constant and is the same as in vacuum), $\mathbf{1}$ is the unit tensor of the second order.

In the most general case, when a solid body possesses properties of polarization and magnetization (or anisotropy in electric and/or magnetic properties), the expression for the Lorentz force $\mathbf{F}^L$ in any curvilinear inertial coordinate system is given by [105]

$$
\mathbf{F}^L = \rho_e\mathbf{E} + \left(\mathbf{D}_\alpha\nabla\mathbf{E}_\alpha - \mathbf{E}_\alpha\nabla\mathbf{D}_\alpha + \mathbf{B}_\alpha\nabla\mathbf{H}_\alpha - \mathbf{H}_\alpha\nabla\mathbf{B}_\alpha\right) + (\mathbf{J} \times \mathbf{B}),
\tag{3-6}
$$

where $\mathbf{J}$ is the density of the external electric field, ∇ is the gradient operator, and Einstein's summation convention is adopted with respect to the index α. It has been

shown in the literature [102] that in the case of an electrically anisotropic and linear but magnetically isotropic solid body (which is the case for carbon fiber reinforced polymer matrix composites), the Lorentz ponderomotive force (3-6) can be written in the form

$$
\begin{aligned}
\mathbf{F}^L = \rho_e \left(\mathbf{E} + \frac{\partial \mathbf{u}}{\partial t} \times \mathbf{B} \right) + \left(\boldsymbol{\sigma} \left(\mathbf{E} + \frac{\partial \mathbf{u}}{\partial t} \times \mathbf{B} \right) \right) \times \mathbf{B} + \left(\left(\left(\boldsymbol{\varepsilon} - \varepsilon_0 \cdot \mathbf{1} \right) \mathbf{E} \right) \times \mathbf{B} \right)_\alpha \nabla \left(\frac{\partial \mathbf{u}}{\partial t} \right)_\alpha \\
+ (\mathbf{J} \times \mathbf{B}),
\end{aligned}
\tag{3-7}
$$

where $\boldsymbol{\sigma}$ is the electrical conductivity tensor, $\boldsymbol{\varepsilon}$ is the electrical permittivity tensor, ε_0 is the vacuum permittivity, and $\mathbf{1}$ is the unit tensor of second order. The third nonlinear term in equation of Lorentz force is related to anisotropy in electrical properties; i.e. it vanishes when the electric properties of the material are isotropic. The last term in (3-7) is caused by the external electric current that the solid body carries. As it can be seen, in electrically anisotropic solids, the Lorentz force depends not only on the electromagnetic parameters (such as the electric and magnetic fields, the magnitude of the electric current and its orientation with respect to the magnetic field), but also on the rate of deformation of the solid ($\partial \mathbf{u} / \partial t$). Therefore, the system of governing electro-magneto-mechanical equations (3-1)–(3-2) for electrically conducting solids is nonlinear, even in the case of a linear material behavior, and coupled which requires simultaneous solving of the equations. Thus, governing equations (3-1) and (3-2) constitute the general mathematical framework for solving dynamic problems for the solids with electromagnetic effects.

It is worthwhile to comment briefly on the choice of the system of units adopted in the studies of solids with electromagnetic effects. In many studies on electromagnetic field theory and electromagnetic field effects in solids, the Gaussian system of units is used to describe an electromagnetic field, which results in a presence of the speed of light factor $c \; 3 \cdot 10^8 \, \text{m/s}$ in equations (3-1), (3-6) and (3-7). In situations when an analytical solution is of interest, the choice of SI or Gaussian systems is rather a matter of convenience; however, when one is concerned with the development of numerical

schemes, the presence of c can lead to significant computational issues with scalability and convergence of the numerical schemes. Therefore, to avoid potential scalability problems, the SI units are adopted in this study.

It is also worthwhile to emphasize the substantial differences in the mathematical formulations of the governing equations for electrical conductors and, for instance, piezoelectrics. In piezoelectric materials the magnetic effects are generally ignored, and instead of the full system of Maxwell's equations, only equations of electrostatics are considered: $\operatorname{div}\mathbf{D} = 0$, $\mathbf{E} = -\operatorname{grad}\psi$ (i.e. $\operatorname{curl}\mathbf{E} \equiv 0$), where ψ is the electrostatic potential. Furthermore, the electro-mechanical coupling terms appear only in the constitutive relations. This, together with the fact that many piezoelectric materials do not exhibit nonlinearities in the response under typical operating conditions, makes the system of the governing equations describing electromechanical behavior of piezoelectrics linear. Moreover, it allows one to use solution procedures similar to those developed within Lame and Beltrami-Mitchell formulations of the classical elasticity theory, which is not the case even for linear electrical conductors, in which the electro-magneto-mechanical coupling is nonlinear.

The heat transfer equation in the anisotropic elastic media is

$$\nabla \cdot \left(\mathbf{k}\nabla T - T^{ambient}\mathbf{C}\boldsymbol{\alpha}\frac{\partial \mathbf{u}}{\partial t} \right) = -Q + c\rho\frac{\partial T}{\partial t}, \tag{3-8}$$

where T is the temperature, $T^{ambient}$ is the ambient temperature, $\mathbf{k}$ is the thermal conductivity tensor, $\mathbf{C}$ is the elasticity tensor, $\boldsymbol{\alpha}$ is the thermal expansion tensor, c is the specific heat, and Q is the Joule heat rate per unit volume.

The Joule heat rate per unit volume is expressed in terms of the electromagnetic field components as

$$Q = \mathbf{J} \cdot \mathbf{E} \tag{3-9}$$

and it couples the electromagnetic and thermal fields.

In general, the problems of interaction of electromagnetic and mechanical fields in electrically conductive solids can be divided into two major types. The first type is related to the problems for which deformation of the solid does not affect considerably the electromagnetic field. In this type of problem, the electromagnetic field is treated first as if the body were rigid, then the Joule heat density and the Lorentz force are calculated, and finally the corresponding thermoelastic problem with the prescribed distribution of heating sources (Joule heating) and body forces (Lorentz forces) is formulated. This is the so-called one-way coupling. On the other hand, there are problems that require simultaneous solving of Maxwell's equations together with the equations of motion, the so-called mutual coupling problems. The nature of coupling in many cases is determined by the characteristics of the applied electromagnetic and mechanical loads. More detailed discussion on the electro-magneto-thermo-mechanical coupling in electrically conductive composites can be found in [103]. In this thesis, a mechanical response of a carbon fiber reinforced composites subjected to a transverse impact and in-plane pulsed electromagnetic loads will be studied. It will be shown that this problem requires considering only mutual coupling between mechanical and electromagnetic fields, whereas a thermoelastic problem can be omitted due to current-induced heating being localized within a very small region adjacent to the composite-electrode interfaces through which the pulsed electric current is injected.

3.2 Two Dimensional (2D) Approximation for Anisotropic Thin Plates

The inherent complexity of the coupled Maxwell's equations (3-1) and equations of motion (3-2) can be reduced by applying simplifying assumptions. For the case of thin

plates, this can be done by employing the classic Kirchhoff hypothesis of nondeformable normals for the mechanical part and the corresponding electromagnetic hypotheses introduced by Ambartsumyan et al. [69]. This approach was successfully used for the case of isotropic thin plates in several studies [69, 92, 98]. Other researchers such as Librescu et al. [98] and Qin et al. [99] have employed the small disturbance concept to simplify the nonlinear magneto-elastic problems for anisotropic and laminated composite plates. However, in this study, a different approach is used to solve the coupled system of (3-1) and (3-2) for anisotropic solids, which is not limited to the small disturbance problems.

In this section, the 2D approximation of equations of motions together with the 2D approximation of Maxwell's equations is developed to formulate the system of governing equations of thin, electrically conducting anisotropic plates. For this purpose, a transversely isotropic unidirectional composite plate of uniform thickness h is considered in which current-carrying fibers are aligned along the x-axis, the $y-z$ plane is a plane of symmetry, and plane $x-y$ coincides with the middle plane (Fig. 3). The plate can be loaded with transverse mechanical load and immersed in an external magnetic field.

3.2.1 Governing Mechanical Equations

For the mechanical part of the governing equations, the classic Kirchhoff hypothesis of nondeformble normals can be employed which suggests considering the following displacement field for the plate [106]:

$$u_x = u(x, y, t) - z\frac{\partial w(x, y, t)}{\partial x}, \qquad u_y = v(x, y, t) - z\frac{\partial w(x, y, t)}{\partial y}, \qquad u_z = w(x, y, t), \qquad (3\text{-}10)$$

where $u(x,y,t)$, $v(x,y,t)$, $w(x,y,t)$ are the corresponding middle plane displacement components.
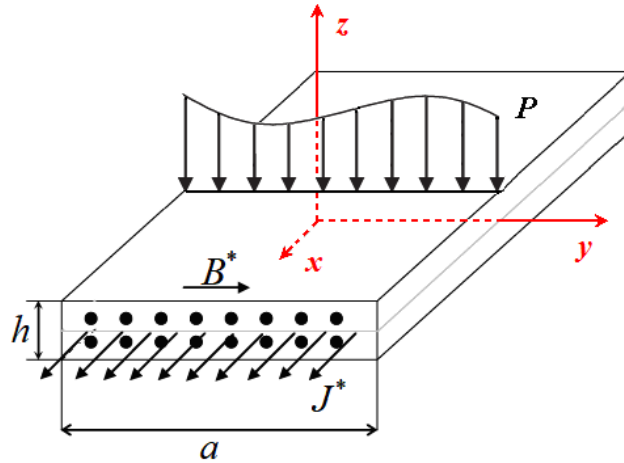
Figure 3. Transversely isotropic plate subjected to mechanical and electromagnetic loads.

Then, the strain-displacement relations can be written as,

$$e_x = \frac{\partial u_x}{\partial x}, \qquad e_y = \frac{\partial u_y}{\partial y}, \qquad e_z = \frac{\partial u_z}{\partial z},$$

$$\gamma_{xy} = \frac{\partial u_x}{\partial y} + \frac{\partial u_y}{\partial x}, \qquad \gamma_{yz} = \frac{\partial u_y}{\partial z} + \frac{\partial u_z}{\partial y}, \qquad \gamma_{xz} = \frac{\partial u_z}{\partial y} + \frac{\partial u_y}{\partial z}, \qquad (3\text{-}11)$$

where γ_{xy}, γ_{yz} and γ_{xz} are engineering shear strains. The generalized Hooke's law for a transversely isotropic plate is in the form:

$$\begin{bmatrix} \tau_{xx} \\ \tau_{yy} \\ \tau_{zz} \\ \tau_{yz} \\ \tau_{xz} \\ \tau_{xy} \end{bmatrix} = \begin{bmatrix} C_{11} & C_{12} & C_{12} & 0 & 0 & 0 \\ C_{12} & C_{22} & C_{23} & 0 & 0 & 0 \\ C_{12} & C_{23} & C_{22} & 0 & 0 & 0 \\ 0 & 0 & 0 & C_{44} & 0 & 0 \\ 0 & 0 & 0 & 0 & C_{55} & 0 \\ 0 & 0 & 0 & 0 & 0 & C_{55} \end{bmatrix} \begin{bmatrix} e_x - \alpha_1 \Delta T \\ e_y - \alpha_2 \Delta T \\ e_z - \alpha_3 \Delta T \\ \gamma_{yz} - \alpha_4 \Delta T \\ \gamma_{xz} - \alpha_5 \Delta T \\ \gamma_{xy} - \alpha_6 \Delta T \end{bmatrix}, \tag{3-12}$$

where α_i are coefficients of thermal expansion, ΔT is the temperature difference, and C_{ij} are the components of the stiffness matrix which are defined in terms of the material properties as follows:

$$C_{11} = \frac{(1 - \nu_{yz}^2)E_1}{1 - \nu}, \qquad C_{12} = \frac{(\nu_{xy} + \nu_{yz}\nu_{xy})E_2}{1 - \nu}, \qquad C_{23} = \frac{(\nu_{yz} + \nu_{yx}\nu_{xy})E_3}{1 - \nu},$$

$$C_{22} = \frac{(1 - \nu_{xy}\nu_{yx})E_1}{1 - \nu}, \qquad C_{44} = G_{yz}, \qquad C_{55} = G_{xy}, \tag{3-13}$$

where

$$\nu = \nu_{yz}^2 + 2\nu_{xy}\nu_{yx}(1 + \nu_{yz}). \tag{3-14}$$

Following the standard procedure of the theory of plates (see, e.g., [107]), the equations of motion (3-2) are integrated with respect to z within the interval $(-h/2, h/2)$ to obtain the equations for stress resultants. To obtain equations for the moment resultants, the first two equations of (3-2) are multiplied by z and integrated with respect to z within the same limits. Finally, this procedure yields five equations of motion for a thin anisotropic plate subjected to mechanical, electromagnetic loads, and associated thermal loads in the absence of body forces:

$$\frac{\partial\left(N_{xx}+N_{xx}^{T}\right)}{\partial x}+\frac{\partial\left(N_{xy}+N_{xy}^{T}\right)}{\partial y}+X_{2}+\rho\int\limits_{-\frac{h}{2}}^{\frac{h}{2}}F_{x}^{L}dz=\rho h\frac{\partial^{2}u}{\partial t^{2}},$$

$$\frac{\partial\left(N_{yy}+N_{yy}^{T}\right)}{\partial y}+\frac{\partial\left(N_{xy}+N_{xy}^{T}\right)}{\partial x}+Y_{2}+\rho\int\limits_{-\frac{h}{2}}^{\frac{h}{2}}F_{y}^{L}dz=\rho h\frac{\partial^{2}v}{\partial t^{2}},$$

$$\frac{\partial\left(N_{xz}+N_{xz}^{T}\right)}{\partial x}+\frac{\partial\left(N_{yz}+N_{yz}^{T}\right)}{\partial y}+Z_{2}+\rho\int\limits_{-\frac{h}{2}}^{\frac{h}{2}}F_{z}^{L}dz=\rho h\frac{\partial^{2}w}{\partial t^{2}}, \qquad (3\text{-}15)$$

$$\frac{\partial\left(M_{xx}+M_{xx}^{T}\right)}{\partial x}+\frac{\partial\left(M_{xy}+M_{xy}^{T}\right)}{\partial y}+hX_{1}+\rho\int\limits_{-\frac{h}{2}}^{\frac{h}{2}}F_{x}^{L}zdz=N_{xz}-\rho\frac{h^{3}}{12}\frac{\partial^{3}w}{\partial t^{2}\partial x},$$

$$\frac{\partial\left(M_{yy}+M_{yy}^{T}\right)}{\partial y}+\frac{\partial\left(M_{xy}+M_{xy}^{T}\right)}{\partial x}+hY_{1}+\rho\int\limits_{-\frac{h}{2}}^{\frac{h}{2}}F_{y}^{L}zdz=N_{yz}-\rho\frac{h^{3}}{12}\frac{\partial^{3}w}{\partial t^{2}\partial y}.$$

Here external body forces are neglected. Equations (3-15) are written with respect to the internal stress (N_{ij}), moment (M_{ij}), thermal stress (N_{ij}^{T}) and moment (M_{ij}^{T}) resultants, and X_{k}, Y_{k}, and Z_{k} stand for

$$X_{1}=\frac{1}{2}\left(\tau_{xz}\bigg|_{z=\frac{h}{2}}+\tau_{xz}\bigg|_{z=-\frac{h}{2}}\right),\quad X_{2}=\tau_{xz}\bigg|_{z=\frac{h}{2}}-\tau_{xz}\bigg|_{z=-\frac{h}{2}},$$

$$Y_{1}=\frac{1}{2}\left(\tau_{yz}\bigg|_{z=\frac{h}{2}}+\tau_{yz}\bigg|_{z=-\frac{h}{2}}\right),\quad Y_{2}=\tau_{yz}\bigg|_{z=\frac{h}{2}}-\tau_{yz}\bigg|_{z=-\frac{h}{2}}, \qquad (3\text{-}16)$$

$$Z_{2}=\tau_{zz}\bigg|_{z=\frac{h}{2}}-\tau_{zz}\bigg|_{z=-\frac{h}{2}}.$$

Referring to Fig. 4, in the case of a transversely isotropic plate with $y-z$ plane of isotropy, the stress and moment resultants are (see, e.g., [106]):

$$N_{xx} = \int\limits_{-\frac{h}{2}}^{\frac{h}{2}} \tau_{xx}dz = hB_{11}\frac{\partial u}{\partial x} + hB_{12}\frac{\partial v}{\partial y} - A_1\int\limits_{-\frac{h}{2}}^{\frac{h}{2}} \tau_{zz}dz,$$

$$N_{yy} = \int\limits_{-\frac{h}{2}}^{\frac{h}{2}} \tau_{yy}dz = hB_{22}\frac{\partial v}{\partial y} + hB_{12}\frac{\partial u}{\partial x} - A_2\int\limits_{-\frac{h}{2}}^{\frac{h}{2}} \tau_{zz}dz,$$

$$N_{xy} = \int\limits_{-\frac{h}{2}}^{\frac{h}{2}} \tau_{xy}dz = hB_{66}\left(\frac{\partial u}{\partial y} + \frac{\partial v}{\partial x}\right), \qquad N_{xz} = \int\limits_{-\frac{h}{2}}^{\frac{h}{2}} \tau_{xz}dz, \qquad N_{yz} = \int\limits_{-\frac{h}{2}}^{\frac{h}{2}} \tau_{yz}dz,$$

$$M_{xx} = \int\limits_{-\frac{h}{2}}^{\frac{h}{2}} \tau_{xx}zdz = -\frac{h^3}{12}B_{11}\frac{\partial^2 w}{\partial x^2} - \frac{h^3}{12}B_{12}\frac{\partial^2 w}{\partial y^2} - A_1\int\limits_{-\frac{h}{2}}^{\frac{h}{2}} \tau_{zz}zdz,$$

$$M_{yy} = \int\limits_{-\frac{h}{2}}^{\frac{h}{2}} \tau_{yy}zdz = -\frac{h^3}{12}B_{22}\frac{\partial^2 w}{\partial y^2} - \frac{h^3}{12}B_{12}\frac{\partial^2 w}{\partial x^2} - A_2\int\limits_{-\frac{h}{2}}^{\frac{h}{2}} \tau_{zz}zdz, \tag{3-17}$$

$$M_{xy} = \int\limits_{-\frac{h}{2}}^{\frac{h}{2}} \tau_{xy}zdz = -\frac{h^3}{6}B_{66}\frac{\partial^2 w}{\partial x\,\partial y},$$

$$N_{xx}^T = \left(B_{11}\alpha_1 + B_{12}\alpha_2\right)\int\limits_{-\frac{h}{2}}^{\frac{h}{2}} \Delta T(x,y,z)dz, \qquad N_{yy}^T = \left(B_{12}\alpha_1 + B_{22}\alpha_2\right)\int\limits_{-\frac{h}{2}}^{\frac{h}{2}} \Delta T(x,y,z)dz,$$

$$N_{xy}^T = B_{66}\alpha_6\int\limits_{-\frac{h}{2}}^{\frac{h}{2}} \Delta T(x,y,z)dz, \qquad N_{xz}^T = B_{66}\alpha_6\int\limits_{-\frac{h}{2}}^{\frac{h}{2}} \Delta T(x,y,z)dz,$$

$$N_{yz}^T = B_{44}\alpha_4\int\limits_{-\frac{h}{2}}^{\frac{h}{2}} \Delta T(x,y,z)dz, \qquad M_{xx}^T = \left(B_{11}\alpha_1 + B_{12}\alpha_2\right)\int\limits_{-\frac{h}{2}}^{\frac{h}{2}} \Delta T(x,y,z)zdz,$$

$$M_{yy}^T = \left(B_{12}\alpha_1 + B_{22}\alpha_2 \right) \int\limits_{-\frac{h}{2}}^{\frac{h}{2}} \Delta T(x,y,z)z\,dz, \qquad M_{xy}^T = B_{66}\alpha_6 \int\limits_{-\frac{h}{2}}^{\frac{h}{2}} \Delta T(x,y,z)z\,dz,$$

$$M_{xz}^T = B_{66}\alpha_6 \int\limits_{-\frac{h}{2}}^{\frac{h}{2}} \Delta T(x,y,z)z\,dz, \qquad M_{yz}^T = B_{44}\alpha_4 \int\limits_{-\frac{h}{2}}^{\frac{h}{2}} \Delta T(x,y,z)z\,dz,$$

where the coefficients B_{11}, B_{12}, B_{22}, B_{44}, B_{66}, A_1 and A_2 are determined using generalized Hooke's law:

$$
\begin{aligned}
& B_{11} = \frac{E_x}{1 - v_{xy}v_{yx}}, \qquad B_{12} = \frac{E_y v_{xy}}{1 - v_{xy}v_{yx}}, \qquad B_{22} = \frac{E_y}{1 - v_{xy}v_{yx}}, \\
& B_{66} = G_{xy}, \qquad B_{44} = B_{22} + B_{23} = G_{yz}, \\
& A_1 = -\frac{v_{xy}\left(1 + v_{yz}\right)}{1 - v_{xy}v_{yx}}, \qquad A_2 = -\frac{v_{yz} + v_{xy}v_{yx}}{1 - v_{xy}v_{yx}}.
\end{aligned}
\tag{3-18}
$$

Here E_x is Young's modulus for the fiber direction, E_y is Young's modulus for the isotropy plane, v_{yz} is Poisson's ratio characterizing the contraction within the plane of isotropy for forces applied within the same plane, v_{xy} is Poisson's ratio characterizing contraction in the plane of isotropy due to forces in the direction perpendicular to it, and v_{yx} is Poisson's ratio characterizing contraction in the direction perpendicular to the plane of isotropy due to forces within the plane of isotropy, G_{xy} is the shear modulus for the direction perpendicular to the plane of isotropy, G_{yz} is the shear modulus in the plane of isotropy ($y - z$).

And the generalized Hooke's law for the transversely isotropic plate can be rewritten in the more convenient form:

$$\tau_{xx} = B_{11}e_x + B_{12}e_y - A_1\tau_{zz} - \left(B_{11}\alpha_1 + B_{12}\alpha_2\right)\Delta T,$$
$$\tau_{yy} = B_{22}e_y + B_{12}e_x - A_2\tau_{zz} - \left(B_{12}\alpha_1 + B_{22}\alpha_2\right)\Delta T,$$
$$\tau_{xy} = B_{66}e_{xy} - A_3\tau_{zz} - B_{66}\alpha_6\Delta T, \tag{3-19}$$
$$\tau_{xz} = B_{66}e_{xz} - B_{66}\alpha_6\Delta T,$$
$$\tau_{yz} = B_{44}e_{yz} - B_{44}\alpha_4\Delta T,$$
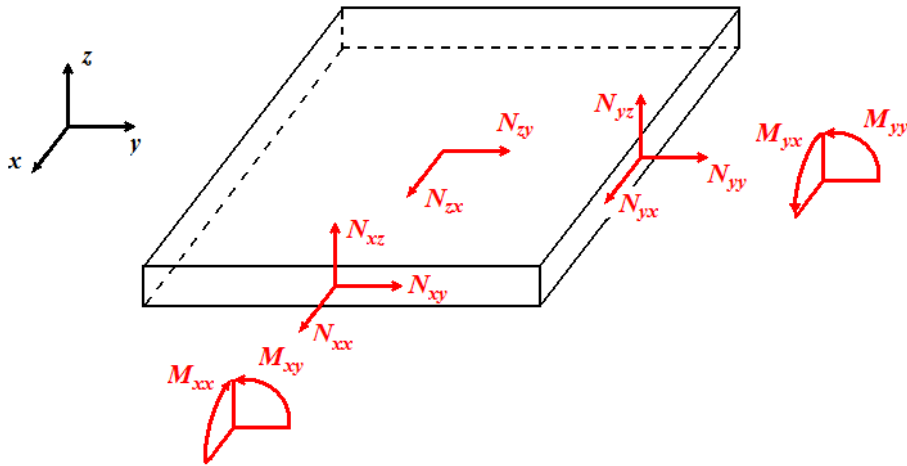
Figure 4. The positive directions of stress and moment resultants defined on the composite plate.

3.2.2 Governing Electromagnetic Equations

In the case of the solids with electromagnetic effects, employing the Kirchhoff hypothesis is not sufficient to reduce the equations of motion to a 2D form without introducing additional hypotheses regarding the behavior of an electromagnetic field in

thin plates and reducing the expression for the Lorentz force to a 2D form. The electromagnetic hypotheses are presented next.

It is assumed that the tangential components of the electric field vector and the normal component of the magnetic field vector do not change across the thickness of the plate:

$$E_x = E_x(x, y, t), \quad E_y = E_y(x, y, t), \quad H_z = H_z(x, y, t).$$

(3-20)

This set of hypotheses was obtained by Ambartsumyan et al. [69] using asymptotic integration of 3D Maxwell's equations. It is important to note that the electromagnetic hypotheses (3-20) are valid only together with the hypothesis of non-deformable normals.

Furthermore, applying the electromagnetic hypotheses (3-20) and taking into account the constitutive relations (3-3), the second and fourth of Maxwell's equations (3-1) can be rewritten in the form

$$-\frac{\partial B_x}{\partial t} = \frac{\partial E_z}{\partial y} - \frac{\partial E_y}{\partial z}, \qquad -\frac{\partial B_y}{\partial t} = \frac{\partial E_x}{\partial z} - \frac{\partial E_z}{\partial x}, \qquad -\frac{\partial B_z}{\partial t} = \frac{\partial E_y}{\partial x} - \frac{\partial E_x}{\partial y},$$

(3-21)

$$\sigma_x E_x = \frac{\partial H_z}{\partial y} - \frac{\partial H_y}{\partial z}, \qquad \sigma_y E_y = \frac{\partial H_x}{\partial z} - \frac{\partial H_z}{\partial x}, \qquad \sigma_z E_z = \frac{\partial H_y}{\partial x} - \frac{\partial H_x}{\partial y}.$$

(3-22)

To obtain (3-21) and (3-22), the term $\partial \mathbf{D} / \partial t$, that is small comparing to the term $\boldsymbol{\sigma}(\mathbf{E} + \partial \mathbf{u} / \partial t \times \mathbf{B})$ (this invokes the so-called quasistatic approximation to Maxwell's equations), and the term $\boldsymbol{\sigma}(\partial \mathbf{u} / \partial t \times \mathbf{B})$, which are small comparing to $\boldsymbol{\sigma}\mathbf{E}$ in the expression for the current density $\mathbf{j}$, are disregarded. After substituting (3-22) in the first two equations (3-21), one can obtain

$$\sigma_y \mu \frac{\partial H_x}{\partial t} = \frac{\partial^2 H_x}{\partial z^2},$$

(3-23)

$$\sigma_x \mu \frac{\partial H_y}{\partial t} = \frac{\partial^2 H_y}{\partial z^2}. \tag{3-24}$$

By introducing operator

$$P^2 = -\sigma_y \mu \frac{\partial}{\partial t}, \tag{3-25}$$

equation (3-23) can be converted into the equation

$$P^2 H_x + \frac{\partial^2 H_x}{\partial z^2} = 0, \tag{3-26}$$

whose general solution is

$$H_x(x, y, z, t) = C(x, y, t)\cos Pz + D(x, y, t)\sin Pz, \tag{3-27}$$

where $C(x, y, t)$ and $D(x, y, t)$ are the integration coefficients that are determined from the boundary values of the magnetic field on the plate external planes $z = \pm h/2$

$$H_i\left(x, y, \pm\frac{h}{2}, t\right) = H_i^{\pm}(x, y, t) \qquad (i = x, y). \tag{3-28}$$

Finally, we have

$$H_x(x, y, z, t) = \cos Pz \sec \frac{Ph}{2} \frac{H_x^+ + H_x^-}{2} + \sin Pz \operatorname{cosec} \frac{Ph}{2} \frac{H_x^+ - H_x^-}{2}, \tag{3-29}$$

and in a similar way,

$$H_y(x, y, z, t) = \cos P_1 z \sec \frac{P_1 h}{2} \frac{H_y^+ + H_y^-}{2} + \sin P_1 z \operatorname{cosec} \frac{P_1 h}{2} \frac{H_y^+ - H_y^-}{2}, \tag{3-30}$$

where the operator P_1 is defined as

$$P_1^2 = \sigma_x \mu \frac{\partial}{\partial t}. \tag{3-31}$$

The linear approximation to (3-29) and (3-30) yields the following linear distribution for tangential (in-plane) components of the magnetic field across the thickness of the plate:

$$H_x\left(x, y, z, t\right) = \frac{1}{2}\left(H_x^+ + H_x^-\right) + \frac{z}{h}\left(H_x^+ - H_x^-\right),$$

$$H_y\left(x, y, z, t\right) = \frac{1}{2}\left(H_y^+ + H_y^-\right) + \frac{z}{h}\left(H_y^+ - H_y^-\right),$$

(3-32)

A more precise second-order approximation is

$$H_x\left(x, y, z, t\right) = \frac{1}{2}\left(1 + \frac{h^2 - 8z^2}{8}P^2 - \frac{h^2 z^2}{16}P^4\right)\left(H_x^+ + H_x^-\right)$$

$$+ \frac{z}{h}\left(1 + \frac{h^2 - 4z^2}{48}P^2 - \frac{h^2 z^2}{144}P^4\right)\left(H_x^+ - H_x^-\right),$$

$$H_y\left(x, y, z, t\right) = \frac{1}{2}\left(1 + \frac{h^2 - 8z^2}{8}P_1^2 - \frac{h^2 z^2}{16}P_1^4\right)\left(H_y^+ + H_y^-\right)$$

$$+ \frac{z}{h}\left(1 + \frac{h^2 - 4z^2}{48}P_1^2 - \frac{h^2 z^2}{144}P_1^2\right)\left(H_y^+ - H_y^-\right).$$

(3-33)

After this, a 2D approximation for the Lorentz force (3-7) is obtained using the Kirchhoff hypothesis of non-deformable normals and the complementing electromagnetic hypotheses (3-20) and (3-32). The explicit expressions for the Lorentz force components for a thin electrically anisotropic (electrical permittivity and conductivity are represented by (3-4) and (3-5)) and magnetically isotropic (magnetic permittivity is the same as in vacuum) plate are:

$$\rho F_x^L = \sigma_y E_y B_z + \sigma_y B_z \left(\frac{1}{2}B_{x1} + \frac{z}{h}B_{x2}\right)\frac{\partial w}{\partial t} - \left(\sigma_y B_z^2 + \sigma_z \left(\frac{1}{2}B_{y1} + \frac{z}{h}B_{y2}\right)^2\right)$$

$$\times \left(\frac{\partial u}{\partial t} - z\frac{\partial^2 w}{\partial x \partial t}\right) + \sigma_z \left(\frac{1}{2}B_{x1} + \frac{z}{h}B_{x2}\right)\left(\frac{1}{2}B_{y1} + \frac{z}{h}B_{y2}\right)\left(\frac{\partial v}{\partial t} - z\frac{\partial^2 w}{\partial y \partial t}\right)$$

(3-34)

$$+\left(\varepsilon_y - \varepsilon_0\right)E_y B_z\left(\frac{\partial^2 u}{\partial x \partial t} - z\frac{\partial^3 w}{\partial x^2 \partial t}\right) - \left(\varepsilon_x - \varepsilon_0\right)E_x B_z\left(\frac{\partial^2 v}{\partial x \partial t} - z\frac{\partial^3 w}{\partial x \partial y \partial t}\right)$$

$$+\left(\varepsilon_x - \varepsilon_0\right)E_x\left(\frac{1}{2}B_{y1} + \frac{z}{h}B_{y2}\right)\frac{\partial^2 w}{\partial x \partial t} - \left(\varepsilon_y - \varepsilon_0\right)E_y\left(\frac{1}{2}B_{x1} + \frac{z}{h}B_{x2}\right)\frac{\partial^2 w}{\partial x \partial t} + J_y^* B_z,$$

$$\rho F_y^L = -\sigma_x E_x B_z + \sigma_z\left(\frac{1}{2}B_{x1} + \frac{z}{h}B_{x2}\right)\left(\frac{1}{2}B_{y1} + \frac{z}{h}B_{y2}\right)\left(\frac{\partial u}{\partial t} - z\frac{\partial^2 w}{\partial x \partial t}\right)$$

$$-\left(\sigma_x B_z^2 + \sigma_z\left(\frac{1}{2}B_{x1} + \frac{z}{h}B_{x2}\right)^2\right)\left(\frac{\partial v}{\partial t} - z\frac{\partial^2 w}{\partial y \partial t}\right) + \sigma_x B_z\left(\frac{1}{2}B_{y1} + \frac{z}{h}B_{y2}\right)\frac{\partial w}{\partial t}$$

$$+\left(\varepsilon_y - \varepsilon_0\right)E_y B_z\left(\frac{\partial^2 u}{\partial y \partial t} - z\frac{\partial^3 w}{\partial x \partial y \partial t}\right) - \left(\varepsilon_x - \varepsilon_0\right)E_x B_z\left(\frac{\partial^2 v}{\partial y \partial t} - z\frac{\partial^3 w}{\partial y^2 \partial t}\right) \quad (3\text{-}35)$$

$$+\left(\varepsilon_x - \varepsilon_0\right)E_x\left(\frac{1}{2}B_{y1} + \frac{z}{h}B_{y2}\right)\frac{\partial^2 w}{\partial y \partial t} - \left(\varepsilon_y - \varepsilon_0\right)E_y\left(\frac{1}{2}B_{x1} + \frac{z}{h}B_{x2}\right)\frac{\partial^2 w}{\partial y \partial t} - J_x^* B_z,$$

$$\rho F_z^L = \sigma_x E_x\left(\frac{1}{2}B_{y1} + \frac{z}{h}B_{y2}\right) - \sigma_y E_y\left(\frac{1}{2}B_{x1} + \frac{z}{h}B_{x2}\right) + \sigma_x B_z\left(\frac{1}{2}B_{y1} + \frac{z}{h}B_{y2}\right)$$

$$\times\left(\frac{\partial v}{\partial t} - z\frac{\partial^2 w}{\partial y \partial t}\right) + \sigma_y B_z\left(\frac{1}{2}B_{x1} + \frac{z}{h}B_{x2}\right)\left(\frac{\partial u}{\partial t} - z\frac{\partial^2 w}{\partial x \partial t}\right) - \left(\sigma_x\left(\frac{1}{2}B_{y1} + \frac{z}{h}B_{y2}\right)^2\right.$$

$$\left. + \sigma_y\left(\frac{1}{2}B_{x1} + \frac{z}{h}B_{x2}\right)^2\right)\frac{\partial w}{\partial t} - \left(\varepsilon_y - \varepsilon_0\right)E_y B_z\frac{\partial^2 w}{\partial x \partial t} + \left(\varepsilon_x - \varepsilon_0\right)E_x B_z\frac{\partial^2 w}{\partial y \partial t} \quad (3\text{-}36)$$

$$+ J_x^*\left(\frac{1}{2}B_{y1} + \frac{z}{h}B_{y2}\right) - J_y^*\left(\frac{1}{2}B_{x1} + \frac{z}{h}B_{x2}\right).$$

After a 2D approximation for the Lorentz force is obtained, reduction of equations of motion (3-15) to the 2D form is straightforward.

A 2D approximation to Maxwell's equations is derived by representing electromagnetic field functions via series expansions with respect to the thickness coordinate and integrating 3D Maxwell's equations across the thickness of the plate:

$$\sigma_x\left(E_x + \frac{\partial v}{\partial t}B_z - \frac{1}{2}\frac{\partial w}{\partial t}\left(B_y^+ + B_y^-\right)\right) = \frac{\partial H_z}{\partial y} - \frac{1}{h}\left(H_y^+ - H_y^-\right),$$

$$\sigma_y\left(E_y - \frac{\partial u}{\partial t}B_z + \frac{1}{2}\frac{\partial w}{\partial t}\left(B_x^+ + B_x^-\right)\right) = -\frac{\partial H_z}{\partial x} + \frac{1}{h}\left(H_x^+ - H_x^-\right),$$

$$-\frac{\partial B_z}{\partial t} = \frac{\partial E_y}{\partial x} - \frac{\partial E_x}{\partial y}.$$

(3-37)

Here $B_x^{\pm}$ and $B_y^{\pm}$ are the boundary values of magnetic induction on the plate external planes $z = \pm h/2$, and σ_x and σ_y are electrical conductivities in the x- and y-directions, which are assumed to be principal material directions. Note that equations (3-37) constitute the so-called quasistatic approximation. From the physical viewpoint, the quasistatic approximation stands for an instantaneous propagation of an electromagnetic field in a medium, where the electric field instantaneously reaches a steady state, while the magnetic field exhibits diffusion into medium. Mathematically, this means omitting the electric displacement current term $\partial \mathbf{D}/\partial t$, which was disregarded as a part of the derivation procedure for (3-32).

The 2D system of equations of motion (3-15) and Maxwell's equations (3-37) is a nonlinear mixed system of parabolic and hyperbolic partial differential equations that governs the mechanical response of thin anisotropic plates with electromagnetic effects. In the next section, the numerical procedure employed to solve the boundary-value problem of the system (3-15) and (3-37) is discussed.

3.2.3 Boundary Conditions

An exact solution of a physical problem must simultaneously satisfy both the governing differential equation and the boundary conditions of the problem. Boundary conditions are divided into three types: Dirichlet, Neumann, and Cauchy boundary

conditions. Regarding the problem discussed in this study which deals with electro-magneto-thermo-mechanical coupling, the mechanical, thermal and electromagnetic boundary conditions need to be separately defined and satisfied by the solution.

As for the mechanical boundary conditions, different kinds of boundary conditions such as a simply-supported, clamped, partially fixed, elastic-supported (with or without restraints), or free edge can be considered for each boundary edge [108]. Thermal boundary conditions may include fixed surface temperature, heat flux (adiabatic or insulated surface), or convection or radiation surface condition [109].

The electromagnetic boundary conditions are defined based on the change in field parameters at the interface separating two different media. From the Maxwell's equations (3-1), it can be concluded that across any boundary of the discontinuity, the normal component of the magnetic induction vector $\mathbf{B}$ and tangential components of the electric field $\mathbf{E}$ are continuous; that is, if the field vectors change across the interface of media 1 and 2,

$$(\mathbf{B}_2 - \mathbf{B}_1) \cdot \mathbf{n} = 0$$

(3-38)

$$\mathbf{n} \times (\mathbf{E}_2 - \mathbf{E}_1) = \mathbf{0}$$

(3-39)

where $\mathbf{n}$ is the unit normal to the interface drawn from medium 1 to medium 2. Furthermore, it can be found that the normal components of the electric displacement $\mathbf{D}$ and the electric current density vector $\mathbf{j}$ together with the tangential components of the magnetic field vector $\mathbf{H}$ are all discontinuous across any boundary of the discontinuity [88].

In the next chapter, the numerical procedure for solving the system of governing equations of the discussed electro-magneto-mechanical boundary-value problem is presented.

CHAPTER 4

NUMERICAL SOLUTION PROCEDURE

In this section the key aspects of the numerical solution procedure for the system of governing equations (3-15) and (3-37) that is later used in this work to study the effects of electromagnetic fields on the dynamic response of composites are described.

Many different numerical methods (e.g. shooting techniques, quasilinearization, and finite element methods) have been proposed in the literature to solve nonlinear boundary value problems (BVP) with initial conditions similar to the one introduced in this study. The solution procedure consists of a sequential application of a finite difference time and spatial (with respect to one coordinate) integration schemes, quasilinearization of the resulting system of the nonlinear ordinary differential equations (ODE), a finite difference spatial integration of the obtained two-point boundary-value problem, and method of lines (MOL) for the two dimensional case. For effectiveness of this scheme it has to be assumed that the presence of an electromagnetic field does not produce strong skin effects [102].

Newmark's finite difference scheme for time integration was employed because of its simplicity and wide application in dynamic problems. A quazilinearization method used in this work guaranteed rapid rate of convergence to the solution of the original nonlinear problem. A superposition method with modified Gram-Schmidt orthonormalization was used to solve the resulting linear two-point boundary-value problems. A modified Gram-Schmidt orthonormalization procedure is adopted due to its numerical stability, relative simplicity, and modest computational requirements. Fourth-order Runge-Kutta finite difference method was used for spatial integration. Besides this method, multistep fourth-order Adams-Bashforth method was also examined and yielded similar results.

4.1 Integration and Quasilinearization

In this study, the Newmark finite difference time integration scheme [110] is used for the derivatives of any function f with respect to time:

$$
\begin{aligned}
\frac{\partial^2 f}{\partial t^2}\bigg|_{t+\Delta t} &= \frac{1}{\beta(\Delta t)^2}\left(f\big|_{t+\Delta t} - f\big|_t\right) - \frac{1}{\beta}\left(\frac{1}{\Delta t}\frac{\partial f}{\partial t}\bigg|_t + \left(\frac{1}{2} - \beta\right)\frac{\partial^2 f}{\partial t^2}\bigg|_t\right), \\
\frac{\partial f}{\partial t}\bigg|_{t+\Delta t} &= \frac{\partial f}{\partial t}\bigg|_t + \Delta t\left((1-\gamma)\frac{\partial^2 f}{\partial t^2}\bigg|_t + \gamma\frac{\partial^2 f}{\partial t^2}\bigg|_{t+\Delta t}\right),
\end{aligned}
\tag{4-1}
$$

where β and γ are the scheme parameters and Δt is the time integration step. It is well known that in the linear problems the Newmark scheme (4-1) is unconditionally stable for $\beta = 0.25$ and $\gamma = 0.5$, whereas in the nonlinear problems the stability of the scheme depends on the size of the time step.

The application of the Newmark scheme is followed by finite difference space integration with respect to one of the spatial coordinates (e.g., the x-coordinate). This step is essentially an application of the method of lines and will be discussed in details in Section 4.4. Employing the finite difference space integration with respect to one of the spatial coordinates (the x-coordinate, for instance) reduces the system of equations (3-15) and (3-37) to the form

$$
\frac{\partial \mathbf{g}}{\partial y} = \mathbf{\Phi}\left(y, t, \mathbf{g}, \frac{\partial \mathbf{g}}{\partial t}, \frac{\partial^2 \mathbf{g}}{\partial t^2}\right),
\tag{4-2}
$$

where the unknown N-dimensional vector $\mathbf{g}(y,t)$ is comprised of the unknown stress and moment resultants and the electric field and magnetic induction components, as well as the middle plane displacements and their first derivatives, and $\mathbf{\Phi}$ is a smooth and continuously differentiable function of $\mathbf{g}$. Equations (4-2) form a system of nonlinear ODEs. Together with boundary conditions at the edges of the plate, it constitutes a nonlinear two-point boundary-value problem. Note that reduction of the second order

system of equations (3-15) and (3-37) to the first order system (4-2) was done by replacing the second derivatives of the unknowns in (3-15) and (3-37) as the first derivatives of new unknown functions, which themselves are the first derivatives of the unknowns of the system of equations (3-15) and (3-37).

To solve this system, a quasilinearization method of Bellman and Kalaba [111] is used. Quasilinearization is applied to system (4-2) and the accompanying boundary conditions at the moment of time $t + \Delta t$. A sequence vector $\left\{ \mathbf{g}^{k+1} \right\}$ is generated by the linear equations

$$\frac{d\mathbf{g}^{k+1}}{dy} = \mathbf{\Phi}\left(\mathbf{g}^{k} \right) + \mathbf{J}\left(\mathbf{g}^{k} \right)\left(\mathbf{g}^{k+1} - \mathbf{g}^{k} \right),$$
(4-3)

and the linearized boundary conditions

$$\mathbf{D_1}\left(\mathbf{g}^{k} \right) \mathbf{g}^{k+1}\left(y_0, t + \Delta t \right) = \mathbf{d_1}\left(\mathbf{g}^{k} \right),$$
$$\mathbf{D_2}\left(\mathbf{g}^{k} \right) \mathbf{g}^{k+1}\left(y_N, t + \Delta t \right) = \mathbf{d_2}\left(\mathbf{g}^{k} \right),$$
(4-4)

with $\mathbf{g}^0$ being an initial guess. Here $\mathbf{g}^{k}$ and $\mathbf{g}^{k+1}$ are the solutions at the k-th and $(k+1)$-th iterations, matrices $\mathbf{D_1}\left(\mathbf{g}^{k} \right)$ and $\mathbf{D}_2\left(\mathbf{g}^{k} \right)$ together with vectors $\mathbf{d_1}\left(\mathbf{g}^{k} \right)$ and $\mathbf{d}_2\left(\mathbf{g}^{k} \right)$ are determined from the given boundary conditions at the edges of the plate (i.e. points y_0 and y_N, correspondingly), and $\mathbf{J}\left(\mathbf{g}^{k} \right)$ is the Jacobian matrix defined as

$$\left\{ \mathbf{J}_{ij}\left(\mathbf{g}^{k} \right) \right\} = \left\{ \frac{\partial \Phi_i}{\partial g_j}\left(g_1^{k}, g_2^{k}, \dots g_N^{k} \right) \right\}.$$
(4-5)

The Jacobian matrix needs to be calculated analytically.

The sequence of solutions $\left\{ \mathbf{g}^{k+1} \right\}$ of the linear system (4-3) ultimately converges to the solution of the nonlinear system (4-2). The iterative process is terminated when the desired accuracy of the solution is achieved

$$\left| \frac{g_i^{k+1} - g_i^k}{g_i^k} \right| \le \delta , \tag{4-6}$$

where δ is the convergence parameter.

At the first time step, the initial approximation to the solution of the nonlinear problem is the solution to the corresponding linear system, and at the following time steps the initial approximation to the solution is the nonlinear solution at the previous time step. This assures a fast convergence to the nonlinear solution at each time step.

It remains to discuss the solution technique for the linear two-point boundary-value problem (4-4) for the system of linear differential equations (4-3). Various methods, such as the finite-difference method, superposition, and shooting techniques [112-116] can be employed for solution of equations (4-3)-(4-4). In this study, the superposition method along with the stable discrete orthonormalization technique [101, 116-119] is used. The solution to the boundary-value problem (4-3)-(4-4) at the $(k+1)$-th iteration is sought in the form of a linear combination of J linearly independent general solutions and one particular solution

$$\mathbf{g}^{k+1}(y, t + \Delta t) = \sum_{j=1}^{J} c_j \mathbf{G}^j (y, t + \Delta t) + \mathbf{G}^{J+1} (y, t + \Delta t) , \tag{4-7}$$

where c_j, $j = 1, 2, 3, ..., J$ are the solution constants; $\mathbf{G}^j$, $j = 1, 2, 3, ..., J$, are solutions of the Cauchy problem for the homogeneous system (4-3) with homogeneous initial condition at the left endpoint of the interval, at which the solution of the problem is sought; and $\mathbf{G}^{J+1}$ is the solution of the Cauchy problem for the inhomogeneous system (4-3) with initial condition at the left endpoint. If there is the same number of boundary conditions on both ends and they are separated, which is the problem considered in the following numerical studies, $N/2$ base solutions $\mathbf{G}^j$ are needed [116] and $J = N/2$. Construction of the solution in form (4-7) via a straightforward integration will not yield satisfactory results since the matrix of the system (4-3) in the problems with mechanical

and electromagnetic effects is usually "ill-conditioned," which leads to the loss of linear independency in the solution vectors $\mathbf{G}^{j}$, $j = 1, 2, 3, ..., J + 1$. The issues related to the loss of linear independence in the stiff boundary-value problems were extensively discussed in the literature (see among others [116-118]). One of the suggested methods to circumvent the loss of linear independence in the solution vectors is to apply an orthonormalization procedure.

<div align="center">4.2 Orthonormalization</div>

Various orthonormalization methods have been introduced over the years (see, e.g., [120-127]). The Gram-Schmidt orthonormalization [115, 121, 124], Householder decomposition [120, 122], and Singular-Value Decomposition (SVD) [122] are arguably the most widely known orthonormalization techniques. The Householder method is an orthogonal triangularization technique, and the Gram-Schmidt method is a process of triangular orthogonalization. The Gram-Schmidt method is considered more suitable for iterative procedures than the Householder method [122]. The SVD method is very powerful, but it requires significant computational efforts. To improve the numerical stability of the classical Gram-Schmidt orthonormalization method, various modified methods were proposed (see, e.g., [121-125]). Such modified Gram-Schmidt methods are less sensitive to rounding errors.

In this study, a modified Gram-Schmidt orthonormalization procedure is adopted due to its numerical stability, relative simplicity, and modest computational requirements. The orthonormalization procedure is applied at all steps, and whenever needed, reorthonormalization is performed to ensure that the solution vectors always constitute an

orthonormal basis system. The K-criterion with $K = \sqrt{2}$ based on the Eucleadian norms of the solution vectors [125] is selected as the reorthonormalization criterion.

Here main steps of the orthonormalization used in this study are presented. First, solution (4-7) at iteration $(k+1)$ is rewritten in the form

$$\mathbf{g}^{k+1}(y, t + \Delta t) = \mathbf{\Omega}\mathbf{c} + \mathbf{G}^{J+1},$$

(4-8)

where matrix $\mathbf{\Omega}$ is the set of base solutions $\mathbf{G}^j$, $j = 1, 2, 3, ..., J$, and $\mathbf{c}$ is the vector of solution constants c_j. While orthonormalization is performed, the matrix of new orthonormal base solutions, $\mathbf{\Omega}_{new}$, is obtained as

$$\mathbf{\Omega}_{new} = \mathbf{\Omega}_{old}\,\mathbf{P},$$

(4-9)

where $\mathbf{P}$ is a nonsingular upper triangular matrix that is found using a procedure described in [118]. A particular solution that is orthogonal to a new set of the orthonormal base solutions is then calculated as

$$\mathbf{G}_{new}^{J+1} = \mathbf{G}_{old}^{J+1} - \mathbf{\Omega}_{new}\mathbf{\eta}_{new},$$

(4-10)

where the elements of the vector $\mathbf{\eta}_{new}$ are the inner products of $\mathbf{G}_{old}^{J+1}$ and the new base solution vectors of $\mathbf{\Omega}_{new}$. There is no need to normalize the new particular solution [116, 118].

Starting from the left end of the plate and performing orthonormalization, the solution of the boundary-value problem (4-3)-(4-4) can be continued to the last integration point on the right side where the boundary conditions (4-4) give the unknown solution constants. If the endpoint is assumed to be $y = y_m$, the solution after orthonormalization (or reorthonormalization) reads as

$$\mathbf{g}_m^{k+1}(y_m, t+\Delta t) = \mathbf{\Omega}_m(y_m)\mathbf{c}_m + \mathbf{G}_m^{J+1}(y_m),$$
$$\mathbf{G}_m^{J+1}(y_m) = \mathbf{G}_{m-1}^{J+1}(y_m) - \mathbf{\Omega}_m(y_m)\mathbf{\eta}_m(y_m). \tag{4-11}$$

Here, the index m is related to the solution at point y_m. The continuity requires the following condition to be satisfied

$$\mathbf{g}_{m-1}^{k+1}(y_m, t+\Delta t) = \mathbf{g}_m^{k+1}(y_m, t+\Delta t). \tag{4-12}$$

Substituting (4-11) into (4-12) and using equation (4-9), we obtain

$$\mathbf{c}_{m-1} = \mathbf{P}_m(\mathbf{c}_m - \mathbf{\eta}_m). \tag{4-13}$$

The recursive relationship (4-13) enables one to find all solution constants over the plate by proceeding backwards from the endpoint. In such a way, the solution for all the integration points can be found without performing a complete reintegration at all points.

4.3 Spatial Integration and Final Solution

For the spatial integration, explicit fourth-order Runge-Kutta's finite difference procedure is applied to the system of ODEs (4-2):

$$\mathbf{g}_{i+1} = \mathbf{g}_i + \sum_{m=1}^{4} b_m \mathbf{f}_m,$$
$$\mathbf{f}_1 = \Delta x \mathbf{\Phi}(y_i, \mathbf{g}_i),$$
$$\mathbf{f}_2 = \Delta x \mathbf{\Phi}(y_i + c_2\Delta y, \mathbf{g}_i + \beta_{21}\mathbf{f}_2),$$
$$\mathbf{f}_3 = \Delta x \mathbf{\Phi}(y_i + c_3\Delta y, \mathbf{g}_i + \beta_{31}\mathbf{f}_1 + \beta_{32}\mathbf{f}_2), \tag{4-14}$$
$$\mathbf{f}_4 = \Delta x \mathbf{\Phi}(y_i + c_4\Delta y, \mathbf{g}_i + \beta_{41}\mathbf{f}_1 + \beta_{42}\mathbf{f}_2 + \beta_{43}\mathbf{f}_3),$$

where

$$c_1 = 0, \quad c_4 = 1, \quad c_2 = u, \quad c_3 = v,$$

$$u = 0.3, \quad v = 0.6,$$

$$b_2 = \frac{2v-1}{12u(v-u)(1-u)}, \quad b_3 = \frac{1-2u}{12v(v-u)(1-v)},$$

$$b_4 = \frac{6uv-4u-4v+3}{12(1-u)(1-v)}, \quad b_1 = 1-b_2-b_3-b_4,$$

$$\beta_{21} = u, \quad \beta_{32} = \frac{1}{24b_3u(1-v)}, \quad \beta_{31} = v - \beta_{32},$$

$$\beta_{43} = \frac{b_3(1-v)}{b_4} = \frac{1-2u}{12b_4v(u-v)}, \quad \beta_{42} = -\frac{v(4v-5)-u+2}{24b_4u(v-u)(1-v)},$$

$$\beta_{41} = 1 - \beta_{42} - \beta_{43}.$$

(4-15)

A combination of the multistep methods of fourth-order Adams-Bashforth and Adams-Moulton was also examined which yielded exactly same results. The fourth-order Adams-Bashforth is defined as [113]:

$$\mathbf{g}_{i+1} = \mathbf{g}_i + \frac{\Delta y}{24}\big[55\mathbf{\Phi}_i - 59\mathbf{\Phi}_{i-1} + 37\mathbf{\Phi}_{i-2} - 9\mathbf{\Phi}_{i-3}\big],$$

(4-16)

and fourth-order Adams-Moulton method reads as [113]:

$$\mathbf{g}_{i+1} = \mathbf{g}_i + \frac{\Delta y}{24}\big[9\mathbf{\Phi}_{i+1} + 19\mathbf{\Phi}_i - 5\mathbf{\Phi}_{i-1} + \mathbf{\Phi}_{i-2}\big].$$

(4-17)

It should be noted that since the Adams-Bashforth and Adams-Moulton methods are not self-starting, the fourth-order Runge-Kutta is used for the first four steps.

The spatial integration along with the orthonormalization of the solution vectors at each nodal point is performed starting from the first node on the left side of the plate ($y = -a/2$) until reaching the final node on the right ($y = +a/2$). At this point, using the boundary conditions at $y = +a/2$, a linear system of equations can be formed to find the unknown solution constants in (4-7). To solve this linear system of equations, say $\mathbf{Ax} = \mathbf{b}$, the Cholesky decomposition method [115] is employed in which the $n \times n$

matrix of coefficients $\mathbf{A}$ is decomposed into a lower triangular matrix $\mathbf{L}$ and an upper triangular matrix $\mathbf{U}$:

$$\mathbf{A} = \mathbf{LU}$$

(4-18)

where

$$U_{ij} = A_{ij} - \sum_{k=1}^{i-1} L_{ik}U_{kj}, \qquad j = i, \cdots, n$$

$$L_{ij} = \frac{1}{U_{jj}}\left(A_{ij} - \sum_{k=1}^{j-1} L_{ik}U_{kj} \right), \qquad j = 1, \cdots, i-1$$

(4-19)

To overcome the rounding errors in computing the vector of unknowns $\mathbf{x}$, the following iterative refinement is used: after solving the system $\mathbf{A}\mathbf{x}^{(i)} = \mathbf{b}$, the residual vector $\mathbf{r}^{(i)} = \mathbf{A}\mathbf{x}^{(i)} - \mathbf{b}$ is computed. This follows by solving the new system $\mathbf{A}\mathbf{dx}^{(i+1)} = \mathbf{r}^{(i)}$ and updating the solution $\mathbf{x}^{(i+1)} = \mathbf{x}^{(i)} + \mathbf{dx}^{(i+1)}$. This procedure is repeated until an accurate enough solution is achieved. Finally, by solving for the solution constants at the final node, the constants at other nodes can easily be found by the recursive formulation (4-13) which leads to the final solution of unknowns all over the plate using the superposition method (4-7). A code in FORTRAN was developed to implement the described numerical procedure for the solution of the boundary-value problem (4-3)-(4-4).

4.4 Method of Lines

The method of lines (MOL) is a well-established numerical (or semi-analytical) technique that has widely been used to solve the governing partial differential equations of physical boundary value problems [128]. The method has been employed directly to

solve a wide variety of hyperbolic, parabolic, or elliptic PDEs [129-134]. Zafarullah [129] analyzed the numerical errors of the application of MOL to a class of linear and nonlinear parabolic BVPs. Jones et al. [130] applied MOL to solve linear and nonlinear elliptic PDEs and performed stability and convergence analyses for the linear case. Schiesser and Griffiths [132] studied and numerically solved many physical systems, covering all the major classes of PDEs, by the application of MOL and found it a very powerful numerical technique. Saucez et al. [134] investigated the difficulties in the numerical solution of strongly hyperbolic PDEs and proposed some guidance in the solution procedure when MOL is employed.

Recent studies have investigated combinations of MOL and other numerical methods for more accurate solutions; for instance, Ramachandran [133] combined MOL concept with the boundary element (BE) method to solve parabolic PDEs. Such hybrid approach may also be used for problems with complex geometries or material features; e.g., Chen et al. [131] developed an efficient FEM-MOL technique to solve 3D electromagnetic cavity problems. They applied MOL to the homogeneous regions while the FEM was employed to model complex geometrical/material features. Therefore, they simultaneously took advantage of the simplicity of MOL and efficiency of FEM for modeling of intricate structures.

The basic idea of the method of lines is to approximate the original PDE by discretizing all but one of the independent variables in order to obtain a set of ordinary differential equations (ODEs). This is done by replacing the derivatives with respect to one independent variable with algebraic approximations such as finite difference, spline, or weighted residual techniques. Therefore, the PDE can be reduced to an initial-value ODE system which can be easily solved by employing a numerical integration algorithm [132]. The popular algebraic approximation used in most MOL solutions is the finite difference (FD) scheme.

The advantages of MOL include numerical stability, fast convergence, computational efficiency, reduced computational time, and ease of implementation [128]. In some cases, MOL may be more efficient than finite element method as the problem can be solved semi-analytically by discretizing the field equations in one or two dimensions and treat the other dimension analytically [131]. On the other hand, one of the drawbacks of MOL is that its application is restricted to simple geometries. Furthermore, for each line of domain partitioning, a set of new unknowns is added to the system.

In this study, the governing partial differential equations of the 2D problem have three independent variables: x, y and t. When the 1D coupling problem, with two independent variables (y and t), is solved by the numerical procedure presented in this chapter so far, method of lines is the best option to be employed to extend the solution to the 2D case. As the geometry of the problem is not complex, the method can easily be added to the present numerical solution procedure. As mentioned earlier, the Newmark's scheme is used for the time integration. The numerical procedure can be followed by the application of the method of lines to eliminate the explicit presence of one spatial independent variable in the governing equations, converting the system of the PDEs into a system of ODEs similar to (4-2). For this purpose, the plate domain is divided using straight lines perpendicular to the x-direction and the central finite difference is employed to approximate the derivatives with respect to x:

$$
\begin{aligned}
\frac{\partial g_j^i}{\partial x} &\approx \frac{g_j^{i+1} - g_j^{i-1}}{2\Delta x}, \\
\frac{\partial^2 g_j^i}{\partial x^2} &\approx \frac{g_j^{i+1} - 2g_j^i + g_j^{i-1}}{\Delta x^2}, \\
\frac{\partial^3 g_j^i}{\partial x^3} &\approx \frac{g_j^{i+2} - 2g_j^{i+1} + 2g_j^{i-1} - g_j^{i-2}}{2\Delta x^3}, \\
\frac{\partial^4 g_j^i}{\partial x^4} &\approx \frac{g_j^{i+2} - 4g_j^{i+1} + 6g_j^i - 4g_j^{i-1} + g_j^{i-2}}{\Delta x^4},
\end{aligned}
\tag{4-20}
$$

where the index j represents a variable in the vector of unknowns $\mathbf{g}$, index i designates a position along the grid in the x-direction and Δx is the spacing in x. Thus, the system of ODEs approximates the solution of the original system of PDEs at the grid points $i = 1, 2, ..., n_x$. The final form of the system is similar to equation (4-2) except for the fact that the vector of unknowns $\mathbf{g}$ is now n_x times larger:

$$\mathbf{g} = [g_1^1, g_2^1, ..., g_N^1, g_1^2, g_2^2, ..., g_N^2, ..., g_1^{n_x}, g_2^{n_x}, ..., g_N^{n_x}]^T, \tag{4-21}$$

where the vector $\mathbf{g}$ is of the size $(N \cdot n_x) \times 1$.

It is worth to mention that in the method of lines, the system of equations are solved for the unknowns on the lines which are located inside the domain, while the known boundary conditions related to the descritized spatial dimension need to be applied manually to the system of equations. The next chapter presents the implementation of the proposed numerical procedure to solve the nonlinear coupling problem.

CHAPTER 5

DYNAMIC RESPONSE OF THIN ANISOTROPIC PLATES SUBJECTED TO TRANSVERSE IMPACT AND IN-PLANE ELECTROMAGNETIC LOADS

In this chapter, the mathematical framework described in Section 3 and the numerical procedure developed in Section 4 are used to study the effects of electromagnetic fields on the dynamic response of a carbon fiber polymer matrix composite plates.

5.1 Motivation

The present study was partly motivated by the experimental studies of Telitchev et al. [1, 2] and Sierakowski et al. [3], who investigated the impact response of electrified carbon fiber polymer matrix composites and showed that impact resistance of composites can be improved by subjecting them to electrical load at the moment of impact. The studies included a series of low velocity impact tests on electrified unidirectional and cross-ply carbon fiber polymer matrix composites. The tests were carried out under DC current up to 50 A (corresponding current density was $65,617 \ A/m^2$) DC electric current applied to the composite plates. The results of measurements showed considerable dependence of the impact-induced damage upon the intensity of the electric field applied to the composite: the stronger was the applied current, the less damage was observed in the experiments. At the same time, it was demonstrated that in contrast to a short-term current application that improved the impact response of the tested composite plates, a prolonged application of an electric current apparently had a detrimental effect

on the composites. This motivated the present work to investigate the influence of the various electromagnetic loads including DC, AC, and pulsed electric currents on the dynamic response of CFRP composites.

5.2 Long Thin Transversely Isotropic Plate

5.2.1 Problem Statement

Consider a thin unidirectional fiber-reinforced electrically conductive composite plate of width a and thickness h subjected to the transverse short duration load p, pulsed electric current of density $\mathbf{J}^*$, and immersed in the magnetic field with the induction $\mathbf{B}^*$. The plate is transversely isotropic, where $y-z$ is the plane of isotropy and $x-y$ coincides with the middle plane of the plate. The plate is assumed to be long in the fiber direction, which is also the direction of the applied current (x-direction), simply supported along the long sides, and arbitrarily supported along the short sides (Fig. 5).

We are interested principally in how an electromagnetic field alters the mechanical response of the plate to the impact load. Thus, the simple plate geometry is chosen deliberately to elucidate the effects of interaction of the mechanical and electromagnetic loads.

The density of the applied electric current is

$$\mathbf{J}^* = \left(J_x^*, 0, 0 \right).$$

(5-1)

Various electric current waveform including DC, AC, and pulsed currents will be analyzed.
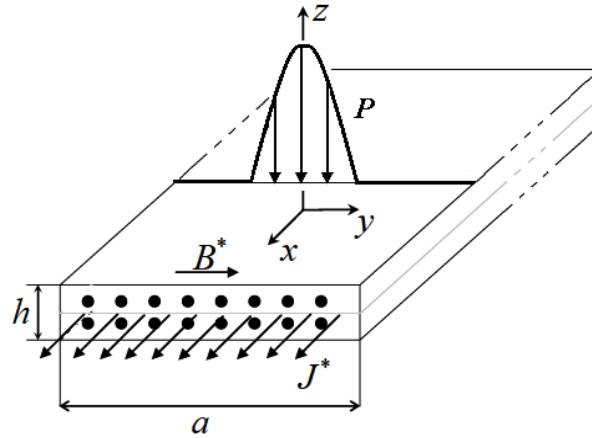
Figure 5. Unidirectional composite plate subjected to the pulsed electric current, transverse impact load, and immersed in the magnetic field.

The plate is also immersed in the constant in-plane magnetic field

$$\mathbf{B}^* = \left(0, B_y^*, 0\right),$$
$$B_y^* = \text{const}. \tag{5-2}$$

In addition, it is assumed that the plate is subjected to a short duration impact load applied transversely to the plate, and this load results in the time-varying compressive pressure distribution, $p(y,t)$, given by:

$$p(y,t) = \begin{cases} p_0 \sqrt{1 - \left(\dfrac{y}{b}\right)^2} \, \sin \dfrac{\pi t}{\tau_p}, & |y| \le b, \ 0 < t \le \tau_p, \\ 0, & b < |y| \le \dfrac{a}{2}, \ t > \tau_p. \end{cases} \tag{5-3}$$

This line pressure mimics the Hertz contact pressure distribution in the quasistatic problem of the elastic impact [135] in the sense that it has a parabolic shape with the maximum located at the center ($y = 0$) and zeros located at the ends of the region to

which it is applied ($y = \pm b$). Here p_0 is the maximum contact pressure, b is the half-size of the contact zone, and τ_p is the characteristic time parameter, which determines the duration of the applied pressure. Note that in the Hertzian model, the size of the contact region increases with an increase in the load, whereas the distribution in (5-3) can be interpreted as a time-varying pressure over the maximum contact area. Moreover, the load is assumed to result only in elastic deformation, and the plate is assumed to be initially at rest.

As for the boundary conditions, the plate is simply supported:

$$
\tau_{zz}\big|_{z=\frac{h}{2}} = -p(y,t),
$$

$$
u_y\big|_{y=\pm\frac{a}{2}} = u_z\big|_{y=\pm\frac{a}{2}} = M_{yy}\big|_{y=\pm\frac{a}{2}} = 0, \tag{5-4}
$$

and the boundary conditions for the electromagnetic field are taken as

$$
\left(E_x - \frac{\partial w}{\partial t} B_y^* + \frac{\partial v}{\partial t} B_z \right)\Bigg|_{y=-\frac{a}{2}} = 0,
$$

$$
E_x\big|_{y=\frac{a}{2}} = 0. \tag{5-5}
$$

The first electromagnetic boundary condition ensures that the electric current does not pass through the boundary $y = -a/2$. The second boundary condition implies that the tangential component of the electric field on the surface of the plate is zero.

It is also assumed that the electric current is applied to the composite plate through the copper bar electrodes attached to the short sides of the plate (Fig. 6), which may result in a non-negligible contact resistance heating with density q_c. The boundary condition at the electric contact is

$$
k_x \frac{\partial T^{(composite)}}{\partial x} - k^{(electrode)} \frac{\partial T^{(electrode)}}{\partial x} = q_c, \tag{5-6}
$$

where k_x and $k^{(electrode)}$ are the thermal conductivities of the composite (in $x-$ direction) and electrode, respectively. The density q_c is determined as

$$q_c = J_x^2 R_c,$$

<div align="right">(5-7)</div>

where R_c is the electric contact resistance. The surfaces of the composite plates and electrodes, other than those that are in the electric contact, are assumed to be exposed to air, and Newton's convection takes place there.
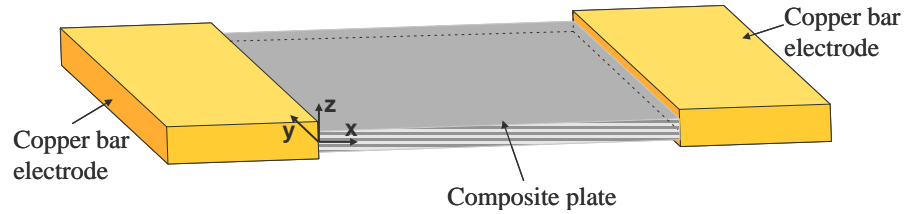
Figure 6. Composite plate and the attached copper bar electrodes.

The following plate parameters are considered in the study. The width of the plate is $a = 0.1524\,\text{m}$ and the thickness is $h = 0.0021\,\text{m}$. The plate is assumed to be made of the AS4/3501-6 unidirectional carbon fiber reinforced polymer matrix composite with 60% fiber volume fraction. The material properties of the composite are as follows: density $\rho = 1594 \text{ kg}/\text{m}^3$, Young's moduli in fiber direction, $E_x = 102.97 \text{ GPa}$ and in transverse direction, $E_y = 7.55 \text{ GPa}$; Poisson's ratios, $v_{yx} = v_{xz} = 0.3$; electric conductivity in fiber direction, $\sigma_x = 39000 \text{ S}/\text{m}$; specific heat $C = 1389.2 \text{ J/kgK}$, thermal conductivity in the fiber direction $k_x = 10.88 \text{ W/mK}$, thermal conductivity in the transverse direction $k_y = k_z = 1.16 \text{ W/mK}$.

The dimensions of the copper electrodes, through which an electric current is injected to the plate, are $0.1524 \times 0.1016 \times 0.009525\,\text{m}$. The electrode material properties are: density $\rho^e = 8700\ \text{kg}/\text{m}^3$, specific heat $C^e = 380\,\text{J/kgK}$, thermal conductivity $k^e = 401\,\text{W/mK}$, and electric conductivity $\sigma^e = 5.81395349 \times 10^7\ \text{S/m}$. The coefficient for the free convection between the composite and air is $23\,\text{W/m}^2\text{K}$, the one between the electrode and air is $12\,\text{W/m}^2\text{K}$, and the ambient temperature is $23\,^\circ\text{C}$. The electric contact resistance is $R_c = 0.0424\,\Omega$. Both the size of the electrodes and the contact resistance are taken from the experimental studies on the electrified CFRP composites [3].

Mechanical loads (5-3) with different characteristic time and maximum contact pressure will be discussed. The half-size of the contact zone is $b = h/100$. The electromagnetic load consisting of the electric current (5-1) and magnetic field (5-2) may vary to investigate its effects on the thermal and mechanical response of the plate. In addition, DC and AC electric currents will be analyzed.

5.2.2 Analysis of the Electromagnetic Field Induced in the Composite Plate by the Applied Electric Current

In this section, the electromagnetic fields that are induced in the electrified composite plate by the electric current of various waveforms applied in the fiber direction are analyzed. The electric currents under consideration are the DC current with density

$$J_x^{DC} = J_0^{DC} = \text{const}\,,\tag{5-8}$$

the AC current with density

$$J_x^{AC} = J_x^{AC}(t) = J_0^{AC} \sin \omega^{AC} t, \ t \geq 0,$$

(5-9)

where J_0^{AC} is the maximum AC current density, and the pulsed current with density

$$J_x^P = J_x^P(t) = J_0^P e^{-t/\tau_c} \sin \frac{\pi t}{\tau_c}, \ t \geq 0,$$

(5-10)

where τ_c is the characteristic time parameter. It is assumed that the maxima of AC and pulsed current are reached at the same moment of time and are equal to the magnitude of the DC current. Figure 7 shows the three different waveforms, DC, AC and pulse (the corresponding characteristics of the pulsed current are $J_0^P = 5 \cdot 10^6 \, \text{A/m}^2$, and $\tau_c = 10 \, \text{ms}$, and $\omega^{AC} = 0.004\pi / \tau_c$).

Computations of the magnetic field induced in the composite plate by the current waveforms (5-8), (5-9), and (5-10) have been performed in COMSOL Multiphysics 3.5a. It was assumed that the plate is long enough in the fiber direction that the variation in the field in that direction can be neglected, making a 2D analysis sufficient. Moreover, the electromagnetic field is calculated in the plate as if it were rigid, and, thus, convective terms are neglected in the constitutive equations (3-3).

Figure 8 shows contour plots of the magnetic induction in the composite plate subjected to the pulsed electric current. The current density is $J_0^P = 5 \cdot 10^6 \, \text{A/m}^2$, which corresponds to the peak of the electric current equal to 1600 A and $\tau_c = 10 \, \text{ms}$. The magnetic induction is plotted at the moment of time $t = 4 \, \text{ms}$ that corresponds to the peak of the electric current, and, thus, to the maximum strength of the electromagnetic field induced by the pulsed current.

The distribution of the magnetic field in the plate subjected to DC and AC currents is similar at $t = 4 \, \text{ms}$, when all three current waveforms have the same magnitude. Figures 9 and 10 shows the magnetic induction along the middle plane, $z = 0$,

and along the $z-$ axis, $y = 0$, respectively, both at $t = 4\,\mathrm{ms}$ for the considered electric pulse.
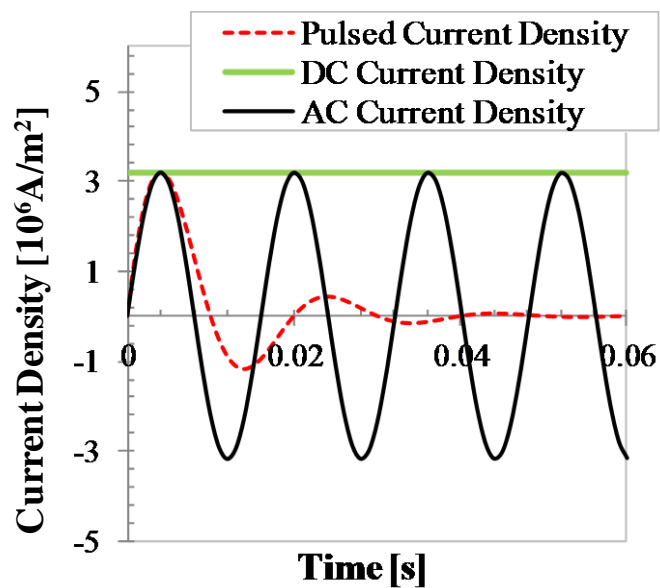
Figure 7. Different waveforms of the applied electric current
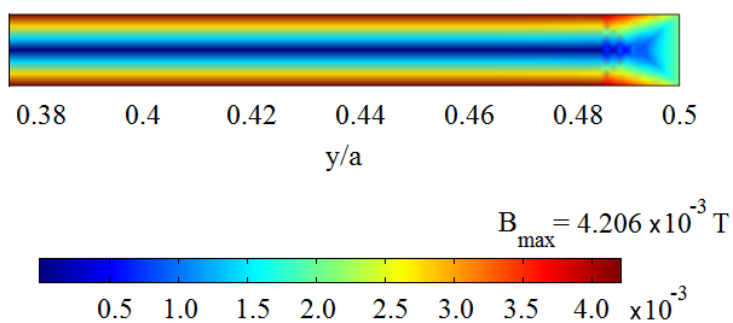
Figure 8. Contour plot of the magnetic induction **B** in the composite plate subjected to the pulsed electric current
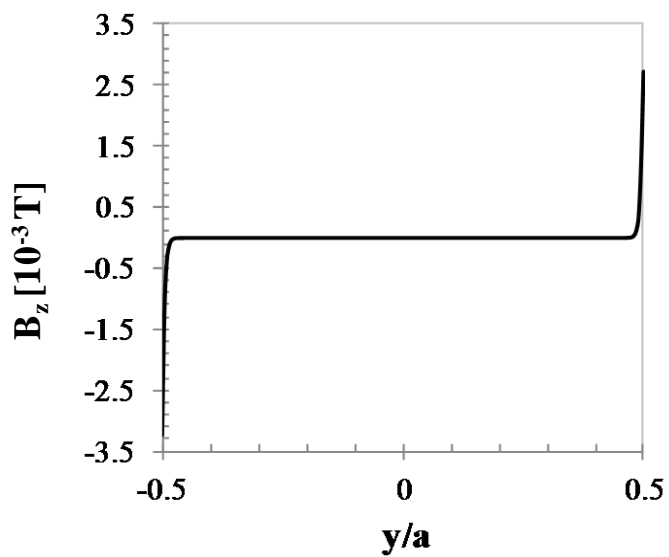
Figure 9. Magnetic induction along the middle plane, $z = 0$
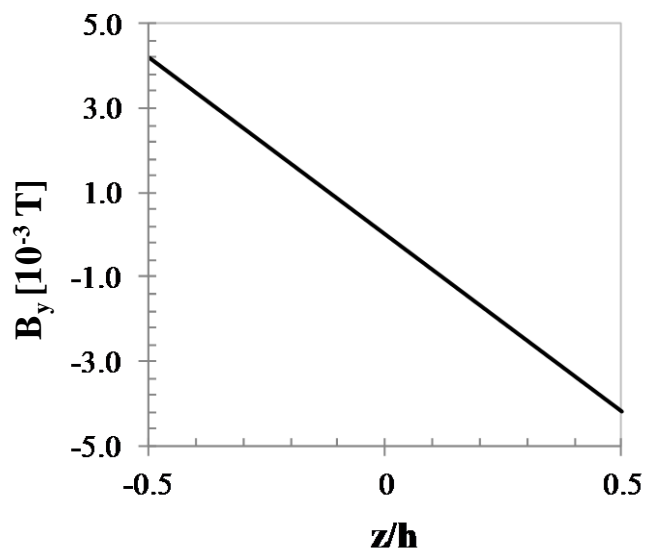
Figure 10. Magnetic induction along the $z -$ axis, $y = 0$

It is worth to mention that there is a direct relationship between the magnitude of the electric current and strength of the induced magnetic field, as follows from Maxwell's equations (3-1). In other words, the results presented in Fig. 8 for the specific current density $J_0^P = 5 \cdot 10^6 \, \text{A}/\text{m}^2$ can be easily scaled if the current density changed.

Overall, the performed computations enable to estimate the magnetic field induced by the electric current, which is important for the evaluation of coupling between electric current, magnetic field, and mechanical field.

The next section is concerned with evaluation of the thermal field induced by the applied electric current.

5.2.3 Heat Transfer in the Electrified Composite Plate

In this section, temperature changes in the composite plate induced by the application of an electric current are analyzed. The 3D heat transfer analysis is performed in COMSOL Multiphysics 3.5a. For the purpose of the heat transfer analysis, it is assumed that the length of the plate is 10 times larger than the width.

First, the heating in the plate produced by the pulsed current (5-10) is compared with that produced by the direct current (DC) of the constant magnitude and alternating current (AC). Figures 11, 12 and 13 show the maximum temperature, $T_{\max}$, developed in the composite plate due to the applied DC (5-8), AC (5-9), and pulsed (5-10) currents at two different values of the electric contact resistance $R_c = 0.0212 \, \Omega$ and $R_c = 0.0424 \, \Omega$. The latter value is taken from the experimental study [3], and the first one, which is twice smaller, is taken for the comparison purposes. It is assumed that the maximums of AC and pulsed currents are reached at the same moment of time and are equal to the magnitude of the DC current as shown in Fig. 7. The corresponding characteristics of the

pulsed current are $J_0^p = 5 \cdot 10^6 \, \text{A}/\text{m}^2$, which corresponds to the peak of the electric current equal to 1600 A, and $\tau_c = 10 \, \text{ms}$.

As it can be seen, application of the AC current reduces composite's heating rate as compared to the DC current application, but does not change the overall trend. At the same time, application of the pulsed current leads to a significant reduction in the maximum temperature attained in the plate and has the highest potential to eliminate the negative thermal effects experimentally observed in composites subjected to DC currents [3, 136, 137] including thermal stresses and polymer matrix degradation.
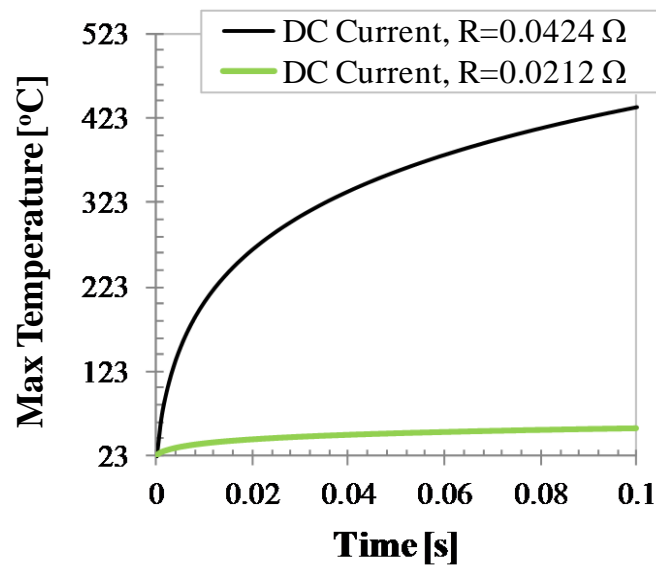
Figure 11. Maximum temperature with respect to time in the plate subjected to the DC current ($J_0^p = 5 \cdot 10^6 \, \text{A}/\text{m}^2$ and $\tau_c = 10 \, \text{ms}$)
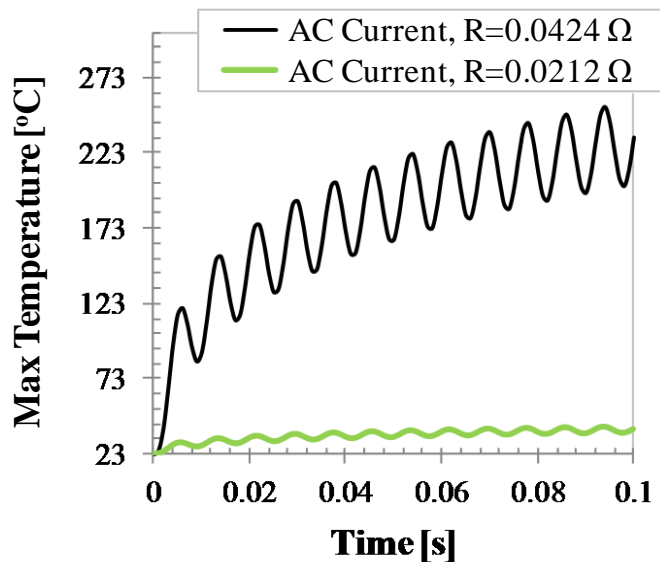
Figure 12. Maximum temperature with respect to time in the plate subjected to the AC current ($J_0^p = 5 \cdot 10^6 \, \text{A}/\text{m}^2$ and $\tau_c = 10 \, \text{ms}$)
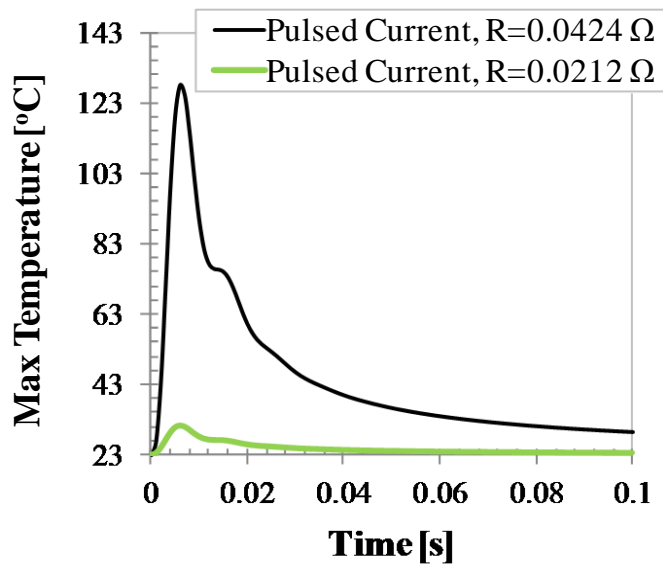
Figure 13. Maximum temperature with respect to time in the plate subjected to the pulsed current ($J_0^p = 5 \cdot 10^6 \, \text{A}/\text{m}^2$ and $\tau_c = 10 \, \text{ms}$)

The temperature in the plate is also strongly affected by the electric contact resistance. It is worth noting that the glass transition temperature for the considered composite material is around $190\,^{\circ}\mathrm{C}$. The performance and material properties of the polymer matrix composites are strongly affected by the temperature. In particular, there is deterioration in the material properties at temperatures above the glass transition temperature. Figure 14 shows the temperature distributions in the plate along the fiber direction at the moment of time $t = 6\,\mathrm{ms}$ (i.e., the moment of time at which the temperature due to the applied pulsed current reaches maximum). The results are presented for DC, AC, and pulsed currents shown in Fig. 7. The corresponding characteristics of the pulsed current are $J_0^p = 5\cdot10^6\,\mathrm{A/m^2}$ and $\tau_c = 10\,\mathrm{ms}$ and the electric contact resistance is $R_c = 0.0212\,\Omega$. The temperatures are plotted against the dimensionless distance x/l from the composite-electrode interface ($l = 10a$, as was stated previously, and $x/l = 1$ corresponds to the composite-electrode interface).

Figure 15 shows the temperature distributions in the plate along the fiber direction at the moment of time $t = 6\,\mathrm{ms}$ (i.e., the moment of time when the temperature reaches maximum) versus the dimensionless distance x/l from the composite-electrode interface ($l = 10a$, as was stated previously, and $x/l = 1$ corresponds to the composite-electrode interface) for various pulsed currents.

As one can see, there is a strong gradient in the temperature field along the plate, but significant temperature growth associated with high electric currents occur only in the regions immediately adjacent to the electric contact (composite-electrode interface). There is practically no change in temperature close to the middle of the plate. These results, together with the temporal temperature variations in the electrified plate, suggest that the temperature changes associated with a pulsed electric current will rather result in the composite material degradation near the electric contact than development of thermal stresses in the plate as opposed to the long-term applications of the DC currents of much lower magnitudes (see, e.g., [103]) that result in the significant thermal stresses

developed across the plate. Thus, thermo-mechanical coupling can be disregarded in the overall evaluation of the mechanical response of the composite plate subjected to the pulsed electric currents. On the other hand, the heat transfer analysis is essential in determination of the range of electric loads, under which no deterioration in the material properties of the composite occurs, since this range depends not only on the characteristics of the applied current, but also on the material properties and electric contact (see, for instance, the work by Sierakowski et al. [3]).

Finally, the influence of the pulsed current characteristic time τ_c on the thermal response of the composite is considered. Figure 16 shows the maximum temperature in the composite plate as a function of time for three different waveforms of the pulsed current with $J_0^p = 5 \cdot 10^6 \, \text{A/m}^2$ and characteristic time parameters $\tau_c = 5 \, \text{ms}$, $\tau_c = 10 \, \text{ms}$, and $\tau_c = 20 \, \text{ms}$.
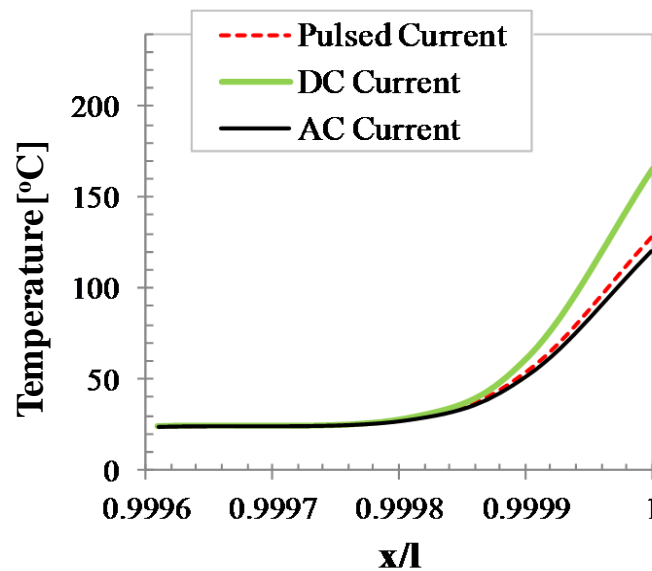
Figure 14. Temperature in the middle plane of the plate along the fiber direction at $t = 6 \, \text{ms}$ for DC, AC, and pulsed currents ($J_0^p = 5 \cdot 10^6 \, \text{A/m}^2$, $\tau_c = 10 \, \text{ms}$, $R_c = 0.0212 \, \Omega$.)
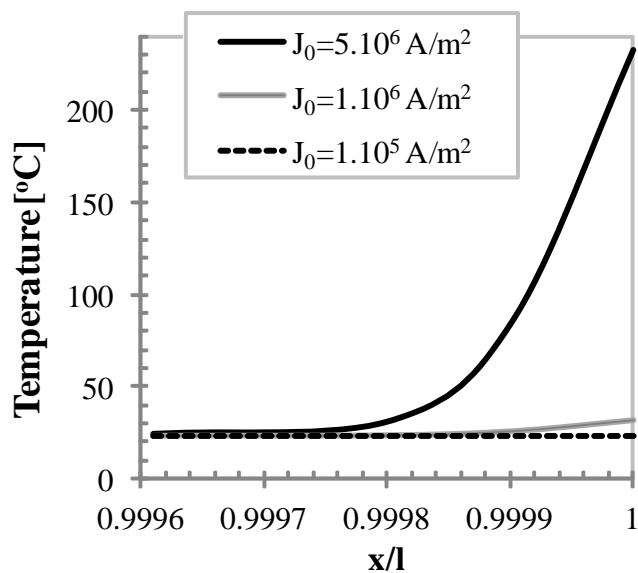
Figure 15. Temperature in the middle plane of the plate along the fiber direction at $t = 6\,\text{ms}$ for various pulsed currents, $\tau_c = 10\,\text{ms}$
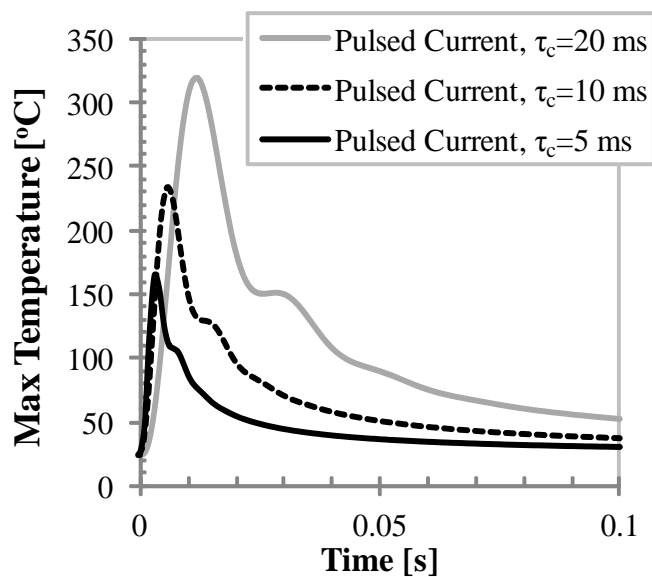
Figure 16. The effect of τ_c on the maximum temperature in the plate, $J_0^p = 5 \cdot 10^6\,\text{A}/\text{m}^2$

As expected, a larger characteristic time leads to a larger temperature rise in the composite plate.

5.2.4 Mechanical Response of the Composite Plate
Subjected to Impact and Electromagnetic Loads

In this section, a mechanical response of the long unidirectional CFRP composite plate described in Section 5.2.1 and subjected to impact and various types of electromagnetic loads, which include DC, AC, and pulsed current as well as a constant in-plane magnetic load, is analyzed. The objective is to elucidate the effects of the various electric current waveforms on the mitigation of stress caused by the impact load. It is assumed that the intensity of the current is such that the associated thermal effects are negligible (as discussed in the previous section) and only electromagnetic effects are taken into account in the evaluation of the mechanical behavior of the plate. The plate is subjected to impact load (5-3), pulsed electric current (5-10), or DC (5-8), or AC (5-9), and magnetic load (5-2) is analyzed. The mechanical and electromagnetic boundary conditions are (5-4) and (5-5), respectively.

To solve this problem, the 2D plate formulation described in Chapter 3 and the numerical solution procedure developed in Chapter 4 are employed. The plate is transversely isotropic ($y - z$ is the plane of isotropy) and long in *x*-direction. Thus, the problem admits the assumption of independence of the components of mechanical and electromagnetic fields of the coordinate x, which reduces the equations of motion (3-15) to the form:

$$\frac{\partial N_{yy}}{\partial y} = \rho h \frac{\partial^2 v}{\partial t^2} + \sigma_x h E_x B_z + \sigma_x h B_z^2 \frac{\partial v}{\partial t} - \frac{1}{2}\sigma_x h B_{y1} B_z \frac{\partial w}{\partial t} + \frac{\varepsilon_x - \varepsilon_0}{B_{22}} h E_x B_z \frac{\partial N_{yy}}{\partial t}$$

$$- \frac{1}{2}(\varepsilon_x - \varepsilon_0) h E_x B_{y1} \frac{\partial W}{\partial t} + h B_z J_x^*(t),$$

$$\frac{\partial N_{yz}}{\partial y} = \rho h \frac{\partial^2 w}{\partial t^2} + p(y,t) - \frac{1}{2}\sigma_x h E_x B_{y1} - \frac{1}{2}\sigma_x h B_{y1} B_z \frac{\partial v}{\partial t} + \frac{1}{4}\sigma_x h \left(B_{y1}^2 + \frac{1}{3} B_{y2}^2 \right)\frac{\partial w}{\partial t}$$

$$+ \frac{1}{12}\sigma_x h^2 B_z B_{y2} \frac{\partial W}{\partial t} - (\varepsilon_x - \varepsilon_0) h E_x B_z \frac{\partial W}{\partial t} - \frac{1}{2} h B_{y1} J_x^*(t),$$

$$\frac{\partial M_{yy}}{\partial y} = -\frac{\rho h^3}{12}\frac{\partial^2 W}{\partial t^2} + N_{yz} - \frac{1}{12}\sigma_x h^2 B_z B_{y2} \frac{\partial w}{\partial t} - \frac{1}{12}\sigma_x h^3 B_z^2 \frac{\partial W}{\partial t}$$

$$- \frac{1}{12}(\varepsilon_x - \varepsilon_0) h^2 E_x B_{y2} \frac{\partial W}{\partial t} + \frac{(\varepsilon_x - \varepsilon_0)}{B_{22}} E_x B_z \frac{\partial M_{yy}}{\partial t},$$

(5-11)

$$\frac{\partial v}{\partial y} = \frac{1}{h B_{22}} N_{yy},$$

$$\frac{\partial^2 w}{\partial y^2} = -\frac{12}{h^3 B_{22}} M_{yy},$$

$$\frac{\partial w}{\partial y} = W,$$

and Maxwell's equations (3-1) to the form:

$$\sigma_x \mu \left(E_x + \frac{\partial v}{\partial t} B_z - \frac{1}{2}\frac{\partial w}{\partial t} B_{y1} \right) = \frac{\partial B_z}{\partial y} - \frac{B_{y2}}{h},$$

$$\frac{\partial B_z}{\partial t} = \frac{\partial E_x}{\partial y}.$$

(5-12)

Here the following notations are introduced:

$$B_{x1} = B_x^+ + B_x^-, \qquad B_{x2} = B_x^+ - B_x^-,$$

$$B_{y1} = B_y^+ + B_y^-, \qquad B_{y2} = B_y^+ - B_y^-.$$

(5-13)

The stress and moment resultants in the considered transversely isotropic plate
with $y - z$ plane of isotropy are given by (see, e.g., [106]):

$$N_{xx} = \int\limits_{-\frac{h}{2}}^{\frac{h}{2}} \tau_{xx}dz = hB_{12}\frac{\partial v}{\partial y} - A_1\int\limits_{-\frac{h}{2}}^{\frac{h}{2}} \tau_{zz}dz, \qquad N_{yy} = \int\limits_{-\frac{h}{2}}^{\frac{h}{2}} \tau_{yy}dz = hB_{22}\frac{\partial v}{\partial y} - A_2\int\limits_{-\frac{h}{2}}^{\frac{h}{2}} \tau_{zz}dz,$$

$$N_{xy} = \int\limits_{-\frac{h}{2}}^{\frac{h}{2}} \tau_{xy}dz = 0, \qquad N_{xz} = \int\limits_{-\frac{h}{2}}^{\frac{h}{2}} \tau_{xz}dz, \qquad N_{yz} = \int\limits_{-\frac{h}{2}}^{\frac{h}{2}} \tau_{yz}dz,$$

$$M_{xx} = \int\limits_{-\frac{h}{2}}^{\frac{h}{2}} \tau_{xx}zdz = -\frac{h^3}{12}B_{12}\frac{\partial^2 w}{\partial y^2} - A_1\int\limits_{-\frac{h}{2}}^{\frac{h}{2}} \tau_{zz}zdz, \qquad M_{xy} = \int\limits_{-\frac{h}{2}}^{\frac{h}{2}} \tau_{xy}zdz = 0,$$

$$M_{yy} = \int\limits_{-\frac{h}{2}}^{\frac{h}{2}} \tau_{yy}zdz = -\frac{h^3}{12}B_{22}\frac{\partial^2 w}{\partial y^2} - A_2\int\limits_{-\frac{h}{2}}^{\frac{h}{2}} \tau_{zz}zdz,$$

$$(5\text{-}14)$$

where the coefficients B_{11}, B_{12}, B_{22} and A_1, A_2 are determined using generalized Hooke's law:

$$B_{11} = \frac{E_x}{1 - \nu_{xy}\nu_{yx}}, \qquad B_{12} = \frac{E_y\nu_{xy}}{1 - \nu_{xy}\nu_{yx}}, \qquad B_{22} = \frac{E_y}{1 - \nu_{xy}\nu_{yx}},$$

$$A_1 = -\frac{\nu_{xy}\left(1 + \nu_{yz}\right)}{1 - \nu_{xy}\nu_{yx}}, \qquad A_2 = -\frac{\nu_{yz} + \nu_{xy}\nu_{yx}}{1 - \nu_{xy}\nu_{yx}}.$$

$$(5\text{-}15)$$

Here E_x is Young's modulus for the fiber direction, E_y is Young's modulus for the isotropy plane, ν_{yz} is Poisson's ratio characterizing the contraction within the plane of isotropy for forces applied within the same plane, ν_{xy} is Poisson's ratio characterizing contraction in the plane of isotropy due to forces in the direction perpendicular to it, and ν_{yx} is Poisson's ratio characterizing contraction in the direction perpendicular to the plane of isotropy due to forces within the plane of isotropy.

The system of equations (5-11) and (5-12) is a mixed system of nonlinear hyperbolic and parabolic PDEs for the thin transversely isotropic plate subjected to the

defined electromagnetic loads and time-varying compressive pressure. This system can be rewritten in the vector form (4-2), where the unknown vector $\mathbf{g}$ stands for

$$\mathbf{g} = \left[v, w, W, N_{yy}, N_{yz}, M_y, E_x, B_z \right]^T . \tag{5-16}$$

The boundary-value problem (5-4)-(5-5) for the system (5-11) and (5-12) has been solved using the numerical procedure described in Section 4. The procedure consists of sequential application of Newmark's finite difference time integration to the non-linear system of PDEs (5-11) and (5-12), reduction of the resulting non-linear system of ODEs to the sequence of the linear two-point boundary-value problems via quasilinearization, and finally applying fourth-order Runge-Kutta's finite difference spatial integration and performing modified Gram-Schmidt orthonormalization at every integration step. The final form of the system of governing equations is presented in Appendix.

The four homogeneous and one non-homogenous initial vectors for the 1D problem are:

$$\begin{aligned}
\mathbf{N}_1^{\text{hom}} &= \left[0,\, 0,\, 1,\, 0,\, 0,\, 0,\, 0,\, 0 \right]^T , \\
\mathbf{N}_2^{\text{hom}} &= \left[0,\, 0,\, 0,\, 1,\, 0,\, 0,\, 0,\, 0 \right]^T , \\
\mathbf{N}_3^{\text{hom}} &= \left[0,\, 0,\, 0,\, 0,\, 1,\, 0,\, 0,\, 0 \right]^T , \\
\mathbf{N}_4^{\text{hom}} &= \left[0,\, 0,\, 0,\, 0,\, 0,\, 0,\, \frac{g_1^k}{2\beta\Delta t} + \zeta_1,\, -1 \right]^T , \\
\mathbf{N}^{non\,\text{hom}} &= \left[0,\, 0,\, 0,\, 0,\, 0,\, 0,\, \zeta_1 g_8^k - \zeta_2 B_y^*,\, -g_8^k \right]^T .
\end{aligned} \tag{5-17}$$

The matrices $\mathbf{D}_1$ and $\mathbf{D}_2$, and vectors $\mathbf{d}_1$ and $\mathbf{d}_2$ in (4-4) for the 1D problem are:

$$\mathbf{D}_1 = \begin{bmatrix}
1, & 0, & 0, & 0, & 0, & 0, & 0, & 0 \\
0, & 1, & 0, & 0, & 0, & 0, & 0, & 0 \\
0, & 0, & 0, & 0, & 0, & 1, & 0, & 0 \\
\dfrac{g_8^k}{2\beta\Delta t}, & \dfrac{-B_y^*}{2\beta\Delta t}, & 0, & 0, & 0, & 0, & 1, & \dfrac{g_1^k}{2\beta\Delta t} + \zeta_1
\end{bmatrix}, \tag{5-18}$$

$$\mathbf{D}_2 = \begin{bmatrix} 1, & 0, & 0, & 0, & 0, & 0, & 0, & 0 \\ 0, & 1, & 0, & 0, & 0, & 0, & 0, & 0 \\ 0, & 0, & 0, & 0, & 0, & 1, & 0, & 0 \\ 0, & 0, & 0, & 0, & 0, & 0, & 1, & 0 \end{bmatrix},$$

$$\mathbf{d}_1 = \left[0,\, 0,\, 0,\, -B_y^* \zeta_2 - \frac{g_1^k g_8^k}{2\beta\Delta t} \right]^T, \qquad \mathbf{d}_2 = \begin{bmatrix} 0,\, 0,\, 0,\, 0 \end{bmatrix}^T,$$

Next section presents the study on the validity of the proposed numerical method followed by the numerical results and discussion.

5.2.4.1 Validation

The first step in the development of the numerical solution is to validate the numerical procedure developed in Section 4. Here, this validation is done by comparing the numerical results of the FORTRAN code developed in this thesis with the corresponding analytical solution of the mechanical response of a long thin transversely isotropic plate (Fig. 5) subjected to a transverse mechanical load. The analytical solution of such a problem with a constant pressure p_0 all over the plate is proposed by Timoshenko in series form as [138]:

$$w\big|_{y=0} = -\frac{p_0 a^4}{h^3 B_{22}} \left[\frac{5}{32} - \frac{48}{\pi^5} \sum_{n=1}^{\infty} \frac{\sin(n\pi/2)}{n^5} \cos(\omega t) \right],$$

$$M_y\big|_{y=0} = -\frac{p_0 a^2}{4} \left[\frac{1}{2} - \frac{16}{\pi^3} \sum_{n=1}^{\infty} \frac{\sin(n\pi/2)}{n^3} \cos(\omega t) \right],$$

(5-19)

where n is an odd number and

$$\omega = \frac{\pi^2 n^2 h}{2 a^4} \sqrt{\frac{B_{22}}{3\rho}}.$$

(5-20)

is the modal frequency of the vibrations of the plate.

The comparison between the numerical and analytical solutions is shown in Figs. 17 and 18. For both cases, $p_0 = 10\,\text{kPa}$ and the time step is $0.0001\,\text{s}$. Moreover, in the numerical simulation, the number of divisions in the y-direction (n_y) is 50000. As it can be seen in the figures, the results for the numerical solution for both the transverse deflection and moment resultant of the middle of the plate match the results of the analytical solution.

Figure 19 shows the mesh convergence of the numerical results while the time step is $0.0001\,\text{s}$. From this figure, the error analysis between the numerical and analytical solutions for the transverse middle plane deflection reveals that the minimum divisions of the plate corresponding to this time step should be 10000 to have less than 1 percent error.
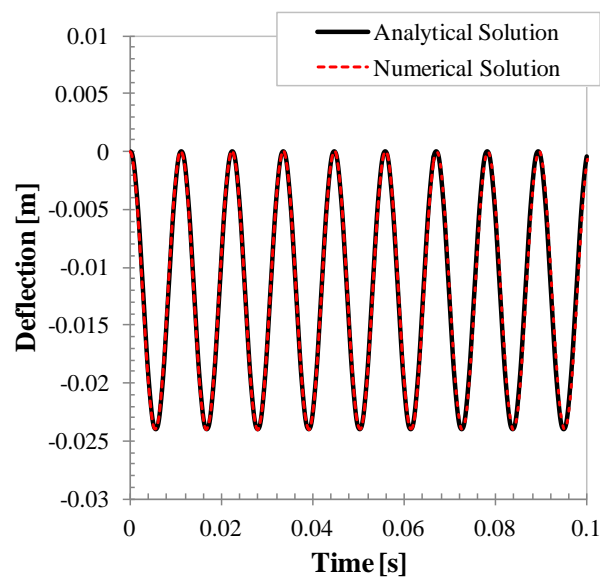
Figure 17. Comparison of the middle plate deflection between analytical and numerical solutions for $p_0 = 10\,\text{kPa}$, $n_y = 50000$ and time step of $0.0001\,\text{s}$.
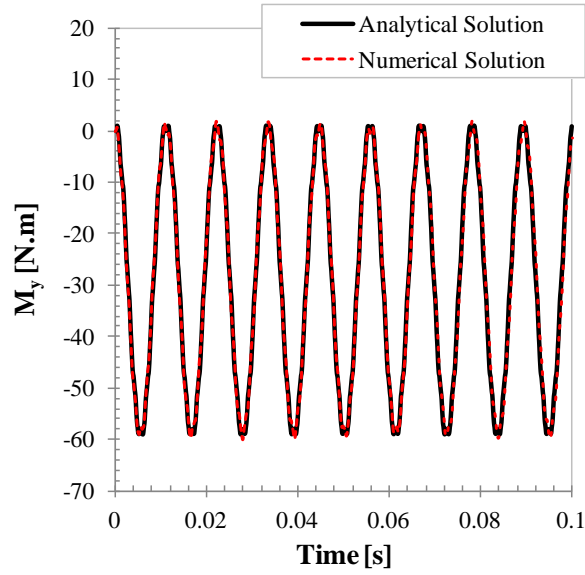
Figure 18. Comparison of the moment resultant between analytical and numerical solutions for $p_0 = 10\,\text{kPa}$, $n_y = 50000$ and time step of 0.0001s.
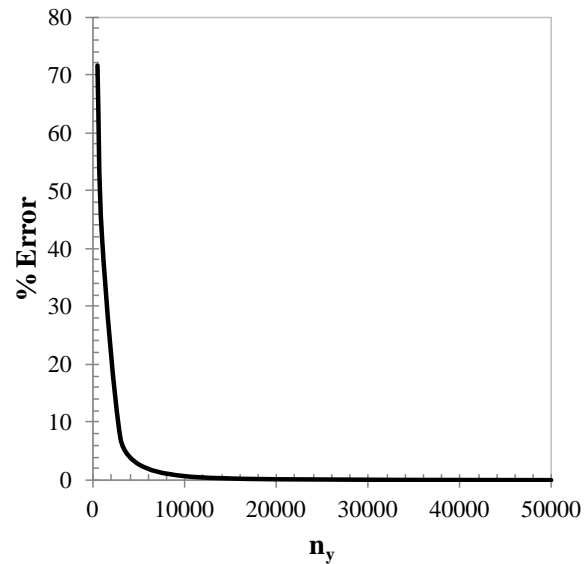
Figure 19. Error percentage versus number of divisions in the y - direction for $p_0 = 10\,\text{kPa}$ and time step of 0.0001s.

The appropriate size steps found from the validation procedure in order to obtain accurate numerical results used in the next section to study the mechanical response of the composite plate subjected to an impact load and various electromagnetic loading profiles.

5.2.4.2 Numerical Results

The computational study has been performed for various electromagnetic loads in order to elucidate the effects of the intensity, direction, and duration of the electromagnetic field on the impact response of the plate. The intensity of the electromagnetic load was restricted by thermal effects considerations discussed in Section 5.2.3. At the same time, the induced magnetic field due to this current, which was discussed in Section 5.2.2, is much smaller than the applied magnetic field (5-2).

For all numerical results in this study, the desired convergence and stability were obtained for the time step of 0.0001 s and the spatial step of $a \times 10^{-5}$ m, where a is the width of the plate and 10^5 is the number of discretization points along the y-direction. The step-size of the Runge-Kutta method was the same as the spatial step. Moreover, the number of steps required to achieve convergence in (4-6) was less than three in all numerical examples.

First, the influence of the electric current waveform on the deflection of the plate is discussed. Figures 20 and 21 show the transverse middle plane deflection, w, at the center of the plate $(y = 0)$ as a function of time for the plate subjected to the prescribed impact load (5-3), magnetic load (5-2) with a relatively low induction $B_y^* = 0.1$ T, and DC (5-8), AC (5-9), and pulsed (5-10) electric currents. It is assumed that the maximums of AC and pulsed current are reached at the same moment of time and are equal to the

magnitude of the DC current. The corresponding characteristics of the pulsed current are $J_0^p = 10^6 \, \text{A}/\text{m}^2$ (in Fig. 20) and $J_0^p = 5 \cdot 10^6 \, \text{A}/\text{m}^2$ (in Fig. 21) and $\tau_c = 10 \, \text{ms}$ in both figures.

As it was expected, the contribution of the electromagnetic load into the deflection response becomes more noticeable with an increase in the magnitude of the electric current density for all three waveforms. There was practically no difference due to an electromagnetic load observed at the lower current densities. At the same time, only a pulsed electric current leads to a marked decrease in the amplitude of the plate's vibrations over the extended period of time, while both DC and AC currents do not produce such a sustainable effect. An increase in the strength of the external magnetic field also has a distinct effect on the deflection response of the plate.
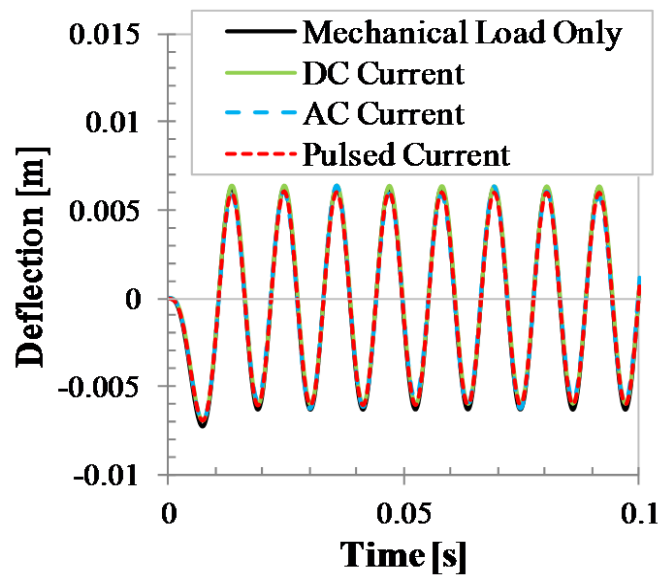
Figure 20. Plate's deflection as a function of time: effect of the electric current waveforms at the low current density ($J_0^p = 10^6 \, \text{A}/\text{m}^2$) and low magnetic induction ($B_y^* = 0.1 \, \text{T}$)
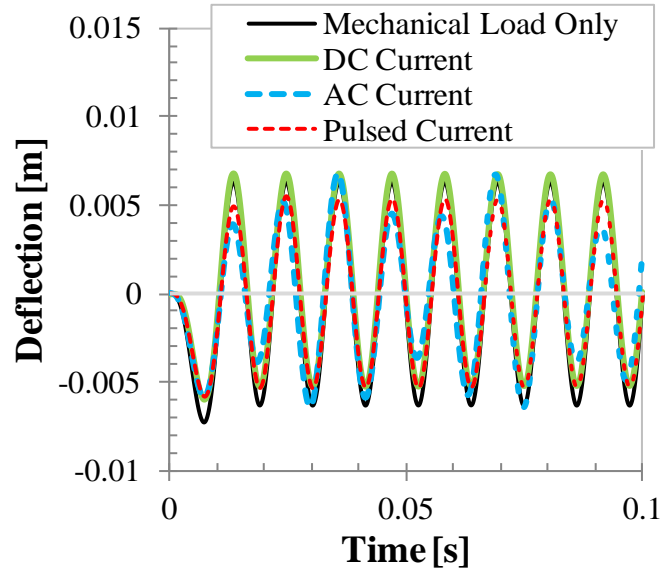
Figure 21. Plate's deflection as a function of time: effect of the electric current waveforms at the high current density ($J_0^p = 5 \cdot 10^6 \, \text{A}/\text{m}^2$) and low magnetic induction ($B_y^* = 0.1 \, \text{T}$)

Figure 22 shows the transverse middle plane deflection, w, at a higher magnetic induction $B_y^* = 1.0 \, \text{T}$ at DC (5-8), AC (5-9), and pulsed (5-10) electric currents. As before, it is assumed that the maximums of AC and pulsed current are reached at the same moment of time and are equal to the magnitude of the DC current. The corresponding characteristics of the pulsed current are $J_0^p = 10^6 \, \text{A}/\text{m}^2 \quad \tau_c = 10 \, \text{ms}$.

As one can see, there is a significant reduction in the amplitude of the vibrations over time for large values of the magnetic induction. This is related to the two-way electro-magneto-mechanical coupling terms in the Lorentz force (3-7) that include velocity and external magnetic induction terms.
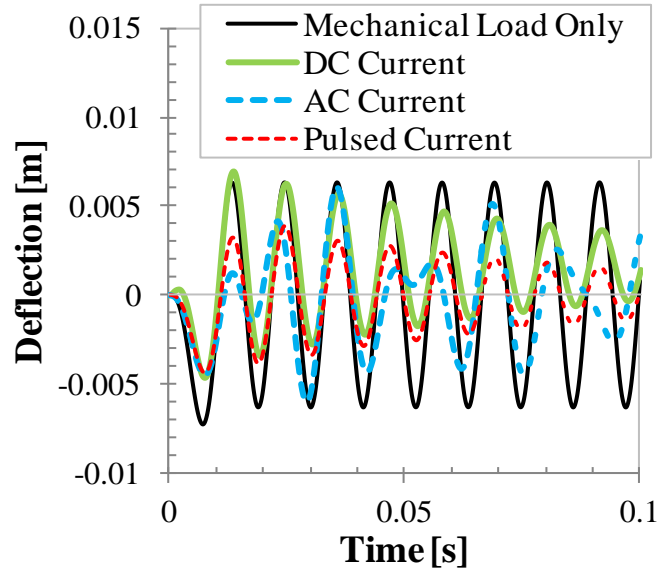
Figure 22. Plate's deflection as a function of time: effect of the electric current waveforms at the low current density ($J_0^p = 10^6 \text{ A/m}^2$) and high magnetic induction ($B_y^* = 1.0 \text{ T}$)

Next, we look specifically at the pulsed electric current and the effect of the pulse duration. Figure 23 shows the mechanical load at the center of the plate ($y = 0$) as well as three different electric pulses applied to the plate over time. Note that the maximum electric current density is the same for all three pulses, where $J_0 = 10^7 \text{ A/m}^2$, but the rise and fall times, which are determined by τ_c , are different, ranging from $\tau_c = \tau_p/2$ to $\tau_c = 2\tau_p$.

Figure 24 shows the transverse middle plane deflection, w , at the center of the plate ($y = 0$) as a function of time for four different loadings consisting of the mechanical load only and combined mechanical and electromagnetic loads. Electromagnetic loads consist of the various pulsed currents (5-10), which are shown in Fig. 23, and constant magnetic field $B_y^* = 0.1 \text{ T}$.
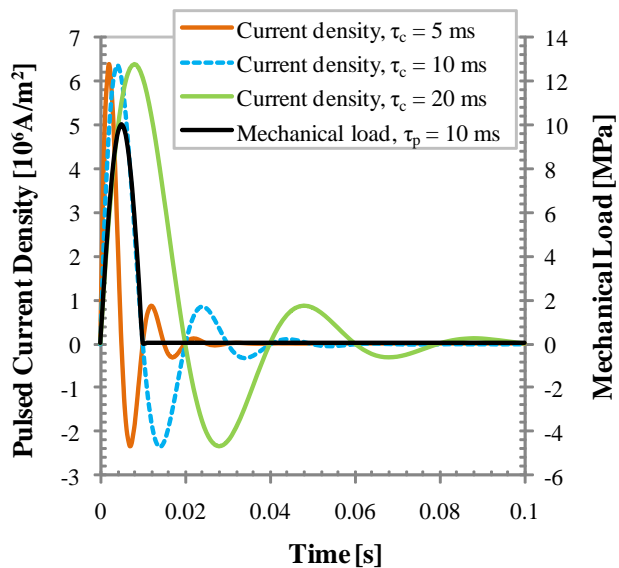
Figure 23. Mechanical load and density of the pulsed electric currents as functions of time.
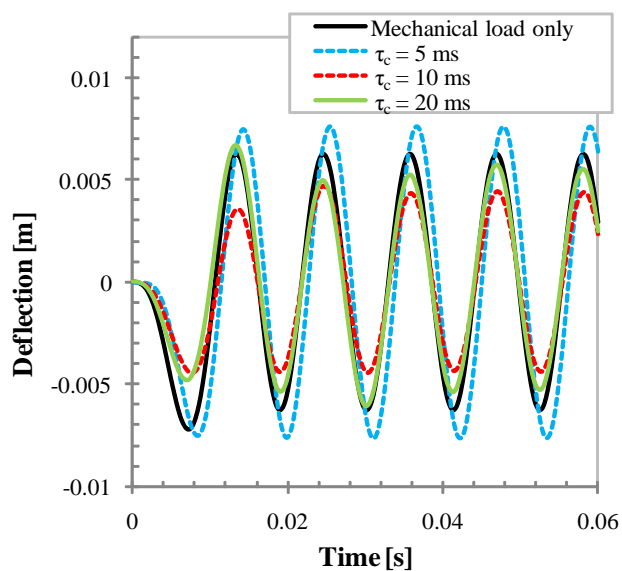
Figure 24. Plate's deflection as a function of time: effect of the electric current waveform ($J_0 = 10^7$ A/m^2, $B_y^* = 0.1$ T, $p_0 = 10$ MPa).

As one can see, electric current waveform has a noticeable effect on the plate deflection. It changes the plate's response during the time of application of the impact load ($t \leq \tau_p = 10$ ms), reduces the amplitude of the subsequent vibrations, and slightly changes the frequency of vibrations. The maximum reduction in deflection occurs when application of the mechanical load is coordinated with application of the pulsed electric current, i.e., $\tau_c = \tau_p$. Figure 25 gives a close-up view of the plate's middle plane deflection, w, at $y = 0$ for the first 10 ms (i.e., presumable impact event).
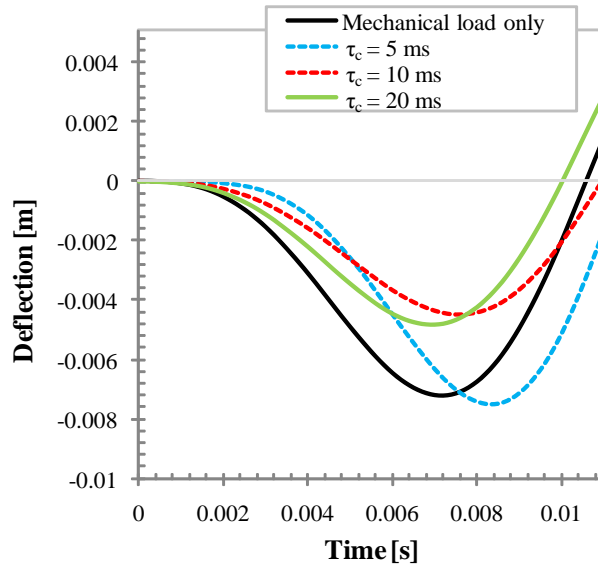
Figure 25. Plate's deflection as a function of time: effect of the electric current waveform on the impact response for
$t \leq \tau_p = 10$ ms ($J_0 = 10^7$ A/m^2, $B_y^* = 0.1$ T, $p_0 = 10$ MPa).

External in-plane magnetic field $\mathbf{B}^* = \left(0, B_y^*, 0\right)$ also alters the mechanical response of the plate. Figure 26 shows the deflection w at the center of the plate ($y = 0$) as a function of time for the magnetic fields of different intensity ($B_y^* = 0.1$ T , $B_y^* = 1.0$ T ,

and $B_y^* = 2.0$ T). In all three cases, the electric current density is determined by (5-10),

where $J_0 = 10^5$ A/m^2 , $\tau_c = \tau_p = 10$ ms .
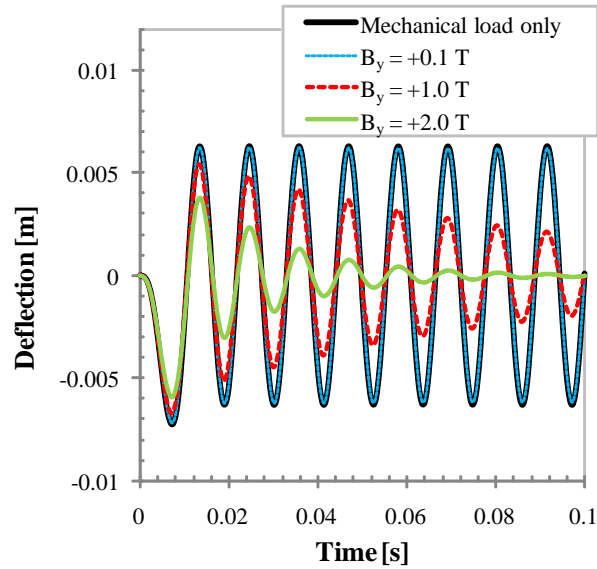
Figure 26. Plate's deflection as a function of time: damping effect of the magnetic field
($J_0 = 10^5$ A/m^2 , $\tau_c = \tau_p = 10$ ms, $p_0 = 10$ MPa).

Note that in Fig. 26, the "mechanical load only" case is practically
indistinguishable from the case with $B_y^* = 0.1$ T . Figure 26 shows that an increase in the
magnetic induction tends to reduce the amplitude of vibrations of the plate with a trend
towards a more rapid decay at the higher induction magnitudes. The observed results are
independent of the magnitude of the electric current density and will prevail if the electric
current density increases. The damping effect is attributed to the two-way electro-
magneto-mechanical terms in the Lorentz force (3-7) that couple magnetic induction and
velocity terms and that increase with an increase in the magnetic induction or velocity. If

these terms are omitted from the Lorentz force, there will be no evident decay in the amplitude of the vibrations. This is shown in Fig. 27, where impact responses of the plate for one-way and two-way electro-magneto-mechanical couplings are compared.
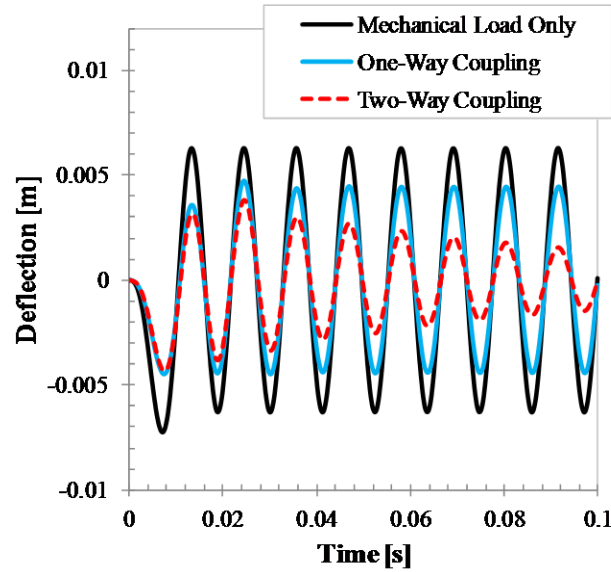
Figure 27. Damping effect of the external magnetic field ($p_0 = 10$ MPa, $J_0 = 10^6$ A/m^2, $\tau_c = \tau_p = 10$ ms, and $B_y^* = 1.0$ T).

The characteristics of the electromagnetic field are $p_0 = 10$ MPa, $J_0 = 10^6$ A/m^2, $\tau_c = \tau_p = 10$ ms, and $B_y^* = 1.0$ T. For the one-way coupling case, the mechanical field has no effects on the Lorentz force, which means:

$$\mathbf{F}^L = \mathbf{J} \times \mathbf{B} .$$

$$(5\text{-}21)$$

It can be seen that the damping effect occurs only in presence of the two-way coupling terms. However, this is barely noticeable if small values of the external

magnetic induction are used, as shown in Fig. 28. Here, $p_0 = 10$ MPa, $J_0 = 10^7$ A/m^2,
$\tau_c = \tau_p = 10$ ms, and $B_y^* = 0.1$ T. Thus, the magnitude of the magnetic field plays an
important role in the damping of the vibrations of the plate over time.
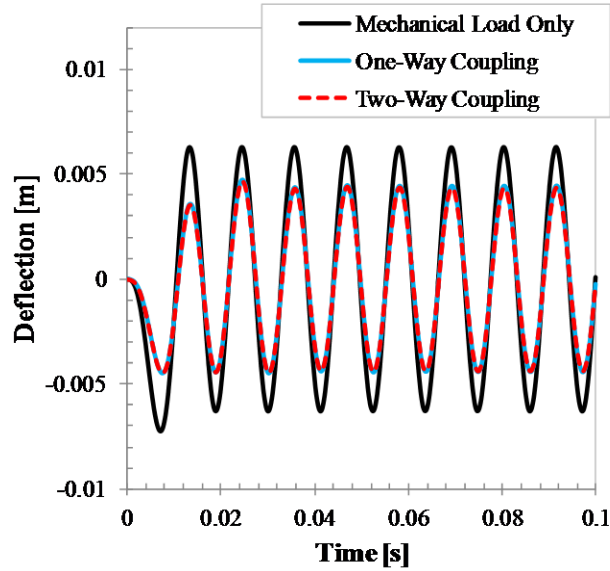
Figure 28. Negligible damping effect for a small magnetic field ($p_0 = 10$ MPa,
$J_0 = 10^7$ A/m^2, $\tau_c = \tau_p = 10$ ms, and $B_y^* = 0.1$ T; the two curves coincide).

As for the electrical conductivity, its effect on the plate response is similar to the
effect of the magnetic induction: an increase in the electrical conductivity leads to a
decay in the amplitude of the plate vibrations over time. The decay becomes more
pronounced at the stronger magnetic fields, which themselves induce damping
independently of the conductivity. This is an expected result that can be directly inferred
from the analysis of the Lorentz force (3-7). The effect of the electrical conductivity on
the short term-response of the plate is negligible when the magnetic field is relatively

low. For instance, there is no further improvement in the response of the plate subjected

to the mechanical and electromagnetic ($J_0 = 10^6$ A/m^2, $\tau_c = \tau_p = 10$ ms, $B_y^* = 0.1$ T) loads,

even when the conductivity is increased hundred times

($\sigma_x = 100\,\sigma_{composite} = 3900000$ S/m), as shown in Fig. 29. The results are shown for two

different electrical conductivity values: $\sigma_x = \sigma_{composite} = 39000$ S/m, which corresponds to

the AS4/3501-6 unidirectional carbon fiber reinforced polymer matrix composite with

60% fiber volume fraction, and $\sigma_x = 100\,\sigma_{composite} = 3900000$ S/m.
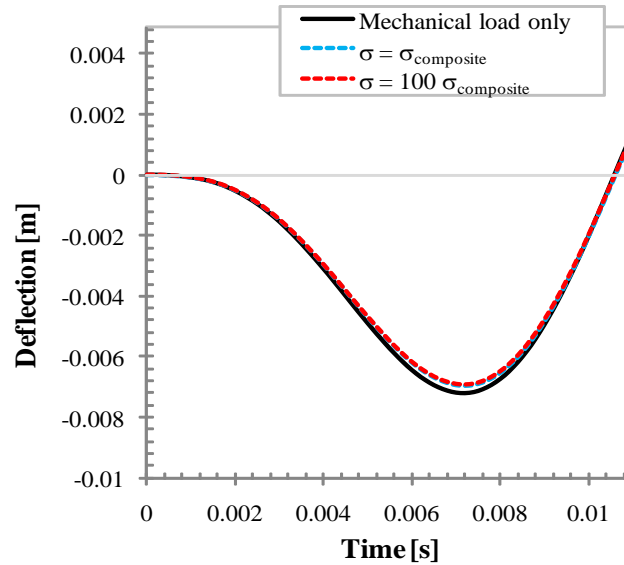
Figure 29. Plate's deflection as a function of time: effect of the electrical conductivity at $J_0 = 10^6$ A/m^2, $\tau_c = \tau_p = 10$ ms, $B_y^* = 0.1$ T, $p_0 = 10$ MPa (blue and red curves coincide).

As the magnetic field increases, the effect of the electrical conductivity becomes

more prominent, even for relatively low electric current densities. Figure 30 shows the

effect of the electrical conductivity on the middle plane deflection, w, at $y = 0$. The

characteristics of the electromagnetic field are $J_0 = 10^5$ A/m^2, $\tau_c = \tau_p = 10$ ms, $B_y^* = 0.5$ T. The electrical conductivity values are $\sigma_x = \sigma_{composite} = 39000$ S/m, which corresponds to the AS4/3501-6 unidirectional carbon fiber reinforced polymer matrix composite with 60% fiber volume fraction, and $\sigma_x = 100\,\sigma_{composite} = 3900000$ S/m.
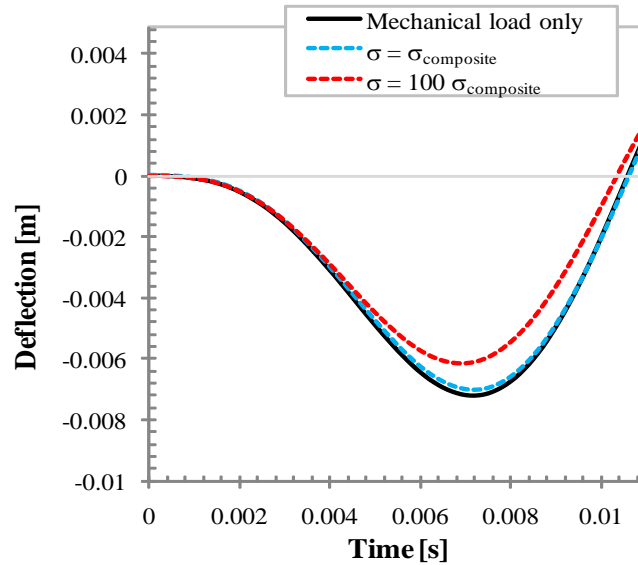
Figure 30. Plate's deflection as a function of time: effect of the electrical conductivity at $J_0 = 10^5$ A/m^2, $\tau_c = \tau_p = 10$ ms, $B_y^* = 0.5$ T, $p_0 = 10$ MPa.

As for the electric current density, an increase in the current density tends to decrease the amplitude of the plate vibrations. Moreover, the effect of the electric current density becomes more pronounced as the magnetic field intensity increases. Figures 31 and 32 illustrate the results. Figure 31 shows the middle plane deflection, w, at $y = 0$. The characteristics of the electromagnetic field are $J_0 = 10^5$ A/m^2, $J_0 = 10^6$ A/m^2 and $J_0 = 10^7$ A/m^2 at $\tau_c = \tau_p = 10$ ms. The magnetic induction is the same for all three

different current densities $B_y^* = 0.1\,\text{T}$. Figure 32 shows the middle plane deflection, w, at $y = 0$. The characteristics of the electromagnetic field are $J_0 = 10^5\ \text{A}/\text{m}^2$, $J_0 = 10^6\ \text{A}/\text{m}^2$ and $J_0 = 2 \cdot 10^6\ \text{A}/\text{m}^2$ at $\tau_c = \tau_p = 10\,\text{ms}$. The magnetic induction once again is the same for all three different current densities, $B_y^* = 1.0\,\text{T}$.

Stress state in the plate subjected to impact load and pulsed electromagnetic load was also investigated in this work. Figures 33 and 34 show contour plots of the normalized normal stress, τ_{yy}/p_0, of the plate subjected to the mechanical load only ($p_0 = 10\,\text{MPa}$, $\tau_p = 10\,\text{ms}$) and subjected to the mechanical load ($p_0 = 10\,\text{MPa}$, $\tau_p = 10\,\text{ms}$) combined with the electromagnetic load ($J_0 = 10^5\ \text{A/m}^2$, $\tau_c = \tau_p = 10\,\text{ms}$, $B_y^* = 1.0\,\text{T}$), respectively. Stress is shown through the thickness of the plate, z/h, and with respect to time, t, at $y = 0$.
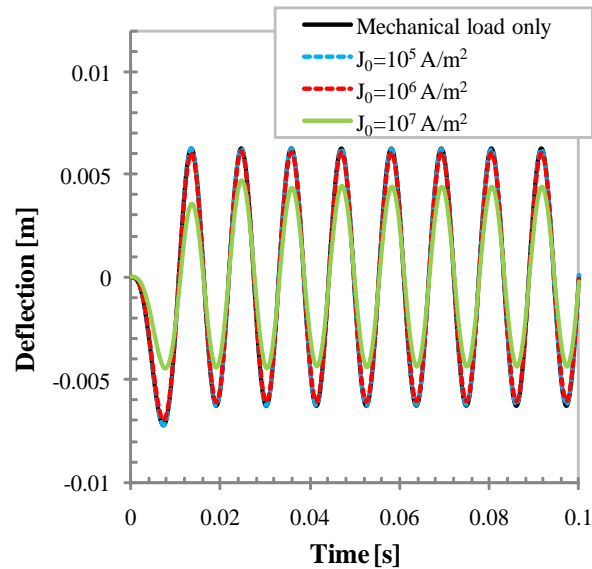
Figure 31. Plate's deflection as a function of time: effect of the electric current density at the low magnetic field, $B_y^* = 0.1\,\text{T}$ (black, blue, and red curves coincide).
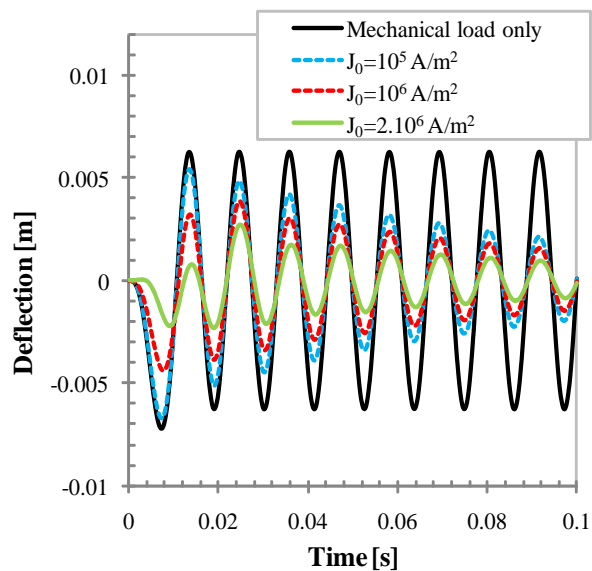
Figure 32. Plate's deflection as a function of time: effect of the electric current density at the strong magnetic field, $B_y^* = 1.0$ T .
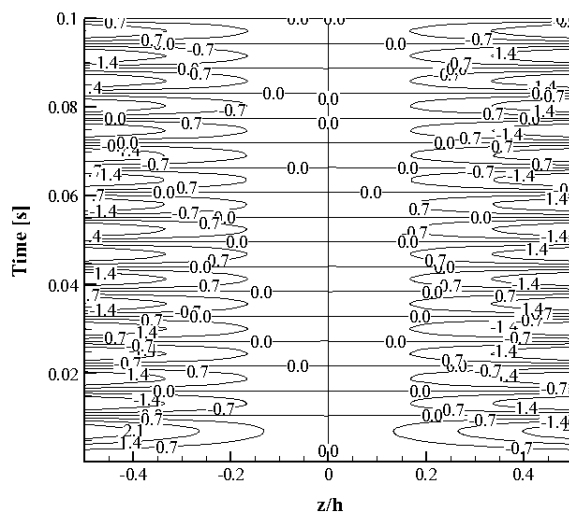
Figure 33. Contours of the stress τ_{yy}/p_0 at $y = 0$ of the plate subjected to the mechanical load only ($p_0 = 10$ MPa, $\tau_p = 10$ ms).
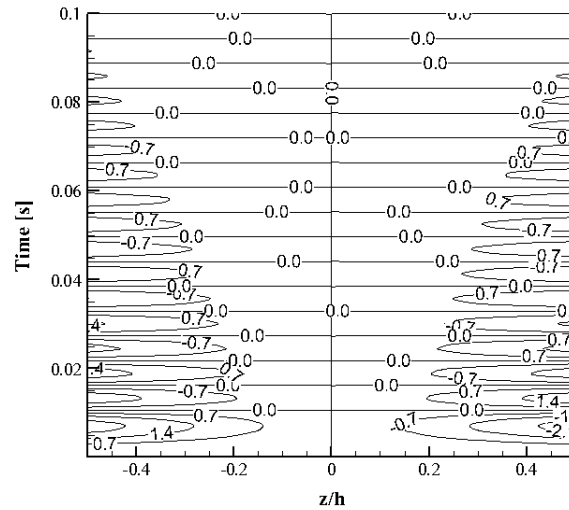
Figure 34. Contours of the stress τ_{yy}/p_0 at the $y = 0$ of the plate subjected to the mechanical and electromagnetic loads ($p_0 = 10$ MPa, $J_0 = 10^5$ A/m^2, $\tau_c = \tau_p = 10$ ms, $B_y^* = 1.0$ T).

As one can see, there is a significant reduction in stress over time, when the electromagnetic load is applied, which is consistent with the vibrations decay shown in Fig. 26.

The distribution of the stress τ_{yy}/p_0 over the cross-section of the plate at the moment of time when the stress is maximum ($t = 7$ ms) for the case, when both mechanical ($p_0 = 10.0$ MPa , $\tau_p = 10$ ms) and electromagnetic ($J_0 = 10^5$ A/m^2 , $\tau_c = \tau_p = 10$ ms , $B_y^* = 1.0$ T) loads are applied, is shown in Fig. 35.

As expected, the stress distribution is antisymmetric with respect to the middle plane of the plate ($z = 0$) with the maximum and minimum stresses of the same magnitude reached at the top and bottom of the plate at $y = 0$, respectively. In the case when only mechanical load is applied to the plate, the pattern of the stress distribution is similar to that shown in Fig. 35, but the stress magnitudes are larger. This shows that the

application of an appropriate electromagnetic load to the anisotropic plate can reduce the stresses caused by an impact load.
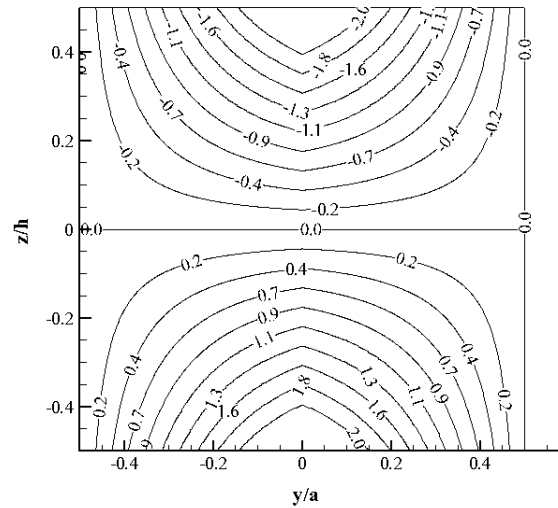
Figure 35. Contours of the stress τ_{yy}/p_0 at $t = 7\,\text{ms}$ when both mechanical and electromagnetic loads are applied ($p_0 = 10\,\text{MPa}$, $J_0 = 10^5\,\text{A/m}^2$, $\tau_c = \tau_p = 10\,\text{ms}$, $B_y^* = 1.0\,\text{T}$).

5.3 Two-Dimensional Finite Plate

5.3.1 Governing Equations and Numerical Solution

Procedure

From the 2D approximation of Maxwell's equations (3-37) and in absence of the external magnetic induction in x-direction, that is $B_x^{\pm} = 0$, the expression for E_y can be obtained as:

$$E_y = \frac{\partial u}{\partial t} B_z - \frac{1}{\sigma_y \mu} \frac{\partial B_z}{\partial x} \tag{5-22}$$

Moreover, the resultants N_{xx}, N_{xz}, M_{xx} and M_{xy} can be written in terms of other variables as:

$$N_{xx} = \frac{B_{12}}{B_{22}} N_{yy} + (B_{11} - \frac{B_{12}^2}{B_{22}})h \frac{\partial u}{\partial x} - A_1 \int_{-\frac{h}{2}}^{\frac{h}{2}} \tau_{zz} dz,$$

$$N_{xz} = \frac{\rho h^3}{12} \frac{\partial^3 w}{\partial x \partial t^2} + \left(\frac{B_{12}}{B_{22}} + \frac{2 B_{66}}{B_{22}} \right) \frac{\partial M_{yy}}{\partial x} + \frac{h^3}{12} \left(\frac{2 B_{66} B_{12}}{B_{22}} - B_{11} + \frac{B_{12}^2}{B_{22}} \right) \frac{\partial^3 w}{\partial x^3}$$

$$- A_1 \int_{-\frac{h}{2}}^{\frac{h}{2}} \frac{\partial \tau_{zz}}{\partial x} z dz + \rho \int_{-\frac{h}{2}}^{\frac{h}{2}} F_x^L z dz, \tag{5-23}$$

$$M_{xx} = \frac{B_{12}}{B_{22}} M_{yy} - \frac{h^3}{12} (B_{11} - \frac{B_{12}^2}{B_{22}}) \frac{\partial^2 w}{\partial x^2} - A_1 \int_{-\frac{h}{2}}^{\frac{h}{2}} \tau_{zz} z dz,$$

$$M_{xy} = -\frac{h^3}{6} B_{66} \frac{\partial W}{\partial x}.$$

Therefore, considering the type of loading on the plate and ignoring the small terms which contain $(\varepsilon_y - \varepsilon_0)$, the system of equations for a 2D plate reads as

$$\frac{\partial u}{\partial y} = \frac{1}{h B_{66}} N_{xy} - \frac{\partial v}{\partial x},$$

$$\frac{\partial v}{\partial y} = \frac{1}{h B_{22}} N_{yy} - \frac{B_{12}}{B_{22}} \frac{\partial u}{\partial x},$$

$$\frac{\partial N_{xy}}{\partial y} = \rho h \frac{\partial^2 u}{\partial t^2} - \frac{B_{12}}{B_{22}} \frac{\partial N_{yy}}{\partial x} - (B_{11} - \frac{B_{12}^2}{B_{22}})h \frac{\partial^2 u}{\partial x^2} + \frac{h}{\mu} \frac{\partial B_z}{\partial x} B_z \tag{5-24}$$

$$+ \frac{h}{4} \sigma_z \left(B_{y1}^2 + \frac{1}{3} B_{y2}^2 \right) \frac{\partial u}{\partial t} - \frac{h^2}{12} \sigma_z B_{y1} B_{y2} \frac{\partial^2 w}{\partial x \partial t} + (\varepsilon_x - \varepsilon_0) h E_x B_z \frac{\partial^2 v}{\partial x \partial t}$$

$$- \frac{h}{2} (\varepsilon_x - \varepsilon_0) B_{y1} E_x \frac{\partial^2 w}{\partial x \partial t},$$

$$\frac{\partial N_{yy}}{\partial y} = \rho h \frac{\partial^2 v}{\partial t^2} - \frac{\partial N_{xy}}{\partial x} + \sigma_x h B_z^2 \frac{\partial v}{\partial t} - \frac{h}{2} \sigma_x B_{y1} B_z \frac{\partial w}{\partial t} + \frac{\varepsilon_x - \varepsilon_0}{B_{22}} E_x B_z \frac{\partial N_{yy}}{\partial t}$$

$$- (\varepsilon_x - \varepsilon_0) h \frac{B_{12}}{B_{22}} E_x B_z \frac{\partial^2 u}{\partial x \partial t} - \frac{h}{2}(\varepsilon_x - \varepsilon_0) B_{y1} E_x \frac{\partial W}{\partial t} + \sigma_x h E_x B_z + h B_z J_x^*(t),$$

$$\frac{\partial w}{\partial y} = W,$$

$$\frac{\partial W}{\partial y} = -\frac{12}{h^3 B_{22}} M_{yy} - \frac{B_{12}}{B_{22}} \frac{\partial^2 w}{\partial x^2},$$

$$\frac{\partial M_{yy}}{\partial y} = -\frac{\rho h^3}{12} \frac{\partial^2 W}{\partial t^2} + N_{yz} + \frac{h^3}{6} B_{66} \frac{\partial^2 W}{\partial x^2} - \frac{h^2}{12} \sigma_x B_z B_{y2} \frac{\partial w}{\partial t} - \frac{h^3}{12} \sigma_x B_z^2 \frac{\partial W}{\partial t}$$

$$- \frac{1}{12}(\varepsilon_x - \varepsilon_0) h^2 E_x B_{y2} \frac{\partial W}{\partial t} + \frac{(\varepsilon_x - \varepsilon_0)}{B_{22}} E_x B_z \frac{\partial M_{yy}}{\partial t}$$

$$+ \frac{h^3}{12} \frac{B_{12}}{B_{22}}(\varepsilon_x - \varepsilon_0) E_x B_z \frac{\partial^3 w}{\partial x^2 \partial t},$$

$$\frac{\partial N_{yz}}{\partial y} = \rho h \frac{\partial^2 w}{\partial t^2} + p(y,t) - \frac{h}{2} \sigma_x E_x B_{y1} - \frac{h}{2} \sigma_x B_{y1} B_z \frac{\partial v}{\partial t} + \frac{h}{4} \sigma_x \left(B_{y1}^2 + \frac{1}{3} B_{y2}^2 \right) \frac{\partial w}{\partial t}$$

$$+ \frac{h^2}{12} \sigma_x B_z B_{y2} \frac{\partial W}{\partial t} - (\varepsilon_x - \varepsilon_0) h E_x B_z \frac{\partial W}{\partial t} - \frac{h}{2} B_{y1} J_x^*(t) - \frac{\rho h^3}{12} \frac{\partial^4 w}{\partial x^2 \partial t^2}$$

$$- \left(\frac{B_{12}}{B_{22}} + \frac{2 B_{66}}{B_{22}} \right) \frac{\partial^2 M_{yy}}{\partial x^2} - \frac{h^3}{12} \left(\frac{2 B_{66} B_{12}}{B_{22}} - B_{11} + \frac{B_{12}^2}{B_{22}} \right) \frac{\partial^4 w}{\partial x^4}$$

$$- \frac{h^3}{12} \left(\sigma_y B_z^2 + \frac{1}{4} \sigma_z B_{y1}^2 \right) \frac{\partial^3 w}{\partial x^2 \partial t} - \frac{h^3}{2} \left(\frac{1}{3} \sigma_y B_z \frac{\partial B_z}{\partial x} + \frac{1}{40} \sigma_z B_{y2}^2 \right) \frac{\partial^2 w}{\partial x \partial t}$$

$$+ \frac{h^2}{12} \sigma_z B_{y1} B_{y2} \frac{\partial^2 u}{\partial x \partial t} - \frac{h^3}{12}(\varepsilon_x - \varepsilon_0) \left(B_z \frac{\partial E_x}{\partial x} + E_x \frac{\partial B_z}{\partial x} \right) \frac{\partial^2 W}{\partial x \partial t}$$

$$- \frac{h^3}{12}(\varepsilon_x - \varepsilon_0) E_x B_z \frac{\partial^3 W}{\partial x^2 \partial t} - \frac{h^2}{12}(\varepsilon_x - \varepsilon_0) B_{y2} \left(\frac{\partial E_x}{\partial x} \frac{\partial^2 w}{\partial x \partial t} + E_x \frac{\partial^3 w}{\partial x^2 \partial t} \right),$$

$$\frac{\partial E_x}{\partial y} = \frac{\partial B_z}{\partial t} + \frac{\partial u}{\partial t} \frac{\partial B_z}{\partial x} + \frac{\partial^2 u}{\partial t \partial x} B_z - \frac{1}{\sigma_y \mu} \frac{\partial^2 B_z}{\partial x^2},$$

$$\frac{\partial B_z}{\partial y} = \sigma_x \mu E_x + \sigma_x \mu \frac{\partial v}{\partial t} B_z - \sigma_x \mu \frac{B_{y1}}{2} \frac{\partial w}{\partial t} + \frac{B_{y2}}{h}.$$

which include eight mechanical and two electromagnetic variables. This system can be rewritten in the vector form (4-2), where the unknown vector $\mathbf{g}$ stands for

$$\mathbf{g} = \left[u, v, N_{xy}, N_{yy}, w, W, M_{yy}, N_{yz}, E_x, B_z \right]^T.$$

(5-25)

in which the order of the variables was selected such that the resulting matrix of coefficients of the system is close to a band matrix: first the four in-plane displacements and resultants followed by the four out-of-plane unknowns, and finally, the two electromagnetic variables. This is helpful to yield a less ill-conditioned matrix of coefficients.

The method of lines discussed in Section 4.4 is now applied to the system of (5-24) to discretize one of the spatial independent variables (x). To do so, all the derivatives with respect to x are replaced with the corresponding finite difference approximations (4-20). The plate is partitioned in the x-direction by n_x number of lines where $x = \pm l/2$ are the boundary lines, the line $x = -l/2 + \Delta x$ is the first line $i = 1$ and the line $x = +l/2 - \Delta x$ is the last line $i = n_x$. After applying the method of lines, the final vector of unknowns reads as:

$$\begin{aligned}
\mathbf{g} = [& u^1, v^1, N_{xy}^1, N_{yy}^1, w^1, W^1, M_{yy}^1, N_{yz}^1, E_x^1, B_z^1, \\
& u^2, v^2, N_{xy}^2, N_{yy}^2, w^2, W^2, M_{yy}^2, N_{yz}^2, E_x^2, B_z^2, \ldots, \\
& u^{n_x}, v^{n_x}, N_{xy}^{n_x}, N_{yy}^{n_x}, w^{n_x}, W^{n_x}, M_{yy}^{n_x}, N_{yz}^{n_x}, E_x^{n_x}, B_z^{n_x}]^T.
\end{aligned}$$

(5-26)

The boundary conditions for $x = \pm l/2$ need to be applied manually to the adjacent lines in the system of equations. Therefore, the PDEs system of (5-24) is now reduced to a system of ODEs that can be solved by the same numerical procedure used for the 1D case: MOL is followed by the Newmark's time integration and quasilinearization. Then the resulting linear system of ODEs is integrated in y-direction while orthonormalization is applied which yields the final solution over the plate.

The $5n_x$ homogeneous and one non-homogenous initial vectors for the 2D problem are:

$$\mathbf{N}_{1,i}^{\text{hom}} = \left[\overbrace{0, ..., 0}^{10(i-1)}, 0, 0, 1, 0, 0, 0, 0, 0, 0, \overbrace{0, ..., 0}^{10(n_x-i)} \right]^T ,$$

$$\mathbf{N}_{2,i}^{\text{hom}} = \left[\overbrace{0, ..., 0}^{10(i-1)}, 0, 0, 0, 1, 0, 0, 0, 0, 0, 0, \overbrace{0, ..., 0}^{10(n_x-i)} \right]^T ,$$

$$\mathbf{N}_{3,i}^{\text{hom}} = \left[\overbrace{0, ..., 0}^{10(i-1)}, 0, 0, 0, 0, 0, 1, 0, 0, 0, 0, \overbrace{0, ..., 0}^{10(n_x-i)} \right]^T , \qquad (5\text{-}27)$$

$$\mathbf{N}_{4,i}^{\text{hom}} = \left[\overbrace{0, ..., 0}^{10(i-1)}, 0, 0, 0, 0, 0, 0, 0, 1, 0, 0, \overbrace{0, ..., 0}^{10(n_x-i)} \right]^T ,$$

$$\mathbf{N}_{5,i}^{\text{hom}} = \left[\overbrace{0, ..., 0}^{10(i-1)}, 0, 0, 0, 0, 0, 0, \frac{g_2^k}{2\beta\Delta t} + \zeta_2, -1, \overbrace{0, ..., 0}^{10(n_x-i)} \right]^T ,$$

$$\mathbf{N}^{non\,\text{hom}} = \left[\overbrace{0, ..., 0}^{10(i-1)}, 0, 0, 0, 0, 0, 0, \zeta_2 g_{10}^k - \zeta_5 B_y^*, -g_{10}^k, \overbrace{0, ..., 0}^{10(n_x-i)} \right]^T .$$

The boundary conditions for the finite 2D plate are defined as follows: at $y = \pm a/2$, similar to 1D problem, the plate is simply-supported:

$$u_x\big|_{y=\pm\frac{a}{2}} = u_y\big|_{y=\pm\frac{a}{2}} = u_z\big|_{y=\pm\frac{a}{2}} = M_{yy}\big|_{y=\pm\frac{a}{2}} = 0, \qquad (5\text{-}28)$$

and the electromagnetic boundary conditions the same as (5-5). As a results, the matrices $\mathbf{D}_1$ and $\mathbf{D}_2$, and vectors $\mathbf{d}_1$ and $\mathbf{d}_2$ in (4-4) for the 2D problem become:

$$\mathbf{D}_1 = \begin{bmatrix} \mathbf{A}_1, & \mathbf{0}, & \dots, & \mathbf{0} \\ \mathbf{0}, & \mathbf{A}_1, & \cdots, & \mathbf{0} \\ \vdots & & \ddots & \vdots \\ \mathbf{0}, & \cdots, & \mathbf{0}, & \mathbf{A}_1 \end{bmatrix}, \quad \mathbf{D}_2 = \begin{bmatrix} \mathbf{A}_2, & \mathbf{0}, & \dots, & \mathbf{0} \\ \mathbf{0}, & \mathbf{A}_2, & \cdots, & \mathbf{0} \\ \vdots & & \ddots & \vdots \\ \mathbf{0}, & \cdots, & \mathbf{0}, & \mathbf{A}_2 \end{bmatrix}, \tag{5-29}$$

$$\mathbf{d}_1 = \begin{bmatrix} \mathbf{a}_1, \mathbf{a}_1, \cdots, \mathbf{a}_1 \end{bmatrix}^T, \qquad \mathbf{d}_2 = \begin{bmatrix} \mathbf{a}_2, \mathbf{a}_2, \cdots, \mathbf{a}_2 \end{bmatrix}^T,$$

where $\mathbf{D}_1$ and $\mathbf{D}_2$ are matrices of the size $5n_x \times 5n_x$, $\mathbf{d}_1$ and $\mathbf{d}_2$ are vectors of the size $5n_x$ in which

$$\mathbf{A}_1 = \begin{bmatrix} 1, & 0, & 0, & 0, & 0, & 0, & 0, & 0, & 0, & 0 \\ 0, & 1, & 0, & 0, & 0, & 0, & 0, & 0, & 0, & 0 \\ 0, & 0, & 0, & 0, & 1, & 0, & 0, & 0, & 0, & 0 \\ 0, & 0, & 0, & 0, & 0, & 0, & 1, & 0, & 0, & 0 \\ 0, & \dfrac{g_{10}^k}{2\beta\Delta t}, & 0, & 0, & \dfrac{-B_y^*}{2\beta\Delta t}, & 0, & 0, & 0, & 1, & \dfrac{g_1^k}{2\beta\Delta t}+\zeta_1 \end{bmatrix}, \tag{5-30}$$

$$\mathbf{A}_2 = \begin{bmatrix} 1, & 0, & 0, & 0, & 0, & 0, & 0, & 0 \\ 0, & 1, & 0, & 0, & 0, & 0, & 0, & 0 \\ 0, & 0, & 0, & 0, & 0, & 1, & 0, & 0 \\ 0, & 0, & 0, & 0, & 0, & 0, & 1, & 0 \end{bmatrix},$$

$$\mathbf{a}_1 = \left[0, 0, 0, 0, -B_y^*\zeta_2 - \dfrac{g_1^k g_8^k}{2\beta\Delta t} \right]^T, \qquad \mathbf{a}_2 = \begin{bmatrix} 0, 0, 0, 0, 0 \end{bmatrix}^T.$$

The mechanical and electromagnetic boundary conditions at $x = \pm l/2$ are:

$$u_x\big|_{x=\pm\frac{l}{2}} = u_y\big|_{x=\pm\frac{l}{2}} = u_z\big|_{x=\pm\frac{l}{2}} = M_{xx}\big|_{x=\pm\frac{l}{2}} = 0,$$
$$E_y\big|_{x=\pm\frac{l}{2}} = 0. \tag{5-31}$$

The boundary conditions in (5-31) results in the following values of other variables at $x = \pm l/2$:

$$N_{xy}\big|_{x=-\frac{l}{2}} = hB_{66}\frac{v^1}{\Delta x}, \qquad N_{xy}\big|_{x=+\frac{l}{2}} = -hB_{66}\frac{v^{n_x}}{\Delta x},$$

$$N_{yy}\big|_{x=-\frac{l}{2}} = hB_{12}\frac{u^1}{\Delta x}, \qquad N_{yy}\big|_{x=+\frac{l}{2}} = -hB_{12}\frac{u^{n_x}}{\Delta x},$$

$$M_{yy}\big|_{x=-\frac{l}{2}} = \frac{h^3}{12}\left(\frac{B_{11}B_{22}}{B_{12}} - B_{12}\right)\frac{1}{\Delta x^2}(w^2 - 2w^1),$$

$$M_{yy}\big|_{x=+\frac{l}{2}} = -\frac{h^3}{12}\left(\frac{B_{11}B_{22}}{B_{12}} - B_{12}\right)\frac{1}{\Delta x^2}(w^{n_x-2} - 2w^{n_x-1}), \tag{5-32}$$

$$W\big|_{x=\pm\frac{l}{2}} = 0,$$

$$E_x\big|_{x=-\frac{l}{2}} = E_x^1, \qquad E_x\big|_{x=+\frac{l}{2}} = E_x^{n_x},$$

$$B_z\big|_{x=-\frac{l}{2}} = B_z^1, \qquad B_z\big|_{x=+\frac{l}{2}} = B_z^{n_x}.$$

Next section discusses the validation of the presented numerical solution procedure followed by the numerical results of the mechanical response of the finite plate.

5.3.2 Validation

To validate the accuracy of the code for a 2D finite plate, the numerical results are compared to known analytical solutions. For the sake of simplicity, only the results for an isotropic plate with the elasticity modulus E and Poisson's ratio v are considered here. The analytical solution for of the vibrations of the center of a simply-supported isotropic plate subjected to a constant transverse load p_0 has the form [139]:

$$w\big|_{x=0,y=0} = \frac{16p_0}{\pi^6 D}\sum_{m=1}^{\infty}\sum_{n=1}^{\infty}\frac{\sin(m\pi/2)\sin(n\pi/2)}{mn\left(\frac{m^2}{l^2} + \frac{n^2}{a^2}\right)^2}\left[1 - \cos(\omega_{mn}t)\right], \tag{5-33}$$

where m and n are odd numbers; l, a, and h are the dimensions of the plate in x-, y-, and z-direction; D is the flexural rigidity of the plate defined as:

$$D = \frac{Eh^3}{12(1 - \nu^2)},$$ (5-34)

and

$$\omega_{mn} = \pi^2 \left(\frac{m^2}{l^2} + \frac{n^2}{a^2} \right) \sqrt{\frac{D}{\rho h}}.$$ (5-35)

is the modal frequency of the vibrations.

If the load is applied in the form of $p_0 \sin(\Omega t)$, the vibration of the center of the simply-supported isotropic plate can be written as [108]:

$$w\big|_{x=0, y=0} = \frac{16 p_0}{\pi^2 \rho h} \sum_{m=1}^{\infty} \sum_{n=1}^{\infty} \frac{\sin(m\pi/2)\sin(n\pi/2)}{mn\left(\omega_{mn}^2 - \Omega^2\right)} \left(\frac{\Omega}{\omega_{mn}} \sin(\omega_{mn}t) - \sin(\Omega t) \right),$$ (5-36)

where m and n are odd numbers.

Analytical results (5-33) and (5-36) have been compared with the numerical results obtained using the numerical solution procedure described in Section 5.3.1. The results of these comparisons are shown in Figs. 36 and 37. The plates under consideration were a square and rectangular ($l = 2a$) plates subjected to a constant transverse compressive load p_0. The material and geometric parameters were as following: Young's modulus $E = 102.97\,\text{GPa}$, Poisson's ratio $\nu = 0.3$, plate width $a = 0.1524\,\text{m}$, plate thickness $h = 0.0021\,\text{m}$, and the constant transverse load $p_0 = 1000\,\text{Pa}$. The following parameters were also taken for the numerical simulations: $n_x = 5$, $n_y = 24000$ and $dt = 0.1\,\text{ms}$. Figure 36 shows numerical and analytical (Eq. (5-33)) solutions for the square plate. Here deflection in the center of the plate ($x = 0$, $y = 0$) is plotted as a function of time.
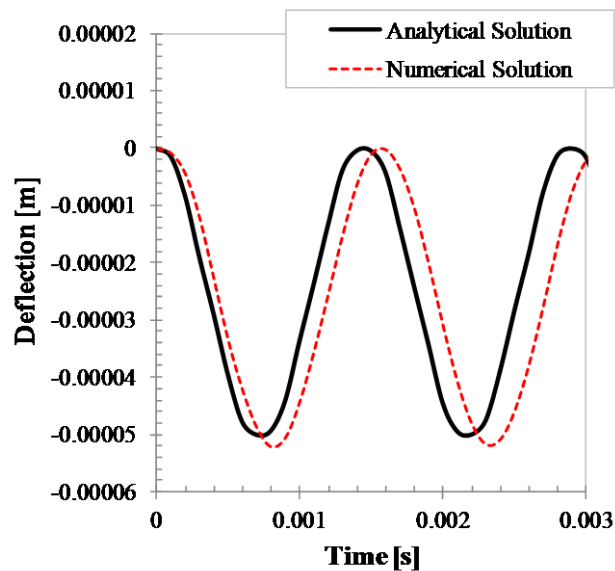
Figure 36. Comparison of the middle plane deflection between analytical and numerical solutions for the square plate: $p_0 = 1\text{kPa}$, $l = a$
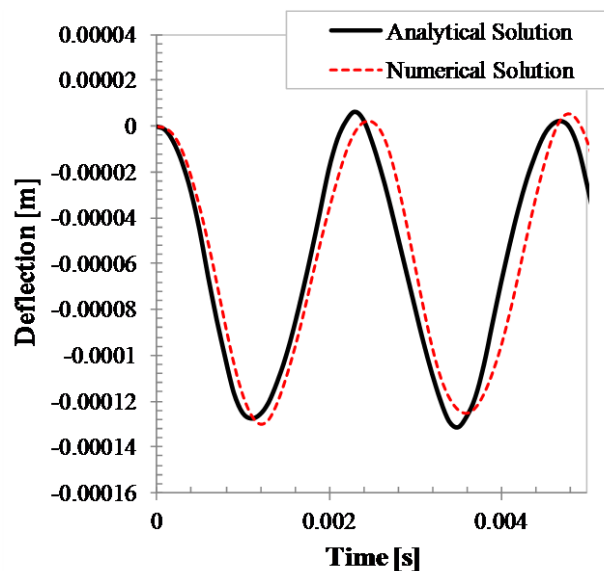
Figure 37. Comparison of the middle plane deflection between analytical and numerical solutions for the rectangular plate: $p_0 = 1\text{kPa}$, $l = 2a$

Figure 37 shows numerical and analytical solutions for the rectangular ($l = 2a$) plate. Deflection in the center of the plate ($x = 0,\ y = 0$) is plotted as a function of time. It can be seen that the amplitudes of vibrations obtained by using the numerical procedure are in a reasonable agreement with the results of the analytical solutions. However, there is noticeable dispersion between the numerical and analytical results because minimum number of lines in the $x-$direction is considered for the numerical procedure (the method of lines). The dispersion can be significantly reduced if the number of lines is increased.

The numerical and analytical (5-36) results for the case of time-dependant load $p_0 \sin(\Omega t)$ are shown in Figs. 38 and 39. The material and geometric parameters of the plates were the same as in the case of the constant transverse load: $E = 102.97\,\text{GPa}$, $v = 0.3$, $a = 0.1524\,\text{m}$, $h = 0.0021\,\text{m}$, and the amplitude of the load $p_0 = 0.1\,\text{MPa}$ and the frequency $\Omega = 100\pi\ \text{rad/s}$. The following parameters were used for the numerical calculations: $n_x = 5$, $n_y = 24000$ and $dt = 0.1\,\text{ms}$. Figure 38 shows the numerical and analytical (5-36) solutions for the square plate. Deflection in the center of the plate ($x = 0,\ y = 0$) is plotted as a function of time.

Figure 39 shows numerical and analytical (5-36) solutions for the rectangular ($l = 2a$) plate. Deflection in the center of the plate ($x = 0,\ y = 0$) is plotted as a function of time.

As it can be seen, the numerical results for both cases of constant and time-dependent loads are in good agreement with the analytical results. It is worth to mention that the pattern of vibrations of the pate subjected to a time-dependant load is a consequence of the interaction between the applied load and natural vibrations of the plate and depends on frequency of the load, aspect ratio of the plate, and its elasticity modulus.
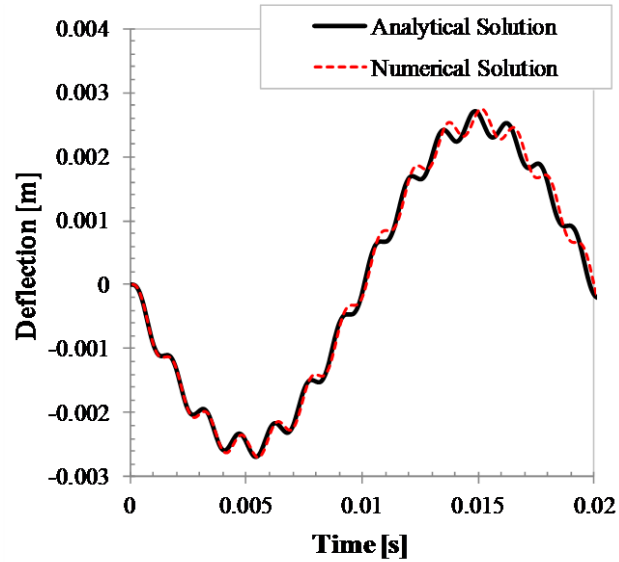
Figure 38. Comparison of the middle plane deflection between analytical and numerical solutions for the square plate: $p_0 = 0.1\,\text{MPa}$ and $\Omega = 100\pi$ rad/s, $l = a$
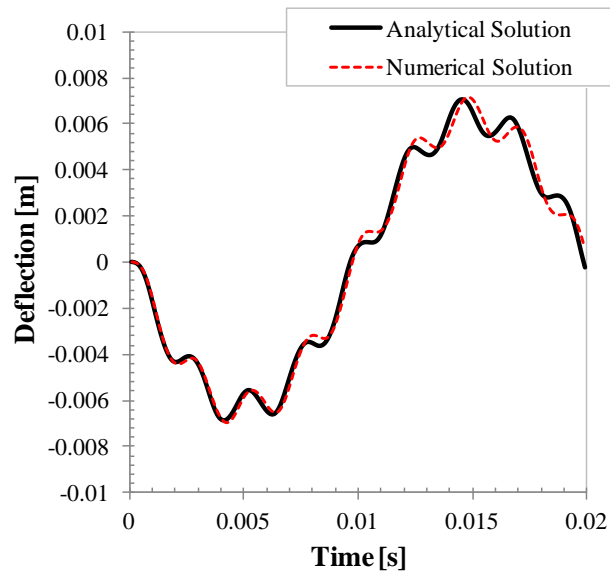
Figure 39. Comparison of the middle plane deflection between analytical and numerical solutions for the square plate: $p_0 = 0.1\,\text{MPa}$ and $\Omega = 100\pi$ rad/s, $l = 2a$

Fig. 40 shows the vibrations of an isotropic plate with different aspect ratios subjected to a time-dependent load $p_0 \sin(\Omega t)$ with $p_0 = 0.1\,\mathrm{MPa}$ and $\Omega = 100\pi\ \mathrm{rad/s}$. The modulus of elasticity of the plate is $E = 7.55\,\mathrm{GPa}$, and $v = 0.3$, $a = 0.1524\,\mathrm{m}$, $h = 0.0021\,\mathrm{m}$. As it can be seen, by increasing the aspect ratio of the plate, the vibrations become smoother. The effect of Young's modulus on the dynamic response of a square plate is shown in Fig. 41. It is shown that the less stiff plate possesses a smoother curve of vibrations which is related to the suppression of the natural vibrations of the plate by the applied load. This observation is clearer if a small enough Young's modulus is considered for the plate as in Fig. 42 in which Young's modulus is $E = 0.755\,\mathrm{GPa}$.
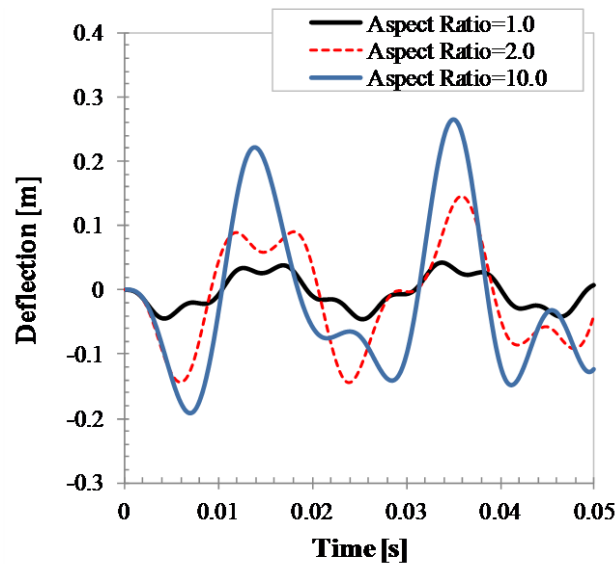
Figure 40. Effect of the aspect ratio on the plate deflection: $p_0 = 0.1\,\mathrm{MPa}$ and $\Omega = 100\pi\ \mathrm{rad/s}$
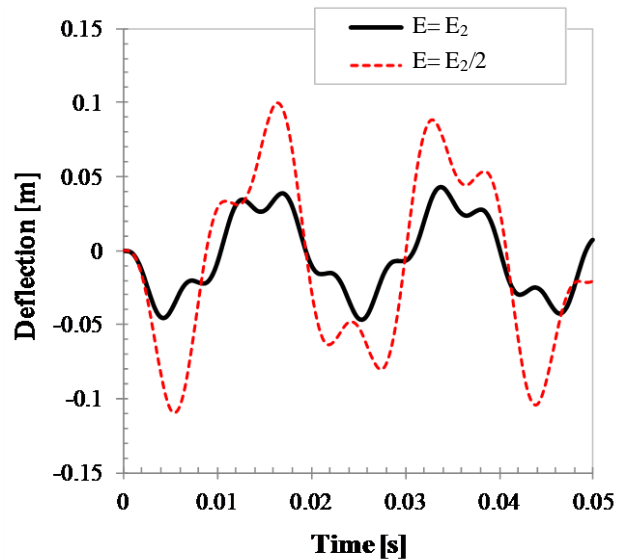
Figure 41. Effect of Young's modulus on the plate deflection: square plate, $p_0 = 0.1\,\text{MPa}$ and $\Omega = 100\pi$ rad/s
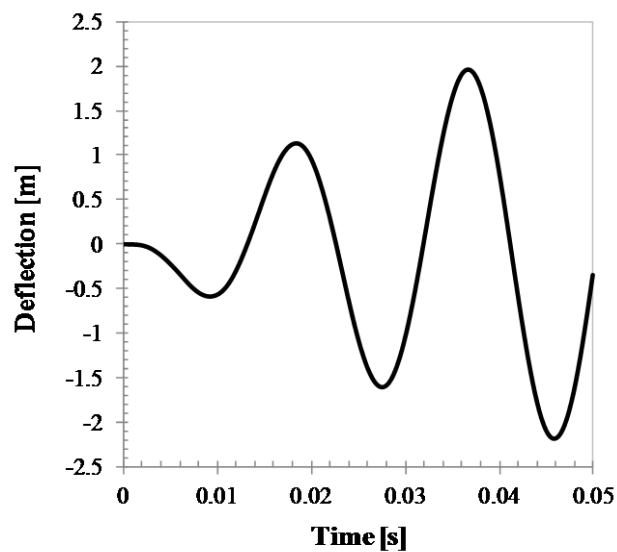
Figure 42. Effect of small Young's modulus on the plate deflection: square plate, $p_0 = 0.1\,\text{MPa}$ and $\Omega = 100\pi$ rad/s, $E = 0.755\,\text{GPa}$

Once the numerical solution procedure for the finite plate was validated, the electro-magneto-mechanical coupling in finite anisotropic electrically conductive plate was studied.

5.3.3 Numerical Results for the Finite Plate

In this section, the results of the numerical studies of the finite rectangular electrically conductive transversely isotropic plate subjected to the mechanical load (5-3) and pulsed electromagnetic loads (5-10) and (5-3) are presented. The plate is shown in Fig. 43. The following plate parameters are considered. The width of the plate is $a = 0.1524\,\text{m}$ and the thickness is $h = 0.0021\,\text{m}$. The plate is assumed to be made of the AS4/3501-6 unidirectional carbon fiber reinforced polymer matrix composite with 60% fiber volume fraction. The material properties of the composite are as follows: density $\rho = 1594\,\text{kg/m}^3$, Young's moduli in fiber direction, $E_x = 102.97\,\text{GPa}$ and in transverse direction, $E_y = 7.55\,\text{GPa}$; Poisson's ratios, $v_{yx} = v_{xz} = 0.3$; electric conductivity in fiber direction, $\sigma_x = 39000\,\text{S/m}$. The electric conductivities of the composite perpendicular to the fiber direction are considered to be $\sigma_y = \sigma_z = 10^{-4}\sigma_x$. The half-size of the contact zone is $b = h/10$. Note that the plate parameters are the same as those for a long plate (see Section 5.2.1), except for b that is $h/10$.

Additional validation of the numerical solution procedure for the finite plate was done by performing computations for a long plate using codes for 2D (finite plate) and 1D (long strip plate) cases. For this purpose, the depth of the plate was chosen to be 10 times larger than its width ($l = 10a$) and the plate was assumed to be subjected to a transient mechanical load described by Eq. (5-3) with the characteristics of $p_0 = 0.1\,\text{MPa}$ and $\tau_p = 10\,\text{ms}$.
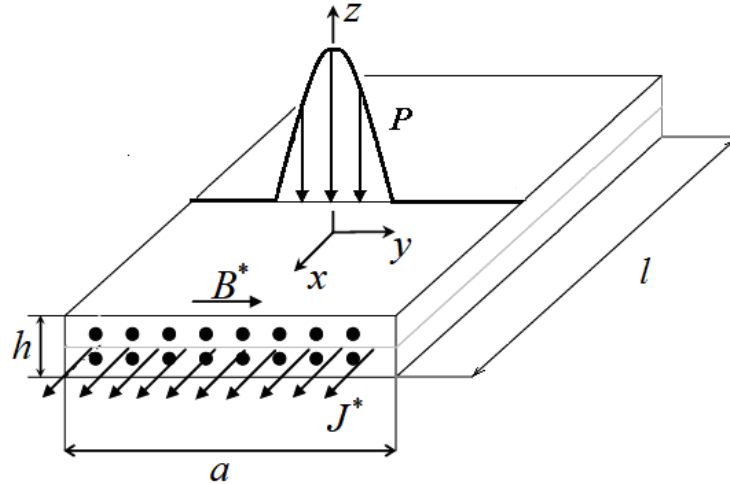
Figure 43. Finite 2D plate subjected to the pulsed electric current, transverse impact load, and immersed in the magnetic field.

In the 1D simulation, the time step was $dt = 10^{-4}$ s and $n_y = 10^5$. For the 2D simulation, same time step was used with $n_y = 10^4$ and $n_x = 5$. The results for middle plane deflections are shown in Fig. 44. As it can be seen, the curves for 1D and 2D cases coincide, from which it can be concluded that the code for simulating the 2D case yields accurate results even with a few number of lines in the x-direction.

Next, the effects of the application of various electromagnetic loads on the mechanical response of the plate have been studied.

The results reported below were obtained for the following parameters. The plate was assumed to be rectangular with $l = 2a$, and the mechanical load (5-3) was such that $p_0 = 1$ MPa, $\tau_p = 10$ ms. The characteristic time of the pulsed electric current was $\tau_c = \tau_p = 10$ ms. Moreover, in all simulations the time step was $dt = 10^{-4}$ s, the number of lines was five, $n_x = 5$, and $n_y = 10^5$.
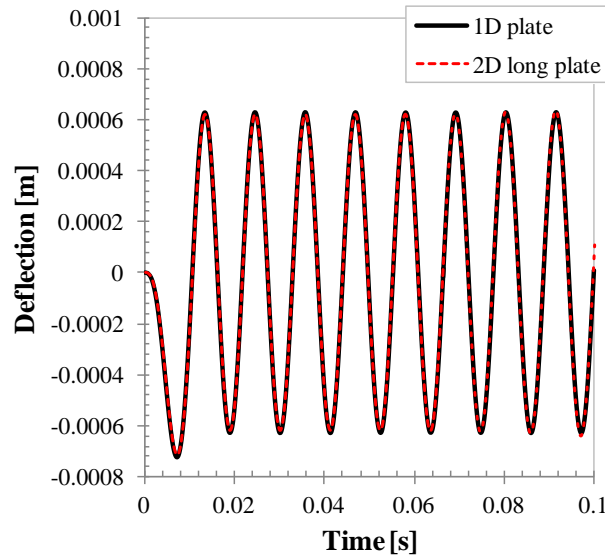
Figure 44. The deflection at the center of the plate over time for the 1D and 2D cases
($p_0 = 0.1$ MPa and $\tau_p = 10\,\text{ms}$).

Figure 45 shows the effect of the magnitude of the external magnetic induction, B_y^*, on the plate's deflection. In this figure, the current density of the pulsed current is fixed at $J_0 = 10^5$ A/m^2 for all the cases. It can be seen that the results exactly follow the same trend reported for the 1D case; i.e., an increase in the magnitude of the magnetic field leads to a decrease in the amplitude of the deflection and a more rapid decay in vibrations.

In Fig. 46, same cases are shown while the pulsed current density is increased to $J_0 = 10^6$ A/m^2. The larger current density results in a larger suppression of the mechanical load, however, the amplitude of the post-impact vibrations gets larger. This is related to the fact that the pulsed current is still present in the plate after the impact load is disappeared (see Fig. 23) and it can dominate the vibrations if it is large enough.
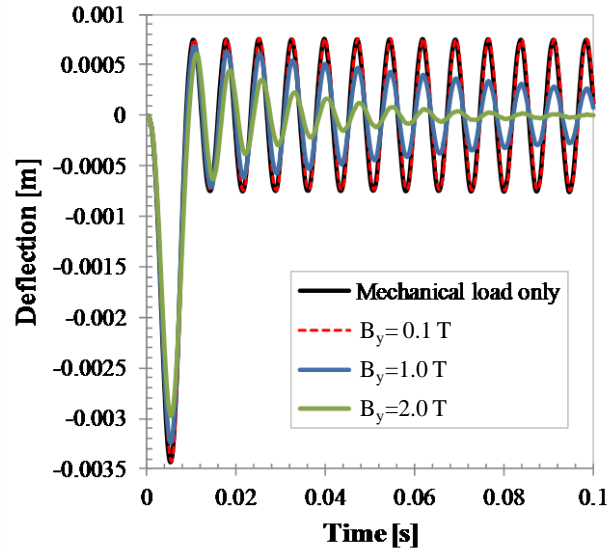
Figure 45. Plate's deflection over time: effect of the magnitude of the magnetic induction when $J_0 = 10^5$ A/m^2.
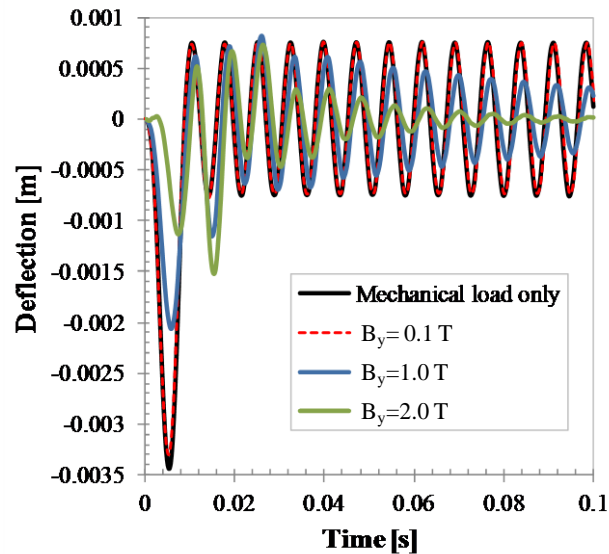
Figure 46. Plate's deflection over time: effect of the magnitude of the magnetic induction when $J_0 = 10^6$ A/m^2.

Another important conclusion that follows from the results presented in Fig. 46 is that the presence of the electromagnetic field may cause dispersion in the plate vibrations. The amount of dispersion depends on the magnitude of both the electric current density and magnetic induction. It is worth to mention again that, if both the current density and magnetic induction are small, the vibrations of the plate would not be affected much compared to the case when only the mechanical load is applied. This is also can be seen in Figs. 45 and 46.

The effect of the magnitude of the electric current density is presented in Fig. 47. Here, the magnetic induction is $B_y^* = 0.1\text{T}$ for all the cases. Similar to the 1D case, since the magnetic field is small, noticeable change in the vibration amplitudes is seen only when the current density is large enough, here as large as $J_0 = 10^7$ A/m^2. Furthermore, damping effect is ignorable when the magnetic field is small.
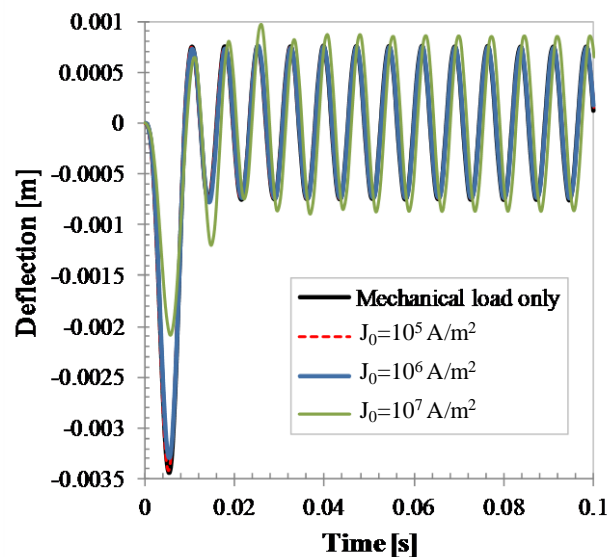
Figure 47. Plate's deflection over time: effect of the magnitude of the current density when $B_y^* = 0.1\text{T}$ (three curves coincide).

The mechanical response of the finite plate in the presence of a larger magnetic induction $B_y^* = 1.0\,\text{T}$ is shown in Fig. 48. Now that the magnetic field is relatively large, not only the damping effect is noticeable, but also the deflection of the plate is considerably reduced at least during the application of the impact load.
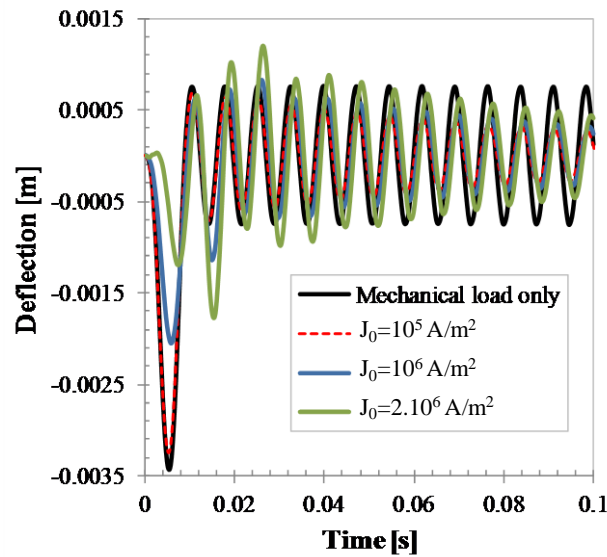
Figure 48. Plate's deflection over time: effect of the magnitude of the current density when $B_y^* = 1.0\,\text{T}$.

In Fig. 48, the current density is reduced to $J_0 = 2.10^6$ A/m^2 for the last case since for larger current densities, the electromagnetic load has an adverse effect and will destructively increase the vibrations.

Overall, the present study shows that due to complex interaction of mechanical and electromagnetic loads, the choice of the electromagnetic load, which will lead to reduction in the composite plate's deflection, and, therefore, stress mitigation in the plate,

depends on the profile of both mechanical and electromagnetic loads and is limited by the thermal considerations. As for the impact loads, the pulsed electric current combined with high in-plane magnetic field applied transversely to the direction of the current seems to be the best choice to mitigate the adverse effects of the impact load on the structure.

CHAPTER 6

TWO-DIMENSIONAL FINITE LAMINATED PLATE

6.1 Introduction

Studying a coupling problem is much more difficult in the case of anisotropic laminated plates since the mechanics of a multilayered composite is more complicated. Most studies in this regard have been devoted to the simulation of the response of piezoelectric and piezomagnetic laminates [140-144], while only few papers can be found on the fully magneto-electro-thermo-mechanical coupling in laminated materials.

Hasanyan et al. [99] and Qin et al. [100] formulated the electro-magneto-thermo-elastic coupling in a current-carrying symmetric orthotropic laminated composite plate subjected to thermal and magnetic fields. They assumed no electro-magneto-mechanical coupling in the formulation of the Lorentz force and only the geometrical nonlinearities were retained. Extended Hamilton's principle was employed to derive the governing equations from Maxwell's equations, equations of motion and Fourier's law of heat conduciton. For 2D approximation of the mechanical part, they adopted the first-order transversely shearable plate theory together with von Kármán's geometrically nonlinear strain. As for the 2D approximation of the Maxwell's equations of electrodynamics, Ambartsumyan's hypothesis was used. This was followed by the small disturbance concept to obtain a linear system of governing equations. Moreover, the electromagnetic field inside the laminate was determined by integration of the Maxwell's equations across the thickness of each layer. Finally, a linear thermal field was assumed. After developing the mathematical framework of the problem, Hasanyan et al. investigated the magneto-

thermo-mechanical behavior of a laminated plate strip in transversal and axial magnetic fields. They also studied the magneto-elastic wave propagation in an infinite plate.

In this section, the electro-magneto-mechanical coupling in a general laminated composite plate is formulated based on the mechanical and electromagnetic governing equations. The resulting system of equations together with the boundary conditions is solved numerically and the results are discussed.

<center>

6.2 Governing Mechanical Equations for the Laminated Plate

</center>

Consider an electrically conductive fiber reinforced laminated plate with the thickness H that consists of N_L number of unidirectional layers of thickness h. The laminate coordinate system (x, y, z) (i.e. the global coordinate system) is chosen in such a way that plane $x - y$ coincides with the middle plane and axis z is perpendicular to the middle plane (Figure 49). The orientation of the fibers may be different in each lamina layer.
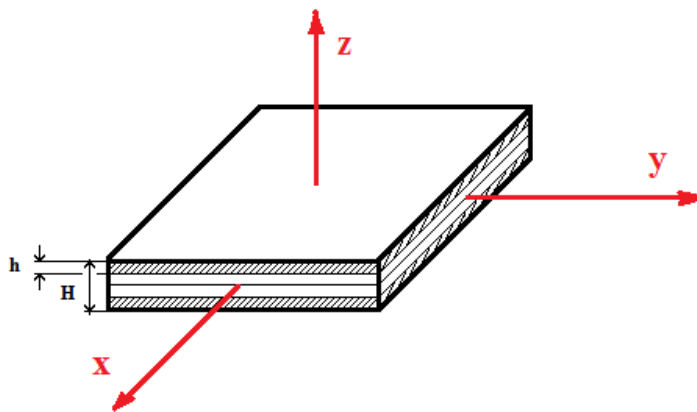
Figure 49. Laminated composite plate with the laminate coordinate axes.

Assume that each lamina in the laminate is transversely isotropic. Therefore, the stress-strain relations in the principal material directions (i.e. directions that are parallel to the planes of the material symmetry) for i-th lamina are

$$
\begin{bmatrix} \tau_{11} \\ \tau_{22} \\ \tau_{33} \\ \tau_{23} \\ \tau_{13} \\ \tau_{12} \end{bmatrix}_i = \begin{bmatrix} C_{11} & C_{12} & C_{12} & 0 & 0 & 0 \\ C_{12} & C_{22} & C_{23} & 0 & 0 & 0 \\ C_{12} & C_{23} & C_{22} & 0 & 0 & 0 \\ 0 & 0 & 0 & C_{44} & 0 & 0 \\ 0 & 0 & 0 & 0 & C_{55} & 0 \\ 0 & 0 & 0 & 0 & 0 & C_{55} \end{bmatrix} \begin{bmatrix} e_1 \\ e_2 \\ e_3 \\ \gamma_{23} \\ \gamma_{13} \\ \gamma_{12} \end{bmatrix}_i , \qquad (6\text{-}1)
$$

where C_{ij} are the components of the stiffness matrix $\mathbf{C}$ which are defined in terms of the material properties as follows:

$$
\begin{aligned}
C_{11} &= \frac{(1-v_{23}^2)E_1}{1-v}, \qquad C_{12} = \frac{(v_{12}+v_{23}v_{12})E_2}{1-v}, \qquad C_{23} = \frac{(v_{23}+v_{21}v_{12})E_2}{1-v}, \\
C_{22} &= \frac{(1-v_{12}v_{21})E_1}{1-v}, \qquad C_{44} = G_{23}, \qquad C_{55} = G_{12},
\end{aligned} \qquad (6\text{-}2)
$$

where

$$
v = v_{12}v_{21} + v_{23}v_{32} + v_{31}v_{13} + 2v_{21}v_{32}v_{13}. \qquad (6\text{-}3)
$$

Here E_1 is Young's modulus for the fiber direction, E_2 is Young's modulus for the isotropy plane, v_{23} is Poisson's ratio characterizing the contraction within the plane of isotropy for forces applied within the same plane, v_{12} is Poisson's ratio characterizing contraction in the plane of isotropy due to forces in the direction perpendicular to it, and v_{21} is Poisson's ratio characterizing contraction in the direction perpendicular to the plane of isotropy due to forces within the plane of isotropy, G_{12} is the shear modulus for the direction perpendicular to the plane of isotropy, G_{23} is the shear modulus in the plane of isotropy ($2-3$).

In the laminate coordinate system (x, y, z), the stress-strain relations for i-th lamina can be written in the form:

$$\begin{bmatrix} \tau_{xx} \\ \tau_{yy} \\ \tau_{zz} \\ \tau_{yz} \\ \tau_{xz} \\ \tau_{xy} \end{bmatrix}_i = \begin{bmatrix} \bar{C}_{11} & \bar{C}_{12} & \bar{C}_{13} & 0 & 0 & \bar{C}_{16} \\ \bar{C}_{12} & \bar{C}_{22} & \bar{C}_{23} & 0 & 0 & \bar{C}_{26} \\ \bar{C}_{13} & \bar{C}_{23} & \bar{C}_{33} & 0 & 0 & \bar{C}_{36} \\ 0 & 0 & 0 & \bar{C}_{44} & \bar{C}_{45} & 0 \\ 0 & 0 & 0 & \bar{C}_{45} & \bar{C}_{55} & 0 \\ \bar{C}_{16} & \bar{C}_{26} & \bar{C}_{36} & 0 & 0 & \bar{C}_{66} \end{bmatrix} \begin{bmatrix} e_x \\ e_y \\ e_z \\ \gamma_{yz} \\ \gamma_{xz} \\ \gamma_{xy} \end{bmatrix}_i . \tag{6-4}$$

Here $\bar{C}_{ij}$ are the components of the transformed stiffness matrix $\bar{\mathbf{C}}$ defined as:

$$\bar{\mathbf{C}} = \mathbf{T^{-1}CT^{-T}}, \tag{6-5}$$

where $\mathbf{T}$ is transformation matrix, the superscript -1 denotes the matrix inverse and the superscript $\mathbf{T}$ denotes the matrix transpose.
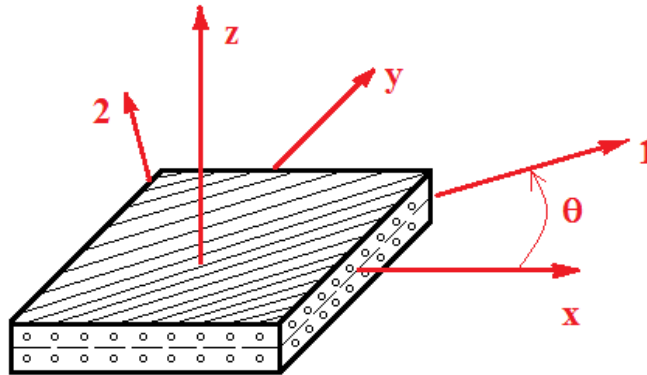
Figure 50. Laminate coordinate system (x, y, z) and in-plane principal material directions $(1, 2)$

The transformation matrix **T** is defined as

$$\mathbf{T} = \begin{bmatrix} \cos^2\theta & \sin^2\theta & 0 & 0 & 0 & 2\cos\theta\sin\theta \\ \sin^2\theta & \cos^2\theta & 0 & 0 & 0 & -2\cos\theta\sin\theta \\ 0 & 0 & 1 & 0 & 0 & 0 \\ 0 & 0 & 0 & \cos\theta & -\sin\theta & 0 \\ 0 & 0 & 0 & \sin\theta & \cos\theta & 0 \\ -\cos\theta\sin\theta & \cos\theta\sin\theta & 0 & 0 & 0 & \cos^2\theta - \sin^2\theta \end{bmatrix}, \tag{6-6}$$

where θ is the angle from the *x*-axis to the 1-axis as shown in Figure 50. It is also assumed that all laminae in the laminate are perfectly bonded, the laminate is thin and a normal to the middle plane is assumed to remain straight and perpendicular to the middle plane when the laminate is deformed. This allows us to employ the classic Kirchhoff hypothesis of nondeformable normals to write laminate displacements in the form (3-10) and laminate strains as:

$$e_x = \frac{\partial u}{\partial x} - z\frac{\partial^2 w}{\partial x^2}, \qquad e_y = \frac{\partial v}{\partial y} - z\frac{\partial^2 w}{\partial y^2}, \qquad e_z = \frac{\partial w}{\partial z} = 0,$$

$$\gamma_{xy} = \frac{\partial u}{\partial y} + \frac{\partial v}{\partial x} - 2z\frac{\partial^2 w}{\partial x\partial y}, \qquad \gamma_{yz} = \gamma_{xz} = 0, \tag{6-7}$$

or

$$\begin{bmatrix} e_x \\ e_y \\ \gamma_{xy} \end{bmatrix} = \begin{bmatrix} e_x^o \\ e_y^o \\ \gamma_{xy}^o \end{bmatrix} + z\begin{bmatrix} \kappa_x \\ \kappa_y \\ \kappa_{xy} \end{bmatrix}, \tag{6-8}$$

where $u(x,y,t),\ v(x,y,t),\ w(x,y,t)$ are the corresponding middle plane displacement components, $e_x^o,\ e_y^o,\ \gamma_{xy}^o$ are the middle plane strains:

$$\begin{bmatrix} e_x^o \\ e_y^o \\ \gamma_{xy}^o \end{bmatrix} = \begin{bmatrix} \dfrac{\partial u}{\partial x} \\ \dfrac{\partial v}{\partial y} \\ \dfrac{\partial u}{\partial y} + \dfrac{\partial v}{\partial x} \end{bmatrix}, \tag{6-9}$$

and κ_x, κ_y, κ_{xy} are middle plane curvatures:

$$\begin{bmatrix} \kappa_x \\ \kappa_y \\ \kappa_{xy} \end{bmatrix} = - \begin{bmatrix} \dfrac{\partial^2 w}{\partial x^2} \\ \dfrac{\partial^2 w}{\partial y^2} \\ 2\dfrac{\partial^2 w}{\partial x \partial y} \end{bmatrix}. \tag{6-10}$$

The Kirchhoff hypothesis implies a linear variation of strain through the laminate thickness, whereas the stress variation through the thickness of the laminate is piecewise linear. In other words, the stress variation is linear through each lamina layer, but discontinues at lamina boundaries. Note that although shear strains are assumed to be zero, yet transverse shear stresses are not regarded as zeros but calculated from the equations of motion or equilibrium.

The stress and moment resultants are obtained by integration of the stresses through the thickness of the laminate:

$$\begin{bmatrix} N_{xx} \\ N_{yy} \\ N_{yz} \\ N_{xz} \\ N_{xy} \end{bmatrix} = \int_{-H/2}^{H/2} \begin{bmatrix} \tau_{xx} \\ \tau_{yy} \\ \tau_{yz} \\ \tau_{xz} \\ \tau_{xy} \end{bmatrix} dz = \sum_{i=1}^{N_L+1} \int_{z_i}^{z_{i+1}} \begin{bmatrix} \tau_{xx} \\ \tau_{yy} \\ \tau_{yz} \\ \tau_{xz} \\ \tau_{xy} \end{bmatrix}_i dz, \tag{6-11}$$

$$\begin{bmatrix} M_{xx} \\ M_{yy} \\ M_{xy} \end{bmatrix} = \int_{-H/2}^{H/2} \begin{bmatrix} \tau_{xx} \\ \tau_{yy} \\ \tau_{xy} \end{bmatrix} z dz = \sum_{i=1}^{N_L+1} \int_{z_i}^{z_{i+1}} \begin{bmatrix} \tau_{xx} \\ \tau_{yy} \\ \tau_{xy} \end{bmatrix}_i z dz, \tag{6-12}$$

where z_{i+1} is the distance to the top of the i-th layer in the laminate and z_i is the distance to the bottom of the i-th layer as shown in Figure 51.
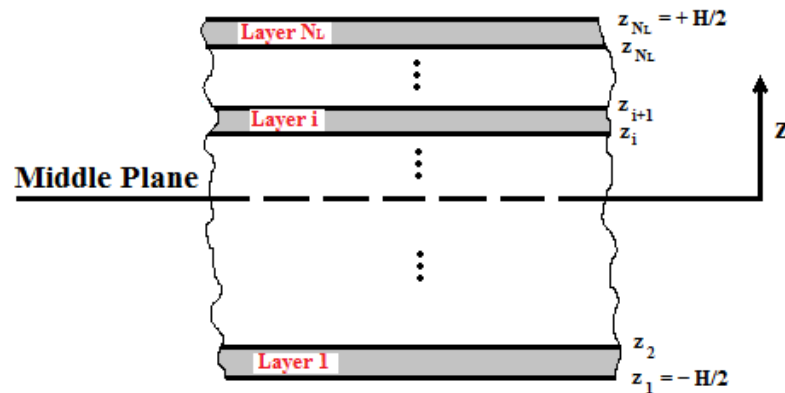
Figure 51. Coordinates of each layer in the laminate with N_L layers

Using stress-strain relations (6-1) and strain middle plane displacement relations(6-7), the stress and moment resultants can be rewritten with respect to the derivatives of the middle plane displacements:

$$N_{xx} = \int_{-H/2}^{H/2} \tau_{xx} dz = \mathsf{M}_1[\bar{C}_{11}]\frac{\partial u}{\partial x} + \mathsf{M}_1[\bar{C}_{12}]\frac{\partial v}{\partial y} + \mathsf{M}_1[\bar{C}_{16}]\left(\frac{\partial u}{\partial y} + \frac{\partial v}{\partial x}\right)$$
$$- \mathsf{M}_2[\bar{C}_{11}]\frac{\partial^2 w}{\partial^2 x} - \mathsf{M}_2[\bar{C}_{12}]\frac{\partial^2 w}{\partial^2 y} - 2\mathsf{M}_2[\bar{C}_{16}]\frac{\partial^2 w}{\partial x \partial y},$$

$$N_{yy} = \int_{-H/2}^{H/2} \tau_{yy} dz = \mathsf{M}_1[\bar{C}_{12}]\frac{\partial u}{\partial x} + \mathsf{M}_1[\bar{C}_{22}]\frac{\partial v}{\partial y} + \mathsf{M}_1[\bar{C}_{26}]\left(\frac{\partial u}{\partial y} + \frac{\partial v}{\partial x}\right)$$
$$- \mathsf{M}_2[\bar{C}_{12}]\frac{\partial^2 w}{\partial^2 x} - \mathsf{M}_2[\bar{C}_{22}]\frac{\partial^2 w}{\partial^2 y} - 2\mathsf{M}_2[\bar{C}_{26}]\frac{\partial^2 w}{\partial x \partial y},$$

$$N_{xy} = \int_{-H/2}^{H/2} \tau_{xy} dz = \mathsf{M}_1[\bar{C}_{16}]\frac{\partial u}{\partial x} + \mathsf{M}_1[\bar{C}_{26}]\frac{\partial v}{\partial y} + \mathsf{M}_1[\bar{C}_{66}]\left(\frac{\partial u}{\partial y} + \frac{\partial v}{\partial x}\right)$$
$$- \mathsf{M}_2[\bar{C}_{16}]\frac{\partial^2 w}{\partial^2 x} - \mathsf{M}_2[\bar{C}_{26}]\frac{\partial^2 w}{\partial^2 y} - 2\mathsf{M}_2[\bar{C}_{66}]\frac{\partial^2 w}{\partial x \partial y},$$

$$N_{xz} = \int_{-H/2}^{H/2} \tau_{xz} dz,$$

$$N_{yz} = \int_{-H/2}^{H/2} \tau_{yz} dz,$$

(6-13)

$$M_{xx} = \int_{-H/2}^{H/2} \tau_{xx} z dz = \mathsf{M}_2[\bar{C}_{11}]\frac{\partial u}{\partial x} + \mathsf{M}_2[\bar{C}_{12}]\frac{\partial v}{\partial y} + \mathsf{M}_2[\bar{C}_{16}]\left(\frac{\partial u}{\partial y} + \frac{\partial v}{\partial x}\right)$$
$$- \mathsf{M}_3[\bar{C}_{11}]\frac{\partial^2 w}{\partial^2 x} - \mathsf{M}_3[\bar{C}_{12}]\frac{\partial^2 w}{\partial^2 y} - 2\mathsf{M}_3[\bar{C}_{16}]\frac{\partial^2 w}{\partial x \partial y},$$

$$M_{yy} = \int_{-H/2}^{H/2} \tau_{xy} z dz = \mathsf{M}_2[\bar{C}_{12}]\frac{\partial u}{\partial x} + \mathsf{M}_2[\bar{C}_{22}]\frac{\partial v}{\partial y} + \mathsf{M}_2[\bar{C}_{26}]\left(\frac{\partial u}{\partial y} + \frac{\partial v}{\partial x}\right)$$
$$- \mathsf{M}_3[\bar{C}_{12}]\frac{\partial^2 w}{\partial^2 x} - \mathsf{M}_3[\bar{C}_{22}]\frac{\partial^2 w}{\partial^2 y} - 2\mathsf{M}_3[\bar{C}_{26}]\frac{\partial^2 w}{\partial x \partial y},$$

$$M_{xy} = \int_{-H/2}^{H/2} \tau_{xy} z dz = \mathsf{M}_2[\bar{C}_{16}]\frac{\partial u}{\partial x} + \mathsf{M}_2[\bar{C}_{26}]\frac{\partial v}{\partial y} + \mathsf{M}_2[\bar{C}_{66}]\left(\frac{\partial u}{\partial y} + \frac{\partial v}{\partial x}\right)$$
$$- \mathsf{M}_3[\bar{C}_{16}]\frac{\partial^2 w}{\partial^2 x} - \mathsf{M}_3[\bar{C}_{26}]\frac{\partial^2 w}{\partial^2 y} - 2\mathsf{M}_3[\bar{C}_{66}]\frac{\partial^2 w}{\partial x \partial y},$$

where the operator M is defined as

$$\mathsf{M}_k[f] = \int_{-H/2}^{H/2} f\, z^{k-1} dz = \frac{1}{k}\sum_{i=1}^{N_L} f^{(i)}(z_{i+1}^k - z_i^k),$$

(6-14)

It should be noted that in Eq. (6-13), N_{xz} and N_{yz} cannot be computed in the same manner that the other resultants are found since they are neglected in the Kirchhoff hypothesis. Therefore, other methods should be employed to calculate them in this case.

The in-plane stress and moment resultants can be also rewritten in terms of the middle plane strains and curvatures as

$$
\begin{bmatrix} N_{xx} \\ N_{yy} \\ N_{xy} \end{bmatrix} = \begin{bmatrix} A_{11} & A_{12} & A_{16} \\ A_{12} & A_{22} & A_{26} \\ A_{16} & A_{26} & A_{66} \end{bmatrix} \begin{bmatrix} e_x^o \\ e_y^o \\ \gamma_{xy}^o \end{bmatrix} + \begin{bmatrix} B_{11} & B_{12} & B_{16} \\ B_{12} & B_{22} & B_{26} \\ B_{16} & B_{26} & B_{66} \end{bmatrix} \begin{bmatrix} \kappa_x \\ \kappa_y \\ \kappa_{xy} \end{bmatrix}, \tag{6-15}
$$

$$
\begin{bmatrix} M_{xx} \\ M_{yy} \\ M_{xy} \end{bmatrix} = \begin{bmatrix} B_{11} & B_{12} & B_{16} \\ B_{12} & B_{22} & B_{26} \\ B_{16} & B_{26} & B_{66} \end{bmatrix} \begin{bmatrix} e_x^o \\ e_y^o \\ \gamma_{xy}^o \end{bmatrix} + \begin{bmatrix} D_{11} & D_{12} & D_{16} \\ D_{12} & D_{22} & D_{26} \\ D_{16} & D_{26} & D_{66} \end{bmatrix} \begin{bmatrix} \kappa_x \\ \kappa_y \\ \kappa_{xy} \end{bmatrix}, \tag{6-16}
$$

where

$$
\begin{aligned}
A_{ij} &= \sum_{i=1}^{N_L+1} \left(\overline{Q}_{ij} \right)_i \left(z_{i+1} - z_i \right) = \mathsf{M}_1[\overline{Q}_{ij}], \\
B_{ij} &= \frac{1}{2} \sum_{i=1}^{N_L+1} \left(\overline{Q}_{ij} \right)_i \left(z_{i+1}^2 - z_i^2 \right) = \mathsf{M}_2[\overline{Q}_{ij}], \\
D_{ij} &= \frac{1}{3} \sum_{i=1}^{N_L+1} \left(\overline{Q}_{ij} \right)_i \left(z_{i+1}^3 - z_i^3 \right) = \mathsf{M}_3[\overline{Q}_{ij}].
\end{aligned} \tag{6-17}
$$

Here A_{ij} are the components of the so-called extensional stiffnesses, B_{ij} are bending-extension coupling stiffnesses, and the D_{ij} are bending stiffnesses [145] and $\overline{Q}_{ij}$ are the components of the reduced stiffness matrix $\overline{\mathbf{Q}}$:

$$
\overline{\mathbf{Q}} = \begin{bmatrix} \overline{Q}_{11} & \overline{Q}_{12} & \overline{Q}_{16} \\ \overline{Q}_{12} & \overline{Q}_{22} & \overline{Q}_{26} \\ \overline{Q}_{16} & \overline{Q}_{26} & \overline{Q}_{66} \end{bmatrix} = \begin{bmatrix} \overline{C}_{11} & \overline{C}_{12} & \overline{C}_{16} \\ \overline{C}_{12} & \overline{C}_{22} & \overline{C}_{26} \\ \overline{C}_{16} & \overline{C}_{26} & \overline{C}_{66} \end{bmatrix}, \tag{6-18}
$$

in which

$$\overline{Q}_{11} = \overline{C}_{11} = C_{11}\cos^4\theta + 2(C_{12} + 2C_{66})\sin^2\theta\cos^2\theta + C_{22}\sin^4\theta,$$
$$\overline{Q}_{12} = \overline{C}_{12} = (C_{11} + C_{22} - 4C_{66})\sin^2\theta\cos^2\theta + C_{12}(\cos^4\theta + \sin^4\theta),$$
$$\overline{Q}_{22} = \overline{C}_{22} = C_{11}\sin^4\theta + 2(C_{12} + 2C_{66})\sin^2\theta\cos^2\theta + C_{22}\cos^4\theta,$$
$$\overline{Q}_{16} = \overline{C}_{16} = (C_{11} - C_{12} - 2C_{66})\sin\theta\cos^3\theta + (C_{12} - C_{22} + 2C_{66})\sin^3\theta\cos\theta, \qquad (6\text{-}19)$$
$$\overline{Q}_{26} = \overline{C}_{26} = (C_{11} - C_{12} - 2C_{66})\sin^3\theta\cos\theta + (C_{12} - C_{22} + 2C_{66})\sin\theta\cos^3\theta,$$
$$\overline{Q}_{66} = \overline{C}_{66} = (C_{11} + C_{22} - 2C_{12} - 2C_{66})\sin^2\theta\cos^2\theta + C_{66}(\cos^4\theta + \sin^4\theta),$$

where θ is the angle between the *x*-axis and the 1-axis.

Therefore, the stress and moment resultants can be written in terms of extensional, bending-extension coupling, and bending stiffnesses as

$$N_{xx} = A_{11}\frac{\partial u}{\partial x} + A_{12}\frac{\partial v}{\partial y} + A_{16}\left(\frac{\partial u}{\partial y} + \frac{\partial v}{\partial x}\right) - B_{11}\frac{\partial^2 w}{\partial^2 x} - B_{12}\frac{\partial^2 w}{\partial^2 y} - 2B_{16}\frac{\partial^2 w}{\partial x\partial y},$$
$$N_{yy} = A_{12}\frac{\partial u}{\partial x} + A_{22}\frac{\partial v}{\partial y} + A_{26}\left(\frac{\partial u}{\partial y} + \frac{\partial v}{\partial x}\right) - B_{12}\frac{\partial^2 w}{\partial^2 x} - B_{22}\frac{\partial^2 w}{\partial^2 y} - 2B_{26}\frac{\partial^2 w}{\partial x\partial y},$$
$$N_{xy} = A_{16}\frac{\partial u}{\partial x} + A_{26}\frac{\partial v}{\partial y} + A_{26}\left(\frac{\partial u}{\partial y} + \frac{\partial v}{\partial x}\right) - B_{16}\frac{\partial^2 w}{\partial^2 x} - B_{26}\frac{\partial^2 w}{\partial^2 y} - 2B_{66}\frac{\partial^2 w}{\partial x\partial y},$$
$$N_{xz} = \int_{-H/2}^{H/2}\tau_{xz}dz,$$
$$N_{yz} = \int_{-H/2}^{H/2}\tau_{yz}dz, \qquad (6\text{-}20)$$
$$M_{xx} = B_{11}\frac{\partial u}{\partial x} + B_{12}\frac{\partial v}{\partial y} + B_{16}\left(\frac{\partial u}{\partial y} + \frac{\partial v}{\partial x}\right) - D_{11}\frac{\partial^2 w}{\partial^2 x} - D_{12}\frac{\partial^2 w}{\partial^2 y} - 2D_{16}\frac{\partial^2 w}{\partial x\partial y},$$
$$M_{yy} = B_{12}\frac{\partial u}{\partial x} + B_{22}\frac{\partial v}{\partial y} + B_{26}\left(\frac{\partial u}{\partial y} + \frac{\partial v}{\partial x}\right) - D_{12}\frac{\partial^2 w}{\partial^2 x} - D_{22}\frac{\partial^2 w}{\partial^2 y} - 2D_{26}\frac{\partial^2 w}{\partial x\partial y},$$
$$M_{xy} = B_{16}\frac{\partial u}{\partial x} + B_{26}\frac{\partial v}{\partial y} + B_{66}\left(\frac{\partial u}{\partial y} + \frac{\partial v}{\partial x}\right) - D_{16}\frac{\partial^2 w}{\partial^2 x} - D_{26}\frac{\partial^2 w}{\partial^2 y} - 2D_{66}\frac{\partial^2 w}{\partial x\partial y},$$

Two-dimensional equations of motion for laminated plates are obtained by integration of equations of motion across the thickness of the plate $(-H/2, H/2)$. In the presence of the electromagnetic loads and surface mechanical loads this procedure yields

$$\frac{\partial N_{xx}}{\partial x} + \frac{\partial N_{xy}}{\partial y} + X_2 + \rho \int\limits_{-\frac{H}{2}}^{\frac{H}{2}} F_x^L dz = \rho H \frac{\partial^2 u}{\partial t^2},$$

$$\frac{\partial N_{yy}}{\partial y} + \frac{\partial N_{xy}}{\partial x} + Y_2 + \rho \int\limits_{-\frac{H}{2}}^{\frac{H}{2}} F_y^L dz = \rho H \frac{\partial^2 v}{\partial t^2},$$

$$\frac{\partial N_{xz}}{\partial x} + \frac{\partial N_{yz}}{\partial y} + Z_2 + \rho \int\limits_{-\frac{H}{2}}^{\frac{H}{2}} F_z^L dz = \rho H \frac{\partial^2 w}{\partial t^2}, \qquad (6\text{-}21)$$

$$\frac{\partial M_{xx}}{\partial x} + \frac{\partial M_{xy}}{\partial y} + H X_1 + \rho \int\limits_{-\frac{H}{2}}^{\frac{H}{2}} F_x^L z dz = N_{xz} - \rho \frac{H^3}{12} \frac{\partial^3 w}{\partial t^2 \partial x},$$

$$\frac{\partial M_{yy}}{\partial y} + \frac{\partial M_{xy}}{\partial x} + H Y_1 + \rho \int\limits_{-\frac{H}{2}}^{\frac{H}{2}} F_y^L z dz = N_{yz} - \rho \frac{H^3}{12} \frac{\partial^3 w}{\partial t^2 \partial y}.$$

Here ρ is the material density of the laminate, t is time, $\mathbf{F}^L = \left(F_x^L, F_y^L, F_z^L \right)$ is the Lorentz ponderomotive force per unit mass vector, and X_k, Y_k, and Z_k are combinations of tractions at the external surfaces of the laminate

$$X_1 = \frac{1}{2}\left(\tau_{xz}\bigg|_{z=\frac{H}{2}} + \tau_{xz}\bigg|_{z=-\frac{H}{2}} \right), \quad X_2 = \tau_{xz}\bigg|_{z=\frac{H}{2}} - \tau_{xz}\bigg|_{z=-\frac{H}{2}},$$

$$Y_1 = \frac{1}{2}\left(\tau_{yz}\bigg|_{z=\frac{H}{2}} + \tau_{yz}\bigg|_{z=-\frac{H}{2}} \right), \quad Y_2 = \tau_{yz}\bigg|_{z=\frac{H}{2}} - \tau_{yz}\bigg|_{z=-\frac{H}{2}}, \qquad (6\text{-}22)$$

$$Z_2 = \tau_{zz}\bigg|_{z=\frac{H}{2}} - \tau_{zz}\bigg|_{z=-\frac{H}{2}}.$$

Thus, the equations of motion are solved with respect to the middle plane displacements $u(x,y,t)$, $v(x,y,t)$, $w(x,y,t)$. After that the in-plane stresses τ_{xx}, τ_{yy}, τ_{xy} are found using stress-strain relations (6-4), and transverse shear stresses τ_{xz} and τ_{yz} and normal stress τ_{zz} are found by integrating equations of motion

$$\frac{\partial \tau_{xx}}{\partial x} + \frac{\partial \tau_{xy}}{\partial y} + \frac{\partial \tau_{xz}}{\partial z} + \rho \int\limits_{-\frac{H}{2}}^{\frac{H}{2}} F_x^L dz = \rho \frac{\partial^2 u_x}{\partial t^2},$$

$$\frac{\partial \tau_{xy}}{\partial x} + \frac{\partial \tau_{yy}}{\partial y} + \frac{\partial \tau_{yz}}{\partial z} + \rho \int\limits_{-\frac{H}{2}}^{\frac{H}{2}} F_y^L dz = \rho \frac{\partial^2 u_y}{\partial t^2}, \qquad (6\text{-}23)$$

$$\frac{\partial \tau_{xy}}{\partial x} + \frac{\partial \tau_{yz}}{\partial y} + \frac{\partial \tau_{zz}}{\partial z} + \rho \int\limits_{-\frac{H}{2}}^{\frac{H}{2}} F_z^L dz = \rho \frac{\partial^2 u_z}{\partial t^2}.$$

Furthermore, in the classical theory the effect of transverse normal stress τ_{zz} on the stresses and deformed state of the laminate is disregarded because this stress is considered to be small in comparison to in-plane stresses.

6.3 Governing Electromagnetic Equations for the Laminated Plate

Since generally the fibers in a lamina may not be in the direction of the global axes, the conductivity of layer i of a laminate in the laminate coordinate system (x, y, z) is defined as:

$$\boldsymbol{\sigma}^{(i)} = \begin{bmatrix} \sigma_{11}^{(i)} & \sigma_{12}^{(i)} & 0 \\ \sigma_{12}^{(i)} & \sigma_{22}^{(i)} & 0 \\ 0 & 0 & \sigma_{33}^{(i)} \end{bmatrix}, \qquad (6\text{-}24)$$

where

$$\sigma_{11}^{(i)} = \sigma_1^{(i)} \cos^2 \theta + \sigma_2^{(i)} \sin^2 \theta,$$
$$\sigma_{22}^{(i)} = \sigma_2^{(i)} \cos^2 \theta + \sigma_1^{(i)} \sin^2 \theta,$$
$$\sigma_{12}^{(i)} = (\sigma_1^{(i)} - \sigma_2^{(i)}) \sin \theta \cos \theta, \qquad (6\text{-}25)$$
$$\sigma_{33}^{(i)} = \sigma_3^{(i)}.$$

Here $\sigma_1^{(i)}$, $\sigma_2^{(i)}$ and $\sigma_3^{(i)}$ are the conductivities along the principal material directions of the lamina i (see Figure 50).

To obtain electromagnetic equations for the laminated plates, the electromagnetic hypotheses (3-20), which imply no variation in tangential components of the electric field vector and the normal component of the magnetic field across the thickness of the plate, are applied first. This transforms Maxwells' equations (3-1) to the form

$$-\frac{\partial B_x}{\partial t} = \frac{\partial E_z}{\partial y} - \frac{\partial E_y}{\partial z}, \qquad -\frac{\partial B_y}{\partial t} = \frac{\partial E_x}{\partial z} - \frac{\partial E_z}{\partial x}, \qquad -\frac{\partial B_z}{\partial t} = \frac{\partial E_y}{\partial x} - \frac{\partial E_x}{\partial y}, \qquad (6\text{-}26)$$

$$J_x = \frac{\partial H_z}{\partial y} - \frac{\partial H_y}{\partial z}, \qquad J_y = \frac{\partial H_x}{\partial z} - \frac{\partial H_z}{\partial x}, \qquad J_z = \frac{\partial H_y}{\partial x} - \frac{\partial H_x}{\partial y}, \qquad (6\text{-}27)$$

where the components of the induced current density in the layer i are determined as

$$J_x^{(i)} = \sigma_{11}^{(i)}(E_x + \frac{\partial u_y}{\partial t} B_z - \frac{\partial u_z}{\partial t} B_y^{(i)}) + \sigma_{12}^{(i)}(E_y + \frac{\partial u_z}{\partial t} B_x^{(i)} - \frac{\partial u_x}{\partial t} B_z),$$
$$J_y^{(i)} = \sigma_{12}^{(i)}(E_x + \frac{\partial u_y}{\partial t} B_z - \frac{\partial u_z}{\partial t} B_y^{(i)}) + \sigma_{22}^{(i)}(E_y + \frac{\partial u_z}{\partial t} B_x^{(i)} - \frac{\partial u_x}{\partial t} B_z), \qquad (6\text{-}28)$$
$$J_z^{(i)} = \sigma_{33}^{(i)}(E_z + \frac{\partial u_x}{\partial t} B_y^{(i)} - \frac{\partial u_y}{\partial t} B_x^{(i)}).$$

Relationships (6-25) are obtained by substitution equations (6-23) into the third equation of (3-3).

Linear approximation for tangential components of the magnetic field (3-32) is hold for each layer of the laminated plate and, therefore, in-plane components of magnetic induction can be written in each layer as:

$$B_x^{(i)} = \frac{1}{2}\left(B_x^{(i)+} + B_x^{(i)-}\right) + \frac{z}{h}\left(B_x^{(i)+} - B_x^{(i)-}\right) = \frac{1}{2}B_{x1}^{(i)} + \frac{z}{h}B_{x2}^{(i)},$$

$$B_y^{(i)} = \frac{1}{2}\left(B_y^{(i)+} + B_y^{(i)-}\right) + \frac{z}{h}\left(B_y^{(i)+} - B_y^{(i)-}\right) = \frac{1}{2}B_{y1}^{(i)} + \frac{z}{h}B_{y2}^{(i)}.$$

(6-29)

Moreover, we assume that the distribution of the in-plane components of magnetic induction along the thickness of the laminate is linear and continuous so that the result of the integration of Eqs. (6-27) across the thickness of the plate depends only on the surface values of the induction on the top and bottom surfaces of the laminated plate.

By substituting Eq. (6-29) into (6-26), we have:

$$\sigma_{11}^{(i)}\left(E_x + \frac{\partial u_y}{\partial t}B_z - \frac{\partial u_z}{\partial t}B_y^{(i)}\right) + \sigma_{12}^{(i)}\left(E_y + \frac{\partial u_z}{\partial t}B_x^{(i)} - \frac{\partial u_x}{\partial t}B_z\right)$$
$$= \frac{\partial H_z}{\partial y} - \frac{1}{h}(H_y^{(i)+} - H_y^{(i)-}),$$

$$\sigma_{12}^{(i)}\left(E_x + \frac{\partial u_y}{\partial t}B_z - \frac{\partial u_z}{\partial t}B_y^{(i)}\right) + \sigma_{22}^{(i)}\left(E_y + \frac{\partial u_z}{\partial t}B_x^{(i)} - \frac{\partial u_x}{\partial t}B_z\right)$$
$$= -\frac{\partial H_z}{\partial x} + \frac{1}{h}(H_x^{(i)+} - H_x^{(i)-}).$$

(6-30)

Application of the Kirchhoff hypothesis (3-10) to the equations (6-30) and integration of the resulting equations across the thickness of the laminate, leads to the following electromagnetic governing equations in a laminate:

$$\mathsf{M}_1[\sigma_{11}]E_x + \mathsf{M}_1[\sigma_{11}]\frac{\partial v}{\partial t}B_z - \mathsf{M}_2[\sigma_{11}]\frac{\partial^2 w}{\partial y\partial t}B_z - \frac{1}{2}\mathsf{M}_1[\sigma_{11}]\frac{\partial w}{\partial t}B_{y1}$$

$$-\frac{1}{2}\mathsf{M}_2[\sigma_{11}]\frac{\partial w}{\partial t}B_{y2} + \mathsf{M}_1[\sigma_{12}]E_y + \frac{1}{2}\mathsf{M}_1[\sigma_{12}]\frac{\partial w}{\partial t}B_{x1} + \frac{1}{H}\mathsf{M}_2[\sigma_{12}]\frac{\partial w}{\partial t}B_{x2}$$

$$-\mathsf{M}_1[\sigma_{12}]\frac{\partial u}{\partial t}B_z + \mathsf{M}_2[\sigma_{12}]\frac{\partial^2 w}{\partial x\partial t}B_z = H\frac{\partial H_z}{\partial y} - (H_y^+ - H_y^-),$$

(6-31)

$$\mathsf{M}_1[\sigma_{12}]E_x + \mathsf{M}_1[\sigma_{12}]\frac{\partial v}{\partial t}B_z - \mathsf{M}_2[\sigma_{12}]\frac{\partial^2 w}{\partial y\partial t}B_z - \frac{1}{2}\mathsf{M}_1[\sigma_{12}]\frac{\partial w}{\partial t}B_{y1}$$

$$-\frac{1}{H}\mathsf{M}_2[\sigma_{12}]\frac{\partial w}{\partial t}B_{y2} + \mathsf{M}_1[\sigma_{22}]E_y + \frac{1}{2}\mathsf{M}_1[\sigma_{22}]\frac{\partial w}{\partial t}B_{x1} + \frac{1}{H}\mathsf{M}_2[\sigma_{22}]\frac{\partial w}{\partial t}B_{x2}$$

$$-\mathsf{M}_1[\sigma_{22}]\frac{\partial u}{\partial t}B_z + \mathsf{M}_2[\sigma_{22}]\frac{\partial^2 w}{\partial x\partial t}B_z = -H\frac{\partial H_z}{\partial x} + (H_x^+ - H_x^-).$$

It should be noted that the normal component of the magnetic induction vector (i.e. H_z) and tangential components of the electric field vector are continuous across the thickness of the laminate. This can be concluded from the electromagnetic boundary conditions (3-38) and (3-39).

From the second equation of (6-31), an expression for E_y can be derived:

$$E_y = -\frac{H}{\mu\mathsf{M}_1[\sigma_{22}]}\frac{\partial B_z}{\partial x} + \frac{1}{\mu\mathsf{M}_1[\sigma_{22}]}B_{x2} - \frac{\mathsf{M}_1[\sigma_{12}]}{\mathsf{M}_1[\sigma_{22}]}E_x - \frac{\mathsf{M}_1[\sigma_{12}]}{\mathsf{M}_1[\sigma_{22}]}\frac{\partial v}{\partial t}B_z$$

$$+\frac{\mathsf{M}_2[\sigma_{12}]}{\mathsf{M}_1[\sigma_{22}]}\frac{\partial W}{\partial t}B_z + \frac{1}{2}\frac{\mathsf{M}_1[\sigma_{12}]}{\mathsf{M}_1[\sigma_{22}]}\frac{\partial w}{\partial t}B_{y1} + \frac{1}{H}\frac{\mathsf{M}_2[\sigma_{12}]}{\mathsf{M}_1[\sigma_{22}]}\frac{\partial w}{\partial t}B_{y2}$$

$$-\frac{1}{2}\frac{\mathsf{M}_1[\sigma_{22}]}{\mathsf{M}_1[\sigma_{22}]}\frac{\partial w}{\partial t}B_{x1} - \frac{1}{H}\frac{\mathsf{M}_2[\sigma_{22}]}{\mathsf{M}_1[\sigma_{22}]}\frac{\partial w}{\partial t}B_{x2} + \frac{\mathsf{M}_1[\sigma_{22}]}{\mathsf{M}_1[\sigma_{22}]}\frac{\partial u}{\partial t}B_z \qquad (6\text{-}32)$$

$$-\frac{\mathsf{M}_2[\sigma_{22}]}{\mathsf{M}_1[\sigma_{22}]}\frac{\partial^2 w}{\partial x\partial t}B_z.$$

Furthermore, after applying the Kirchhoff hypothesis (3-10) and the electromagnetic hypotheses (3-20) and (6-29), the components of the Lorentz force for the lamina i read as:

$$\rho F_x^{L(i)} = \sigma_{12}^{(i)}E_x B_z + \sigma_{12}^{(i)}B_z^2\left(\frac{\partial v}{\partial t} - z\frac{\partial^2 w}{\partial y\partial t}\right) - \sigma_{12}^{(i)}B_z B_y^{(i)}\frac{\partial w}{\partial t} + \sigma_{22}^{(i)}E_y B_z$$

$$+\sigma_{22}^{(i)}B_z B_x^{(i)}\frac{\partial w}{\partial t} - \left(\sigma_{22}^{(i)}B_z^2 + \sigma_{33}^{(i)}B_y^{(i)2}\right)\left(\frac{\partial u}{\partial t} - z\frac{\partial^2 w}{\partial x\partial t}\right) + \sigma_{33}^{(i)}B_x^{(i)}B_y^{(i)}\left(\frac{\partial v}{\partial t} - z\frac{\partial^2 w}{\partial y\partial t}\right) \qquad (6\text{-}33)$$

$$+\left(\varepsilon_y-\varepsilon_0\right)E_yB_z\left(\frac{\partial^2 u}{\partial x\partial t}-z\frac{\partial^3 w}{\partial x^2\partial t}\right)-\left(\varepsilon_x-\varepsilon_0\right)E_xB_z\left(\frac{\partial^2 v}{\partial x\partial t}-z\frac{\partial^3 w}{\partial x\partial y\partial t}\right)$$

$$+\left(\varepsilon_x-\varepsilon_0\right)E_xB_y^{(i)}\frac{\partial^2 w}{\partial x\partial t}-\left(\varepsilon_y-\varepsilon_0\right)E_yB_x^{(i)}\frac{\partial^2 w}{\partial x\partial t}+J_y^{*(i)}B_z,$$

$$\rho F_y^{L(i)}=-\sigma_{12}^{(i)}E_yB_z-\sigma_{12}^{(i)}B_zB_x^{(i)}\frac{\partial w}{\partial t}+\sigma_{12}^{(i)}B_z^2\left(\frac{\partial u}{\partial t}-z\frac{\partial^2 w}{\partial x\partial t}\right)-\sigma_{11}^{(i)}E_xB_z$$

$$+\sigma_{33}^{(i)}B_x^{(i)}\left(\frac{1}{2}B_{y1}+\frac{z}{h}B_{y2}\right)\left(\frac{\partial u}{\partial t}-z\frac{\partial^2 w}{\partial x\partial t}\right)-\left(\sigma_{11}^{(i)}B_z^2+\sigma_zB_x^{(i)2}\right)\left(\frac{\partial v}{\partial t}-z\frac{\partial^2 w}{\partial y\partial t}\right)$$

$$+\sigma_{11}^{(i)}B_zB_y^{(i)}\frac{\partial w}{\partial t}+\left(\varepsilon_y-\varepsilon_0\right)E_yB_z\left(\frac{\partial^2 u}{\partial y\partial t}-z\frac{\partial^3 w}{\partial x\partial y\partial t}\right)+\left(\varepsilon_x-\varepsilon_0\right)E_xB_y^{(i)}\frac{\partial^2 w}{\partial y\partial t} \qquad (6\text{-}34)$$

$$-\left(\varepsilon_x-\varepsilon_0\right)E_xB_z\left(\frac{\partial^2 v}{\partial y\partial t}-z\frac{\partial^3 w}{\partial y^2\partial t}\right)-\left(\varepsilon_y-\varepsilon_0\right)E_yB_x^{(i)}\frac{\partial^2 w}{\partial y\partial t}-J_x^{*(i)}B_z,$$

$$\rho F_z^{L(i)}=\sigma_{12}^{(i)}E_yB_y^{(i)}+\sigma_{12}^{(i)}B_x^{(i)}B_y^{(i)}\frac{\partial w}{\partial t}-\sigma_{12}^{(i)}B_zB_y^{(i)}\left(\frac{\partial u}{\partial t}-z\frac{\partial^2 w}{\partial x\partial t}\right)$$

$$-\sigma_{12}^{(i)}E_xB_x^{(i)}-\sigma_{12}^{(i)}B_zB_x^{(i)}\left(\frac{\partial v}{\partial t}-z\frac{\partial^2 w}{\partial y\partial t}\right)-\sigma_{11}^{(i)}E_xB_y^{(i)}-\sigma_{22}^{(i)}E_yB_x^{(i)}$$

$$+\sigma_{11}^{(i)}B_zB_y^{(i)}\left(\frac{\partial v}{\partial t}-z\frac{\partial^2 w}{\partial y\partial t}\right)+\sigma_{22}^{(i)}B_zB_x^{(i)}\left(\frac{\partial u}{\partial t}-z\frac{\partial^2 w}{\partial x\partial t}\right)-\left(\sigma_{11}^{(i)}B_y^{(i)2}+\sigma_{22}^{(i)}B_x^{(i)2}\right)\frac{\partial w}{\partial t} \qquad (6\text{-}35)$$

$$-\left(\varepsilon_y-\varepsilon_0\right)E_yB_z\frac{\partial^2 w}{\partial x\partial t}+\left(\varepsilon_x-\varepsilon_0\right)E_xB_z\frac{\partial^2 w}{\partial y\partial t}+J_x^{*(i)}B_y^{(i)}-J_y^{*(i)}B_x^{(i)}.$$

where $J_x^{*(i)}$ and $J_y^{*(i)}$ are components of the external electric current, which depend on the fiber orientation in the lamina.

6.4 Solution Procedure for the Laminated Plate

The 2D system of equations of motion (6-21) and Maxwell's equations (6-30) constitutes a mathematical framework within which coupled mechanical and

electromagnetic response of electrically conductive laminated plates is studied. From the mathematical standpoint, the system of equations (6-21) and (6-30) is a nonlinear mixed system of parabolic and hyperbolic partial differential equations. This system is solved using the numerical solution procedure described in Chapter 4 of this thesis. In this section the system (6-21) and (6-30) is brought to the form suitable for implementation of the numerical solution procedure described in Chapter 4.

From Eq. (6-13), the derivatives of the middle-plane displacements with respect to the *y*-direction can be found in terms of the derivative of field variables with respect to the *x*-direction as

$$\frac{\partial w}{\partial y} = W,$$

$$\frac{\partial u}{\partial y} = q_{11}\frac{\partial u}{\partial x} + q_{12}\frac{\partial v}{\partial x} + q_{13}N_{xy} + q_{14}N_{yy} + q_{15}\frac{\partial^2 w}{\partial x^2} + q_{16}\frac{\partial W}{\partial x} + q_{17}M_{yy},$$

$$\frac{\partial v}{\partial y} = q_{21}\frac{\partial u}{\partial x} + q_{22}\frac{\partial v}{\partial x} + q_{23}N_{xy} + q_{24}N_{yy} + q_{25}\frac{\partial^2 w}{\partial x^2} + q_{26}\frac{\partial W}{\partial x} + q_{27}M_{yy}, \qquad (6\text{-}36)$$

$$\frac{\partial W}{\partial y} = q_{61}\frac{\partial u}{\partial x} + q_{62}\frac{\partial v}{\partial x} + q_{63}N_{xy} + q_{64}N_{yy} + q_{65}\frac{\partial^2 w}{\partial x^2} + q_{66}\frac{\partial W}{\partial x} + q_{67}M_{yy},$$

Here, the coefficients q_{1i}, q_{2i}, and q_{6i} are defined as below:

$$q_{11} = \frac{A_{26}B_{12}B_{22} - A_{12}A_{26}D_{22} - A_{16}B_{22}^2 - A_{22}B_{12}B_{26} + A_{12}B_{22}B_{26} + A_{22}A_{16}D_{22}}{Q},$$

$$q_{12} = \frac{-D_{22}A_{26}^2 + 2A_{26}B_{22}B_{26} - A_{66}B_{22}^2 - A_{22}B_{26}^2 + A_{22}A_{66}D_{22}}{Q},$$

$$q_{13} = \frac{B_{22}^2 - A_{22}D_{22}}{Q}, \qquad q_{14} = \frac{A_{26}D_{22} - B_{22}B_{26}}{Q},$$

$$q_{15} = \frac{-A_{26}B_{22}D_{12} + A_{26}B_{12}D_{22} + B_{16}B_{22}^2 - B_{22}B_{12}B_{26} + A_{22}B_{26}D_{12} - A_{22}B_{16}D_{22}}{Q}, \qquad (6\text{-}37)$$

$$q_{16} = \frac{2(-A_{26}B_{22}D_{26} + A_{26}B_{26}D_{22} + A_{22}B_{26}D_{26} - B_{22}B_{26}^2 + B_{66}B_{22}^2 - A_{22}B_{66}D_{22})}{Q},$$

$$q_{17} = \frac{A_{22}B_{26} - A_{26}B_{22}}{Q},$$

$$q_{21} = \frac{-A_{12}B_{26}^2 + A_{26}B_{12}B_{26} + A_{16}B_{22}B_{26} - A_{66}B_{22}B_{12} - A_{16}A_{26}D_{22} + A_{12}A_{66}D_{22}}{Q},$$

$$q_{22} = 0, \qquad q_{23} = \frac{-B_{22}B_{26} + A_{26}D_{22}}{Q}, \qquad q_{24} = \frac{B_{26}^2 - A_{66}D_{22}}{Q},$$

$$q_{25} = \frac{B_{12}B_{26}^2 - B_{22}B_{16}B_{26} - A_{26}B_{12}B_{26} + A_{66}B_{22}D_{12} - A_{66}B_{12}D_{22} + A_{26}B_{16}D_{22}}{Q}, \qquad (6\text{-}38)$$

$$q_{26} = \frac{2(B_{26}^3 - A_{26}B_{26}D_{26} - B_{22}B_{66}B_{26} - A_{66}B_{26}D_{22} + A_{66}B_{22}D_{26} + A_{26}B_{66}D_{22})}{Q},$$

$$q_{27} = \frac{-A_{26}B_{26} + A_{66}B_{22}}{Q},$$

$$q_{61} = \frac{B_{12}A_{26}^2 - A_{16}A_{26}B_{16} - A_{12}A_{26}B_{26} - A_{22}A_{66}B_{12} + A_{12}A_{66}B_{22} + A_{22}A_{16}B_{26}}{Q},$$

$$q_{62} = 0, \qquad q_{63} = \frac{B_{22}A_{26} - A_{22}B_{26}}{Q}, \qquad q_{64} = \frac{A_{26}B_{26} - A_{66}B_{22}}{Q},$$

$$q_{65} = \frac{-D_{12}A_{26}^2 + A_{26}B_{22}B_{16} + A_{26}B_{12}B_{26} - A_{66}B_{22}B_{12} - A_{22}B_{16}B_{26} + A_{22}A_{66}D_{12}}{Q}, \qquad (6\text{-}39)$$

$$q_{66} = \frac{2(-D_{26}A_{26}^2 + A_{26}B_{26}^2 + A_{26}B_{22}B_{66} - A_{66}B_{22}B_{26} - A_{22}B_{26}B_{66} + A_{22}A_{66}D_{26})}{Q},$$

$$q_{67} = \frac{A_{22}A_{66} - A_{26}^2}{Q},$$

where

$$Q = A_{26}^2 D_{22} - 2A_{26}B_{22}B_{26} + B_{26}^2 B_{22} + A_{66}(B_{22}^2 - A_{22}D_{22}). \qquad (6\text{-}40)$$

Moreover, from Eq. (6-13) the following resultants can be rewritten as:

$$N_{xx} = s_1 M_{yy} + s_2 N_{xy} + s_3 \frac{\partial v}{\partial x} + s_4 \frac{\partial u}{\partial x} + s_5 N_{yy} + s_6 \frac{\partial^2 w}{\partial x^2} + s_7 \frac{\partial W}{\partial x},$$

$$M_{xx} = f_1 M_{yy} + f_2 N_{xy} + f_3 \frac{\partial v}{\partial x} + f_4 \frac{\partial u}{\partial x} + f_5 N_{yy} + f_6 \frac{\partial^2 w}{\partial x^2} + f_7 \frac{\partial W}{\partial x}, \qquad (6\text{-}41)$$

$$M_{xy} = l_1 M_{yy} + l_2 N_{xy} + l_3 \frac{\partial v}{\partial x} + l_4 \frac{\partial u}{\partial x} + l_5 N_{yy} + l_6 \frac{\partial^2 w}{\partial x^2} + l_7 \frac{\partial W}{\partial x},$$

where

$$s_1 = A_{16}q_{17} + A_{12}q_{27} - B_{12}q_{67}, \qquad s_2 = A_{16}q_{13} + A_{12}q_{23} - B_{12}q_{63},$$
$$s_3 = A_{16}(q_{12}+1) + A_{12}q_{22} - B_{12}q_{62}, \quad s_4 = A_{16}q_{11} + A_{12}q_{21} - B_{12}q_{61} + A_{11},$$
$$s_5 = A_{16}q_{14} + A_{12}q_{24} - B_{12}q_{64}, \qquad s_6 = A_{16}q_{15} + A_{12}q_{25} - B_{12}q_{65} - B_{11}, \qquad (6\text{-}42)$$
$$s_7 = A_{16}q_{16} + A_{12}q_{26} - B_{12}q_{66} - 2B_{16},$$

$$f_1 = B_{16}q_{17} + B_{12}q_{27} - D_{12}q_{67}, \qquad f_2 = B_{16}q_{13} + B_{12}q_{23} - D_{12}q_{63},$$
$$f_3 = B_{16}(q_{12}+1) + B_{12}q_{22} - D_{12}q_{62}, \quad f_4 = B_{16}q_{11} + B_{12}q_{21} - D_{12}q_{61} + B_{11},$$
$$f_5 = B_{16}q_{14} + B_{12}q_{24} - D_{12}q_{64}, \qquad f_6 = B_{16}q_{15} + B_{12}q_{25} - D_{12}q_{65} - D_{11}, \qquad (6\text{-}43)$$
$$f_7 = B_{16}q_{16} + B_{12}q_{26} - D_{12}q_{66} - 2D_{12},$$

$$l_1 = B_{66}q_{17} + B_{26}q_{27} - D_{26}q_{67}, \qquad l_2 = B_{66}q_{13} + B_{26}q_{23} - D_{26}q_{63},$$
$$l_3 = B_{66}(q_{12}+1) + B_{26}q_{22} - D_{26}q_{62}, \quad l_4 = B_{66}q_{11} + B_{26}q_{21} - D_{26}q_{61} - B_{16},$$
$$l_5 = B_{66}q_{14} + B_{26}q_{24} - D_{26}q_{64}, \qquad l_6 = B_{66}q_{15} + B_{26}q_{25} - D_{26}q_{65} - D_{16}, \qquad (6\text{-}44)$$
$$l_7 = B_{66}q_{16} + B_{26}q_{26} - D_{26}q_{66} - 2D_{66}.$$

Using Eqs. (6-13), (6-32) and (6-41) together with the Lorentz force (6-33), (6-34), and (6-35), the following first derivatives of resultants with respect to the *y*-direction can be derived from the equations of motion (6-21):

$$\frac{\partial N_{xy}}{\partial y} = \rho H \frac{\partial^2 u}{\partial t^2} - s_1 \frac{\partial M_{yy}}{\partial x} - s_2 \frac{\partial N_{xy}}{\partial x} - s_3 \frac{\partial^2 v}{\partial x^2} - s_4 \frac{\partial^2 u}{\partial x^2} - s_5 \frac{\partial N_{yy}}{\partial x} - s_6 \frac{\partial^3 w}{\partial x^3}$$
$$- s_7 \frac{\partial^2 W}{\partial x^2} + \frac{H}{\mu} B_z \frac{\partial B_z}{\partial x} + \frac{1}{4} \mathsf{M}_1[\sigma_{33}]B_{y1}^2 \frac{\partial u}{\partial t} - \frac{1}{4} \mathsf{M}_2[\sigma_{33}]B_{y1}^2 \frac{\partial^2 w}{\partial x\,\partial t}$$
$$+ (\varepsilon_x - \varepsilon_0) H E_x B_z \frac{\partial^2 v}{\partial x\,\partial t} - \frac{H}{2}(\varepsilon_x - \varepsilon_0) B_{y1} E_x \frac{\partial^2 w}{\partial x\,\partial t} - \mathsf{M}_1[J_y^*(t)]B_z$$

$$(6\text{-}45)$$

$$\frac{\partial N_{yz}}{\partial y} = \rho H \frac{\partial^2 w}{\partial t^2} + p(y,t) - \frac{\partial N_{xz}}{\partial x} + q_{82} B_{y1} E_x + q_{82} B_{y1} B_z \frac{\partial v}{\partial t} + q_{86} B_{y1} B_z \frac{\partial W}{\partial t}$$
$$+ q_{85} B_{y1}^2 \frac{\partial w}{\partial t} + q_{80} B_{y1} \frac{\partial B_z}{\partial x} + q_{85}' B_{y1} B_z \frac{\partial^2 w}{\partial x\,\partial t} - (\varepsilon_x - \varepsilon_0) H E_x B_z \frac{\partial W}{\partial t}$$
$$+ \frac{1}{2} B_{y1} \mathsf{M}_1[J_x^*(t)],$$

$$\frac{\partial N_{yy}}{\partial y} = \rho H \frac{\partial^2 v}{\partial t^2} - \frac{\partial N_{xy}}{\partial x} + q_{42} E_x B_z + q_{42} B_z^2 \frac{\partial v}{\partial t} + q_{46} B_z^2 \frac{\partial W}{\partial t}$$

$$+ q_{45} B_{y1} B_z \frac{\partial w}{\partial t} + q_{45}' B_z^2 \frac{\partial w}{\partial t} + q_{40} B_z \frac{\partial B_z}{\partial x}$$

$$+ \left(\varepsilon_x - \varepsilon_0 \right) H E_x B_z (q_{21} \frac{\partial u}{\partial x} + q_{22} \frac{\partial v}{\partial x} + q_{23} N_{xy} + q_{24} N_{yy}$$

$$+ q_{25} \frac{\partial^2 w}{\partial x^2} + q_{26} \frac{\partial W}{\partial x} + q_{27} M_{yy}) - \frac{H}{2} \left(\varepsilon_x - \varepsilon_0 \right) B_{y1} E_x \frac{\partial W}{\partial t} + \mathsf{M}_1 [J_x^*(t)] B_z,$$

$$\frac{\partial M_{yy}}{\partial y} = -\frac{\rho H^3}{12} \frac{\partial^2 W}{\partial t^2} + N_{yz} - l_1 \frac{\partial M_{yy}}{\partial x} + l_2 \frac{\partial N_{xy}}{\partial x} + l_3 \frac{\partial^2 v}{\partial x^2} + l_4 \frac{\partial^2 u}{\partial x^2} + l_5 \frac{\partial N_{yy}}{\partial x}$$

$$+ l_6 \frac{\partial^3 w}{\partial x^3} + l_7 \frac{\partial^2 W}{\partial x^2} - + q_{72} E_x B_z + q_{72} B_z^2 \frac{\partial v}{\partial t} + q_{76} B_z^2 \frac{\partial W}{\partial t} + q_{75} B_{y1} B_z \frac{\partial w}{\partial t}$$

$$+ q_{75}' B_z^2 \frac{\partial^2 w}{\partial x \partial t} + q_{70} B_z \frac{\partial B_z}{\partial x} - \frac{H^3}{12} \left(\varepsilon_x - \varepsilon_0 \right) E_x B_z (q_{61} \frac{\partial u}{\partial x} + q_{62} \frac{\partial v}{\partial x} + q_{63} N_{xy}$$

$$+ q_{64} N_{yy} + q_{65} \frac{\partial^2 w}{\partial x^2} + q_{66} \frac{\partial W}{\partial x} + q_{67} M_{yy}) + \mathsf{M}_2 [J_x^*(t)] B_z.$$

in which B_{y2} and B_x are considered to be zero ($B_{y2} = B_{x1} = B_{x2} = 0$). The coefficients q_{ij} are:

$$q_{42} = \mathsf{M}_1 [\sigma_{11}] - \frac{\mathsf{M}_1^2 [\sigma_{12}]}{\mathsf{M}_1 [\sigma_{22}]}, \quad q_{46} = \frac{\mathsf{M}_1 [\sigma_{12}] \mathsf{M}_2 [\sigma_{12}]}{\mathsf{M}_1 [\sigma_{22}]} - \mathsf{M}_2 [\sigma_{11}],$$

$$q_{45} = \frac{1}{2} \left(\frac{\mathsf{M}_1^2 [\sigma_{12}]}{\mathsf{M}_1 [\sigma_{22}]} - \mathsf{M}_1 [\sigma_{11}] \right), \quad q_{45}' = \mathsf{M}_2 [\sigma_{12}] - \frac{\mathsf{M}_1 [\sigma_{12}] \mathsf{M}_2 [\sigma_{22}]}{\mathsf{M}_1 [\sigma_{22}]},$$

$$q_{40} = -\frac{H}{\mu} \frac{\mathsf{M}_1 [\sigma_{12}]}{\mathsf{M}_1 [\sigma_{22}]},$$

$$\text{(6-46)}$$

$$q_{72} = \mathsf{M}_2 [\sigma_{11}] - \frac{\mathsf{M}_1 [\sigma_{12}] \mathsf{M}_2 [\sigma_{12}]}{\mathsf{M}_1 [\sigma_{22}]}, \quad q_{76} = \frac{\mathsf{M}_2^2 [\sigma_{12}]}{\mathsf{M}_1 [\sigma_{22}]} - \mathsf{M}_3 [\sigma_{11}],$$

$$q_{75} = \frac{1}{2} \left(\frac{\mathsf{M}_1 [\sigma_{12}] \mathsf{M}_2 [\sigma_{12}]}{\mathsf{M}_1 [\sigma_{22}]} - \mathsf{M}_2 [\sigma_{11}] \right), \quad q_{75}' = \mathsf{M}_3 [\sigma_{12}] - \frac{\mathsf{M}_2 [\sigma_{12}] \mathsf{M}_2 [\sigma_{22}]}{\mathsf{M}_1 [\sigma_{22}]},$$

$$q_{70} = -\frac{H}{\mu} \frac{\mathsf{M}_2 [\sigma_{12}]}{\mathsf{M}_1 [\sigma_{22}]},$$

$$q_{82} = \frac{1}{2}\left(\frac{\mathsf{M}_1^2[\sigma_{12}]}{\mathsf{M}_1[\sigma_{22}]} - \mathsf{M}_1[\sigma_{11}] \right), \quad q_{86} = -\frac{1}{2}\left(\frac{\mathsf{M}_1[\sigma_{12}]\mathsf{M}_2[\sigma_{12}]}{\mathsf{M}_1[\sigma_{22}]} - \mathsf{M}_2[\sigma_{11}] \right),$$

$$q_{85} = \frac{1}{4}\left(\mathsf{M}_1[\sigma_{11}] - \frac{\mathsf{M}_1^2[\sigma_{12}]}{\mathsf{M}_1[\sigma_{22}]} \right), \quad q'_{85} = \frac{1}{2}\left(\frac{\mathsf{M}_1[\sigma_{12}]\mathsf{M}_2[\sigma_{22}]}{\mathsf{M}_1[\sigma_{22}]} - \mathsf{M}_2[\sigma_{12}] \right),$$

$$q_{80} = \frac{1}{2}\frac{H}{\mu}\frac{\mathsf{M}_1[\sigma_{12}]}{\mathsf{M}_1[\sigma_{22}]},$$

The stress resultant N_{xz} in the equation of N_{yz} in Eq. (6-45) can be found from the equations of motion in the form:

$$
\begin{aligned}
N_{xz} &= \frac{\rho H^3}{12}\frac{\partial^3 w}{\partial x \partial t^2} - \frac{\rho H^3}{12}l_1\frac{\partial^2 W}{\partial t^2} + \rho H\, l_2\frac{\partial^2 u}{\partial t^2} + \rho H\, l_5\frac{\partial^2 v}{\partial t^2} + l_1 N_{yz} \\
&+ q_{31}\frac{\partial^2 u}{\partial x^2} + q_{32}\frac{\partial^2 v}{\partial x^2} + q_{33}\frac{\partial N_{xy}}{\partial x} + q_{34}\frac{\partial N_{yy}}{\partial x} + q_{35}\frac{\partial^3 w}{\partial x^3} + q_{36}\frac{\partial^2 W}{\partial x^2} + q_{37}\frac{\partial M_{yy}}{\partial x} \\
&+ q'_{31}E_x B_z\frac{\partial^2 u}{\partial x \partial t} + q'_{32}E_x B_z\frac{\partial^2 v}{\partial x \partial t} + q'_{33}E_x B_z\frac{\partial N_{xy}}{\partial t} + q'_{34}E_x B_z\frac{\partial N_{yy}}{\partial t} \\
&+ q'_{35}E_x B_z\frac{\partial^3 w}{\partial x^2 \partial t} + q'_{36}E_x B_z\frac{\partial^2 W}{\partial x \partial t} + q'_{37}E_x B_z\frac{\partial M_{yy}}{\partial t} \\
&+ q_{51}\left(E_x B_z + B_z^2\frac{\partial v}{\partial t}\right) + q_{52}B_z^2\frac{\partial W}{\partial t} + q_{53}B_{y1}B_z\frac{\partial w}{\partial t} + q_{54}B_z^2\frac{\partial^2 w}{\partial x \partial t} + q_{50}B_z\frac{\partial B_z}{\partial x} \\
&+ q'_{51}B_{y1}^2\frac{\partial u}{\partial t} + q'_{52}B_{y1}^2\frac{\partial^2 w}{\partial x \partial t} + q'_{53}B_{y1}E_x\frac{\partial^2 w}{\partial x \partial t} + q'_{54}B_{y1}E_x\frac{\partial W}{\partial t} + \\
&+ \mathsf{M}_1[J_x^*(t)]l_5 B_z - \mathsf{M}_1[J_y^*(t)]l_2 B_z + \mathsf{M}_2[J_y^*(t)]B_z.
\end{aligned}
\tag{6-47}
$$

where

$$
\begin{aligned}
q_{31} &= f_4 - l_1 l_4 - s_4 l_2 + q_{21}l_3 + q_{11}l_4 + q_{61}l_7, \\
q_{32} &= f_3 - l_1 l_3 - s_3 l_2 + q_{22}l_3 + q_{12}l_4 + q_{62}l_7, \\
q_{33} &= f_2 - l_1 l_2 - s_2 l_2 + q_{23}l_3 + q_{13}l_4 + q_{63}l_7, \\
q_{34} &= f_5 - l_1 l_5 - s_5 l_2 + q_{24}l_3 + q_{14}l_4 + q_{64}l_7, \\
q_{35} &= f_6 - l_1 l_6 - s_6 l_2 + q_{25}l_3 + q_{15}l_4 + q_{65}l_7, \\
q_{36} &= f_7 - l_1 l_7 - s_7 l_2 + q_{26}l_3 + q_{16}l_4 + q_{66}l_7 + l_6, \\
q_{37} &= f_1 - l_1^2 - s_1 l_2 + q_{27}l_3 + q_{17}l_4 + q_{67}l_7,
\end{aligned}
\tag{6-48}
$$

$$q'_{31} = (\varepsilon_x - \varepsilon_0) H \left(q_{21} l_4 - \frac{H^2}{12} q_{61} l_1 \right), \quad q'_{32} = (\varepsilon_x - \varepsilon_0) H \left(q_{22} l_5 - \frac{H^2}{12} q_{62} l_1 + l_2 \right),$$

$$q'_{33} = (\varepsilon_x - \varepsilon_0) H \left(q_{23} l_5 - \frac{H^2}{12} q_{63} l_1 \right), \quad q'_{34} = (\varepsilon_x - \varepsilon_0) H \left(q_{24} l_5 - \frac{H^2}{12} q_{64} l_1 \right),$$

$$q'_{35} = (\varepsilon_x - \varepsilon_0) H \left(q_{25} l_5 - \frac{H^2}{12} q_{65} l_1 \right), \quad q'_{36} = (\varepsilon_x - \varepsilon_0) H \left(q_{26} l_5 - \frac{H^2}{12} (q_{66} l_1 - 1) \right)$$

$$q'_{37} = (\varepsilon_x - \varepsilon_0) H \left(q_{27} l_5 - \frac{H^2}{12} q_{67} l_1 \right),$$

$$q_{51} = q_{72} l_1 + q_{42} l_5 + q_{451}, \qquad q_{52} = q_{76} l_1 + q_{46} l_5 - q_{751},$$

$$q_{53} = q_{75} l_1 + q_{45} l_5 + q_{851}, \qquad q_{54} = q_{751} l_1 + q_{451} l_5 + \mathsf{M}_3[\sigma_{22}] - \frac{\mathsf{M}_2^2[\sigma_{22}]}{\mathsf{M}_1[\sigma_{22}]},$$

$$q_{50} = q_{70} l_1 + l_2 \frac{H}{\mu} + 2 q_{80} l_5 + \frac{\mathsf{M}_2[\sigma_{22}]}{\mathsf{M}_1[\sigma_{22}]} \frac{H}{\mu}$$

$$q'_{51} = \frac{1}{4} \left(\mathsf{M}_1[\sigma_{33}] l_1 - \mathsf{M}_2[\sigma_{33}] \right), \qquad q'_{52} = \frac{1}{4} \left(\mathsf{M}_3[\sigma_{33}] - \mathsf{M}_2[\sigma_{33}] l_2 \right),$$

$$q'_{53} = -\frac{H}{2} (\varepsilon_x - \varepsilon_0) l_2, \quad q'_{54} = -\frac{H}{2} (\varepsilon_x - \varepsilon_0) l_5,$$

For the electromagnetic governing equations, considering $B_x = B_{y2} = 0$, from (6-31) we can write:

$$\frac{\partial B_z}{\partial y} = q_{02} E_x + q_{02} \frac{\partial v}{\partial t} B_z + q_{06} \frac{\partial W}{\partial t} B_z + q_{05} B_{y1} \frac{\partial w}{\partial t} + q'_{05} \frac{\partial^2 w}{\partial x \partial t} B_z + q_{00} \frac{\partial B_z}{\partial x}, \qquad (6\text{-}49)$$

where

$$q_{02} = \frac{\mu}{H} \left(\mathsf{M}_1[\sigma_{11}] - \frac{\mathsf{M}_1^2[\sigma_{12}]}{\mathsf{M}_1[\sigma_{22}]} \right), \quad q_{06} = \frac{\mu}{H} \left(\frac{\mathsf{M}_1[\sigma_{12}] \mathsf{M}_2[\sigma_{12}]}{\mathsf{M}_1[\sigma_{22}]} - \mathsf{M}_2[\sigma_{11}] \right),$$

$$q_{05} = \frac{\mu}{2H} \left(\frac{\mathsf{M}_1^2[\sigma_{12}]}{\mathsf{M}_1[\sigma_{22}]} - \mathsf{M}_1[\sigma_{11}] \right), \quad q'_{05} = \frac{\mu}{H} \left(\mathsf{M}_2[\sigma_{12}] - \frac{\mathsf{M}_1[\sigma_{12}] \mathsf{M}_2[\sigma_{22}]}{\mathsf{M}_1[\sigma_{22}]} \right), \qquad (6\text{-}50)$$

$$q_{00} = -\frac{\mathsf{M}_1[\sigma_{12}]}{\mathsf{M}_1[\sigma_{22}]}.$$

The last governing equation can be obtained from the third equations of (3.37) and (6-32) as:

$$\frac{\partial E_x}{\partial y} = \frac{\partial B_z}{\partial x} - \frac{H}{\mu \mathsf{M}_1[\sigma_{22}]}\frac{\partial^2 B_z}{\partial x^2} - \frac{\mathsf{M}_1[\sigma_{12}]}{\mathsf{M}_1[\sigma_{22}]}\frac{\partial E_x}{\partial x} + \frac{\mathsf{M}_1[\sigma_{12}]}{2\mathsf{M}_1[\sigma_{22}]}B_{y1}\frac{\partial^2 w}{\partial t \partial x}$$

$$+ \frac{\mathsf{M}_2[\sigma_{12}]}{\mathsf{M}_1[\sigma_{22}]}\left(\frac{\partial^2 W}{\partial t \partial x}B_z + \frac{\partial W}{\partial t}\frac{\partial B_z}{\partial x}\right) - \frac{\mathsf{M}_1[\sigma_{12}]}{\mathsf{M}_1[\sigma_{22}]}\left(\frac{\partial^2 v}{\partial t \partial x}B_z + \frac{\partial v}{\partial t}\frac{\partial B_z}{\partial x}\right)$$

$$+ \frac{\mathsf{M}_1[\sigma_{22}]}{\mathsf{M}_1[\sigma_{22}]}\left(\frac{\partial^2 u}{\partial t \partial x}B_z + \frac{\partial u}{\partial t}\frac{\partial B_z}{\partial x}\right) - \frac{\mathsf{M}_2[\sigma_{22}]}{\mathsf{M}_1[\sigma_{22}]}\left(\frac{\partial^3 w}{\partial t \partial x^2}B_z + \frac{\partial^2 w}{\partial x \partial t}\frac{\partial B_z}{\partial x}\right). \tag{6-51}$$

Finally, the tenth-order system of governing equations for a laminated plate includes the four equations of (6-36), the four equations of (6-45) and two electromagnetic equations of (6-49) and (6-51).

6.5 Numerical Results for the Laminated Plate

To investigate the response of a laminated plate subjected to mechanical (5-3) and electromagnetic (5-1) and (5-2) loads, the system of governing equations developed in the previous section is solved by the numerical solution procedure introduced in Chapter 4. For the sake of simplicity, only symmetric cross-ply laminates with layers of equal thickness are considered in this study. In a symmetric cross-ply laminate, the geometry and material properties of the layers are symmetric with respect to the middle plane of the laminate and the fiber orientations of the layers are either $\theta = 0°$ or $\theta = 90°$. In such laminates, there is no bending-extension coupling (B_{ij} are zero in Eqs. (6-15) and (6-16)). Moreover, we have $A_{16} = A_{26} = 0$. Thus, the equations of the resultants (Eq. (6-20)) are significantly simplified for the case of symmetric cross-ply laminates. Due to the ease

of manufacturing and analysis, these types of laminates are widely used in civil and aerospace industries.

In this study, laminates of four, eight and sixteen layers are considered and the material properties of each unidirectional fiber reinforced composite layer are those used for the finite plate in Section 5.2. Laminates are assumed to be made of the AS4/3501-6 unidirectional carbon fiber reinforced polymer matrix composite with 60% fiber volume fraction. The material properties of the composite are as follows: density $\rho = 1594 \text{ kg/m}^3$, Young's moduli in fiber direction, $E_1 = 102.97 \text{ GPa}$ and in transverse direction, $E_2 = 7.55 \text{ GPa}$; Poisson's ratios, $\nu_{21} = \nu_{13} = 0.3$; electric conductivity in fiber direction, $\sigma_1 = 39000 \text{ S/m}$. The electric conductivities of the composite perpendicular to the fiber direction are considered to be $\sigma_2 = \sigma_3 = 10^{-4}\sigma_1$. The width of the laminated plate is $a = 0.1524 \text{ m}$, the length is l, and the thickness is $H = 0.0021 \text{m}$.

Four different types of laminates are analyzed and compared. All laminates have the same thickness $H = 0.0021 \text{m}$, but are different in the number of layers and ply sequences. The so-called single-layer plate consists of one transversely isotropic layer with principal material directions coinciding with the laminate coordinate axes. The 4-layer laminate is laid up in the form $[0/90/90/0]$ or $[0/90]_s$, where subscript s stands for "symmetric". Similarly, the 8-layer and 16-layer laminates are defined as $[0/90/0/90]_s$ and $[0/90/0/90/0/90/0/90]_s$, respectively.

Simply-supported boundary conditions are assumed as in Eqs. (5-28) – (5-32), and a laminated plate is assumed to be subjected to a transient mechanical load Eq. (5-3) with the characteristic time $\tau_p = 10 \text{ms}$ and maximum pressure $p_0 = 1 \text{ MPa}$, constant in-plane magnetic field (5-10) and pulsed electric current (5-3), where $\tau_c = \tau_p = 10 \text{ ms}$. Moreover, in all numerical studies the time step was $dt = 10^{-4}$ s, and $n_x = 5$, while $n_y = 10000$. The half-size of the contact zone is $b = h/10$.

First, the effect of the aspect ratio on the response of the laminated plates subjected to the mechanical load with no electromagnetic load is discussed. Figs. 52 and

53 show middle plane transverse deflection, w, in the center of the plate $(x=0, y=0)$ for a long ($l=10a$) and square ($a=0.1524\,\mathrm{m}$) plates, respectively. As it can be seen, adding layers with fiber orientations of $\theta=90°$ to those of $\theta=0°$ significantly reduces deflection of the laminate. Moreover, the frequent use of the layers of $\theta=90°$ in between the plies of $\theta=0°$ will result in the further increase in the impact resistance of the laminated plate. Furthermore, as it was expected, the magnitude of the vibrations in the long plate is larger than in the short plate.

A similar trend can be observed when, in addition to the mechanical load, an electromagnetic load is applied to the laminated plate. In Figure 54, a pulsed electric current and an external magnetic induction ($B_y^*=1.0$ T) are applied together with the mechanical load. The results are shown for the square laminated plate.
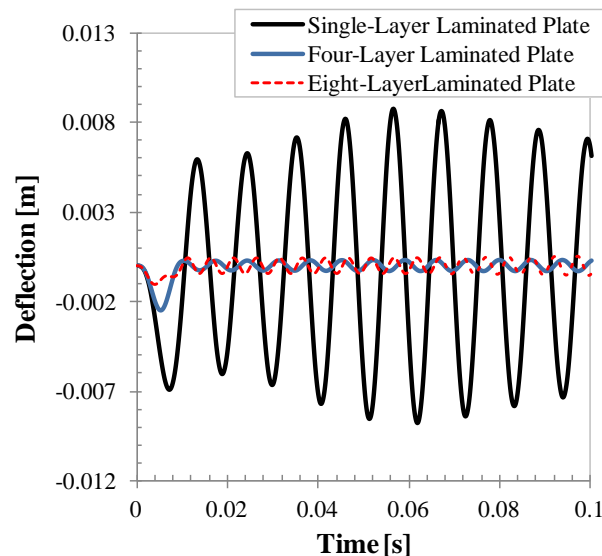

Figure 52. Deflection of the long laminated plate: effect of the ply sequence with no electromagnetic load applied.
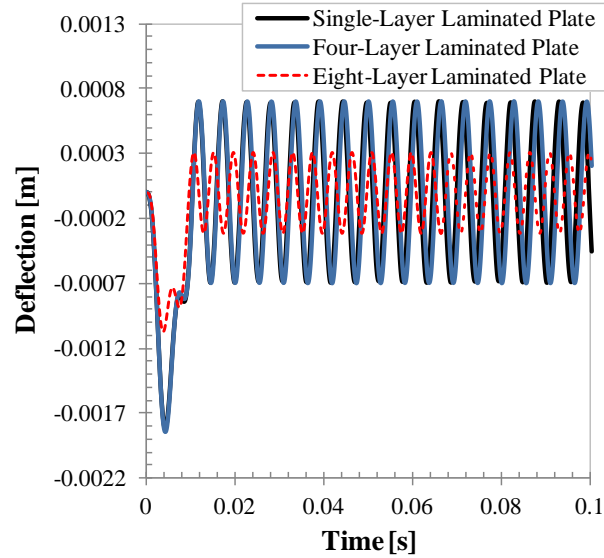
Figure 53. Deflection of the square laminated plate: effect of the ply sequence with no electromagnetic load applied.
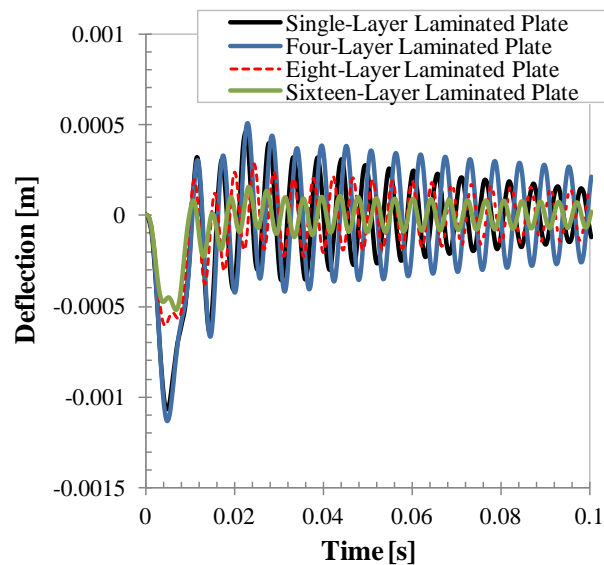

Figure 54. Deflection of the square laminated plate: effect of the ply sequence in the presence of an electromagnetic field

Note that the amount of the electric current that the laminated plates conduct is the same, but since only half of the layers of the laminates which possess plies with fiber orientations of $\theta = 90°$ in their stack, are conductive, the current density in the cross-ply laminates was taken twice ($J_0 = 2.10^6 \ \text{A/m}^2$) of that applied to a single-layer composite, in which all fiber are oriented in the same direction. It can be seen, that addition of the magnetic induction leads to the decay in the plate vibrations.

Next, the response of the laminated plates under various electromagnetic loads is discussed. Figure 55 to Figure 60 show the effect of the magnitude of the external magnetic induction, B_y^*. Each figure shows the results for single-layer, 4-layer, 8-layer, and 16-layer plates subjected to the same mechanical and electromagnetic loads. Thus, emphasizing the difference in the number of layers on the response of the plate. Figure 55 shows deflection of the different laminated plates subjected to the pulsed electric current, $J_0 = 10^5 \ \text{A/m}^2 \ \ \tau_c = \tau_p = 10 \ \text{ms}$, and low magnetic induction $B_y^* = 0.1 \ \text{T}$. As it was noted earlier, the thickness of the laminated plates is the same, while the ply sequence is different in 4-layer, 8-layer, and 16-layer symmetric cross-ply laminates.

Figures 56 and 57 show deflections for the laminated plates with large magnetic induction $B_y^* = 1.0 \ \text{T}$ and $B_y^* = 2.0 \ \text{T}$, correspondingly. The pulsed electric current is characterized by $J_0 = 10^5 \ \text{A/m}^2$ and $\tau_c = \tau_p = 10 \ \text{ms}$.

Figure 58 to Figure 60 show the effect of increasing of magnetic induction on the deflection of the 4-layer, 8-layer, and 16-layer laminated plates, correspondingly. The pulsed electric current is characterized by $J_0 = 10^5 \ \text{A/m}^2$ and $\tau_c = \tau_p = 10 \ \text{ms}$ and is the same for all cases, while magnetic induction is different and $B_y^* = 0.1 \ \text{T}$, $B_y^* = 1.0 \ \text{T}$ and $B_y^* = 2.0 \ \text{T}$, respectively. The results for the laminates subjected to mechanical load with no electromagnetic load are also presented.
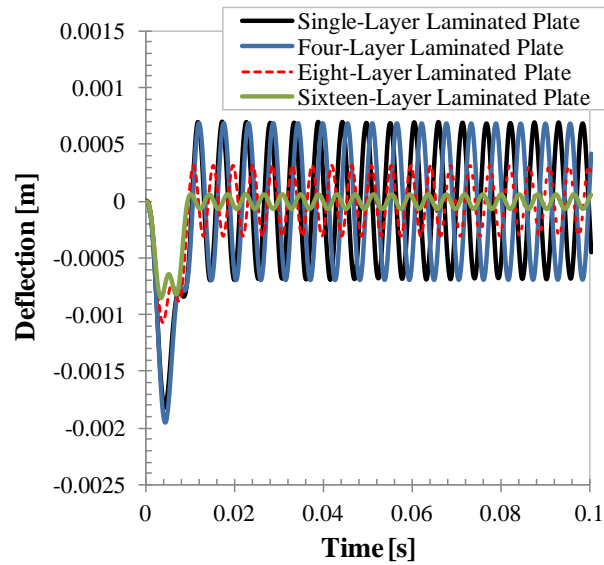
Figure 55. Deflection of the square laminated plate: effect of the number of layers and low magnetic induction, $B_y^* = 0.1 \, \text{T}$.
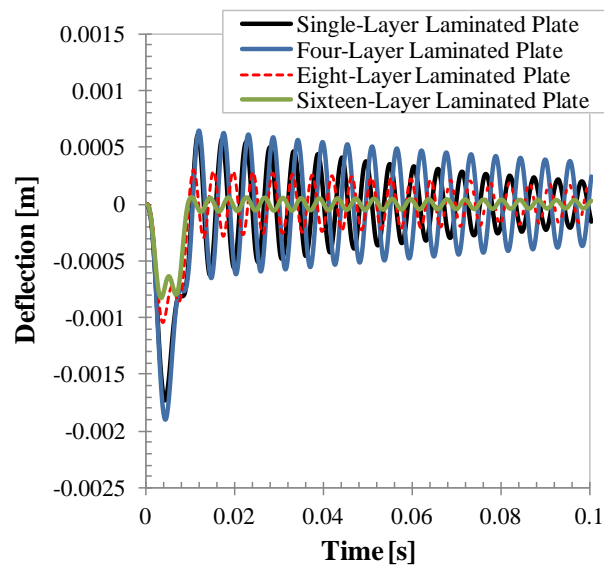

Figure 56. Deflection of the square laminated plate: effect of the number of layers and magnetic induction, $B_y^* = 1.0 \, \text{T}$.
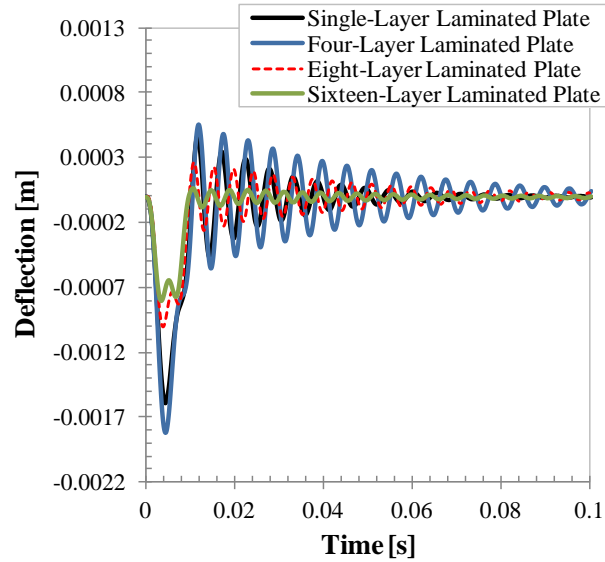
Figure 57. Deflection of the square laminated plate: effect of the number of layers and magnetic induction, $B_y^* = 2.0\,\mathrm{T}$.
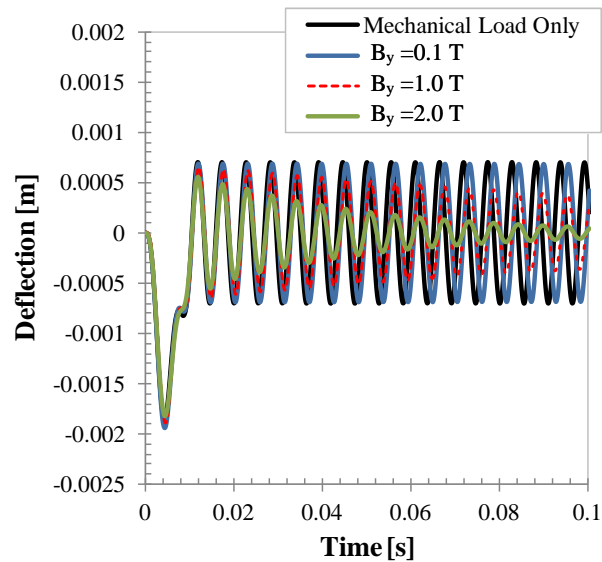

Figure 58. Deflection of the 4-layer square laminated plate: effect of increasing magnetic induction.
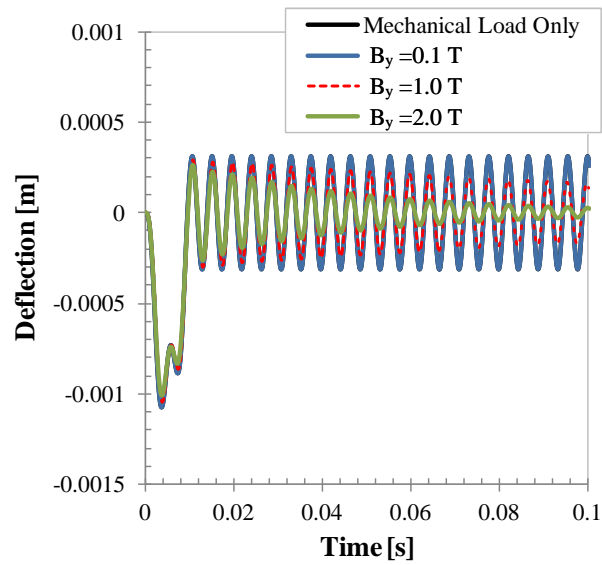
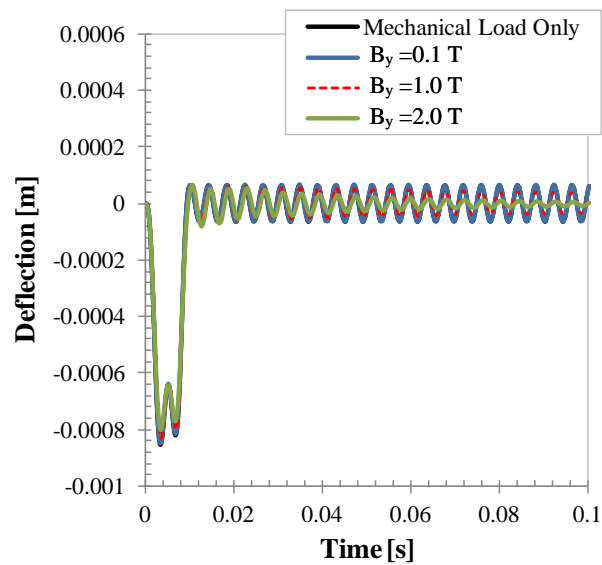Figure 59. Deflection of the 8-layer square laminated plate: effect of increasing magnetic induction.

Figure 60. Deflection of the 16-layer square laminated plate: effect of increasing magnetic induction.

Several conclusions can be drawn based on the results presented in Figs. 54-60. It can be seen that there is a small reduction in the maximum deflection and stress as the number of $90°$ layers increases. This stays true even in the presence of a high strength magnetic field. It can also be seen that vibration magnitude decays faster as the number of $90°$ layers decreases. Overall, the influence of an electromagnetic field on the dynamic mechanical response of the laminated composites is most apparent in the unidirectional composites.

The effect of the magnitude of the electric current density on the deflection of the 4-layer, 8-layer, and 16-layer laminates is presented in Figure 61 to Figure 63. Here, the magnetic induction is $B_y^* = 0.1\,\text{T}$ for all the cases, while the current density differs. As it can be seen, there is some reduction in the deflection at larger current densities, but the noticeable reduction occurs only during the application of the impact load. The reduction in the vibration amplitudes after the impact load has diminished is small. Moreover, it practically disappears as the number of layers in the laminate increases. Furthermore, the damping effect is also ignorable when the magnetic field is small.

The mechanical response of the 4-layer, 8-layer, and 16-layer laminates in the presence of the large magnetic field, $B_y^* = 1.0\,\text{T}$, is shown in Figure 64 to Figure 66. Now that the magnetic field is relatively large, the deflection of the plate is further reduced at least during the application of the impact load. Moreover, the damping effect is also more noticeable.

As for the electrical conductivity, an increase in the conductivity tends to decrease the amplitude of the plate vibrations, but the effect is small even for strong magnetic field and high electric current. Moreover, this effect diminishes as the number of layers in the laminate increases. Figure 67 to Figure 69 illustrate the results. The characteristics of the pulsed electric current are $J_0 = 10^6\,\text{A/m}^2$ and $\tau_c = \tau_p = 10\,\text{ms}$. The magnetic induction is $B_y^* = 1.0\,\text{T}$.

Figure 61. Deflection of the 4-layer square laminated plate: effect of increasing electric current at $B_y^* = 0.1$ T .

Figure 62. Deflection of the 8-layer square laminated plate: effect of increasing electric current at $B_y^* = 0.1$ T .

Figure 63. Deflection of the 16-layer square laminated plate: effect of increasing

electric current at $B_y^* = 0.1$ T .

Figure 64. Deflection of the 4-layer square laminated plate: effect of increasing

electric current at $B_y^* = 1.0$ T .

Figure 65. Deflection of the 8-layer square laminated plate: effect of increasing

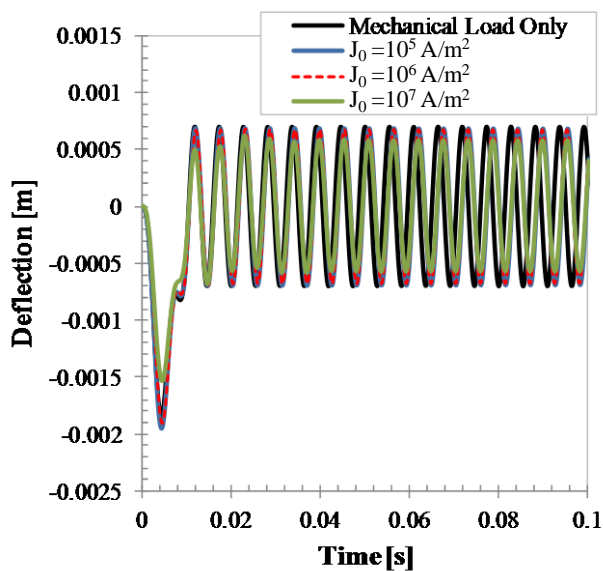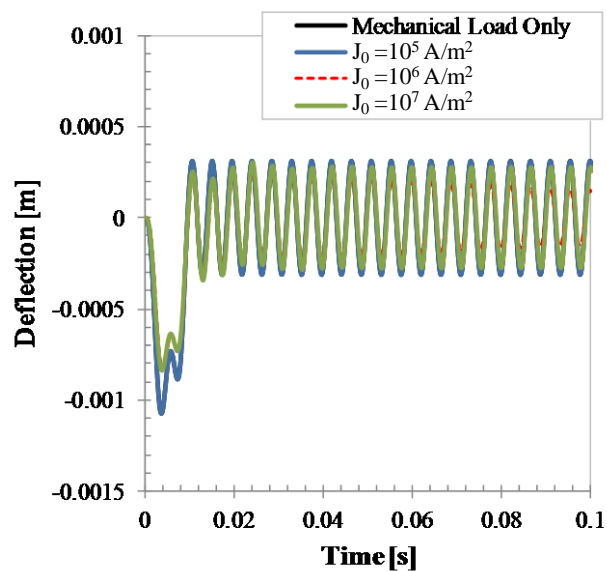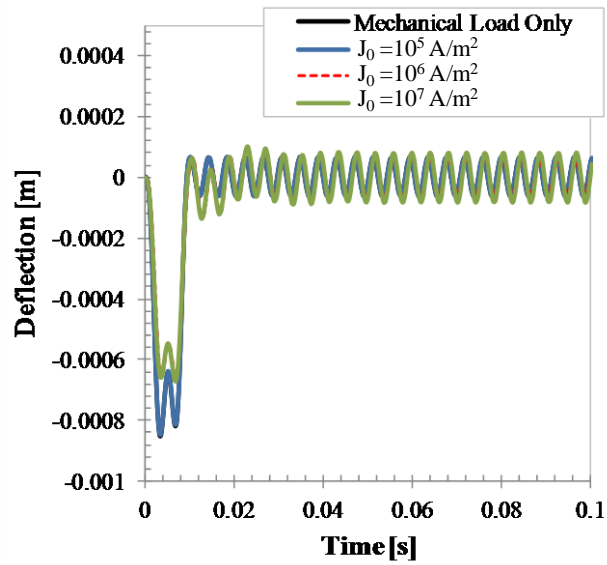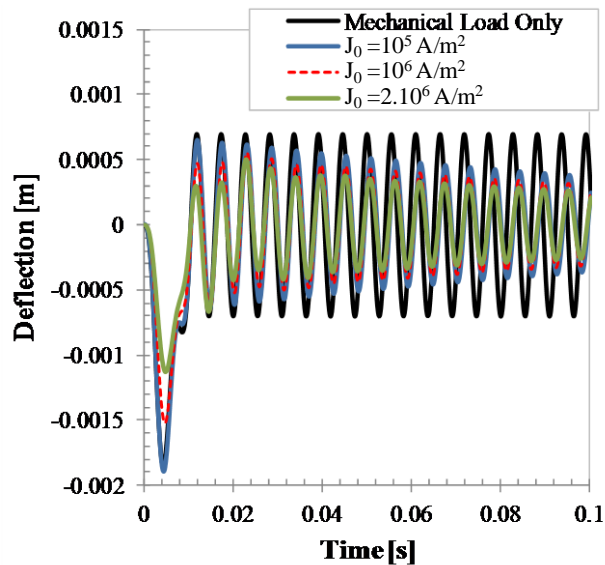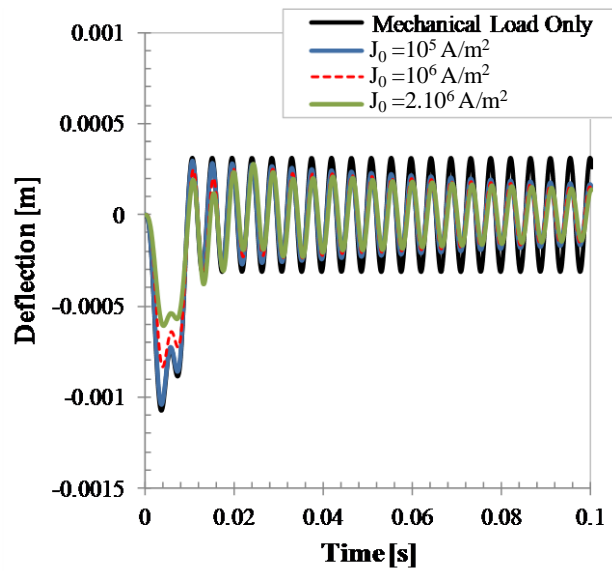electric current at $B_y^* = 1.0$ T .
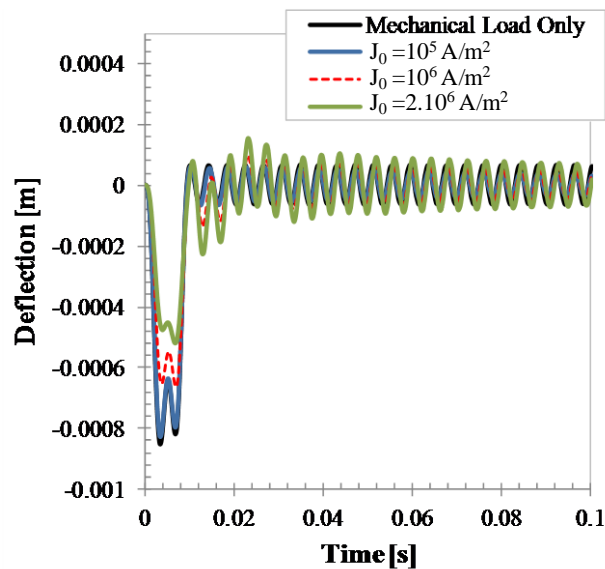
Figure 66. Deflection of the 16-layer square laminated plate: effect of increasing

electric current at $B_y^* = 1.0$ T .
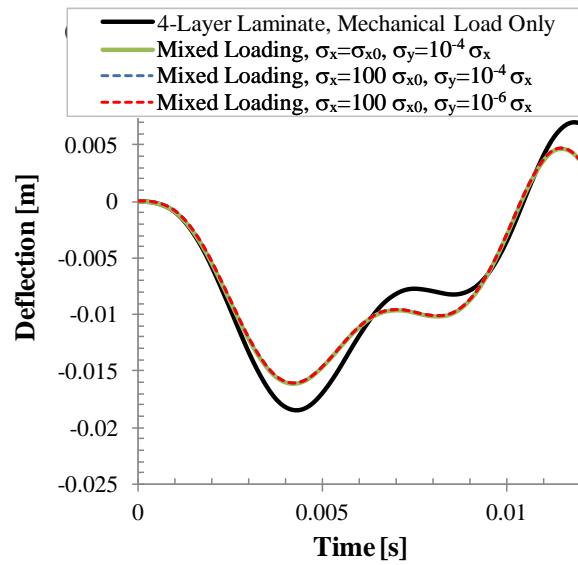
Figure 67. Deflection of the 4-layer square laminated plate: effect of increasing electrical conductivity
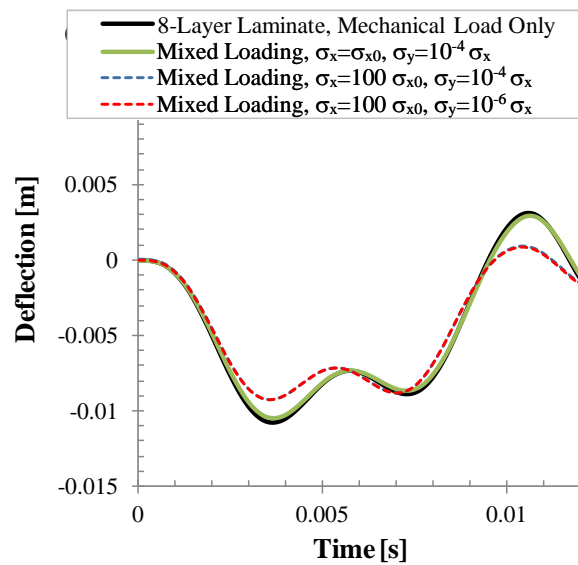
Figure 68. Deflection of the 8-layer square laminated plate: effect of increasing electrical conductivity
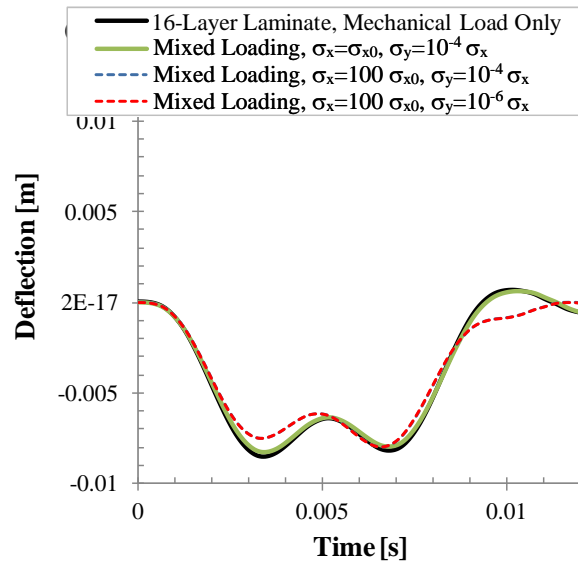
Figure 69. Deflection of the 16-layer square laminated plate: effect of increasing electrical conductivity

The distribution of the stress τ_{yy}/p_0 over the cross-section of the 8-layer laminated plate at the moment of time when the stress is maximum for the case when both mechanical ($p_0 = 1.0$ MPa , $\tau_p = 10$ ms) and pulsed electromagnetic ($J_0 = 10^6$ A/m^2 , $\tau_c = \tau_p = 10$ ms , $B_y^* = 1.0$ T) loads are applied, is shown in Figure 70. The mechanical load is in the form of a strip of impact-like pressure and the half-size of the contact zone is $b = h/10$.

As it can be seen, the four layers with the fiber orientations of $\theta = 90°$ bear the most portion of the induced stress τ_{yy} in a 8-layer cross-ply laminate. This is especially true for the layers farther from the middle plane of the plate. The magnitude of the stress caused in the laminated plate can be compared to the case when the plate is subjected to the mechanical load only, shown in the Fig. 71. Although the patterns of the stress distribution are similar, the magnitude of the stress τ_{yy} is reduced by about 20 percent when an effective electromagnetic load is concurrently applied with the mechanical load.
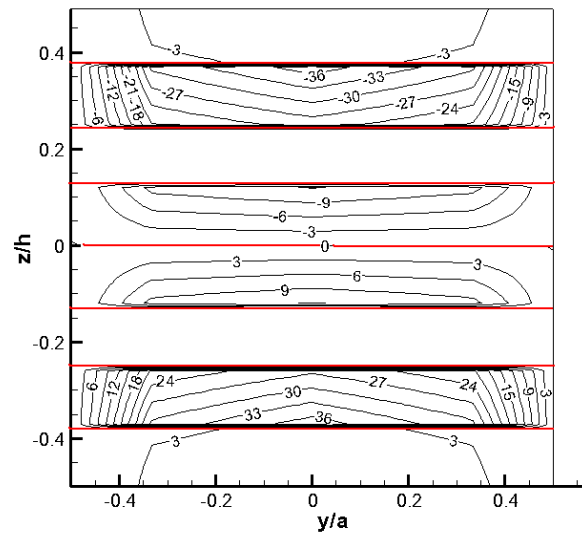
Figure 70. Contours of the stress τ_{yy}/p_0 at $t = 3.8\,\text{ms}$ in a 8-layer laminated plate subjected to both mechanical and electromagnetic loads ($p_0 = 1.0\,\text{MPa}$, $J_0 = 10^6\,\text{A/m}^2$, $\tau_c = \tau_p = 10\,\text{ms}$, $B_y^* = 1.0\,\text{T}$).
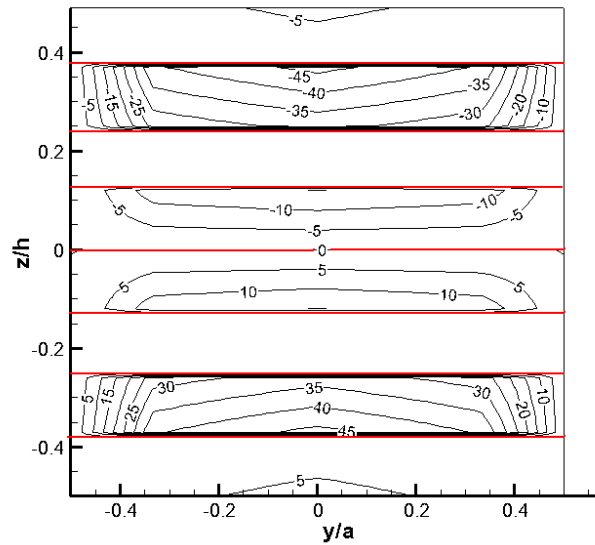
Figure 71. Contours of the stress τ_{yy}/p_0 at $t = 3.6\,\text{ms}$ in a 8-layer laminated plate subjected to the mechanical load only ($p_0 = 1.0\,\text{MPa}$, $\tau_p = 10\,\text{ms}$).

CHAPTER 7

CONCLUSIONS AND RECOMMENDATIONS

In this thesis, the effects of various electromagnetic loads on the dynamic mechanical response of electrically conductive anisotropic composite plates are studied. Both transversely isotropic single layer composite plates and laminated composite plates have been considered. The analysis is based on simultaneous solving of the system of nonlinear partial differential equations, including equations of motion and Maxwell's equations. Physics-based hypotheses for electro-magneto-mechanical coupling in transversely isotropic composite plates and dimension reduction solution procedures for the nonlinear system of the governing equations have been used to reduce the three-dimensional system to a two-dimensional (2D) form. A numerical solution procedure for the resulting 2D nonlinear mixed system of hyperbolic and parabolic partial differential equations has been developed, which consists of a sequential application of time and spatial integrations and quasilinearization. A new 2D model for the electrically conductive laminated composite with electromagnetic effects has been obtained. The model is based on the extension of the 2D model for transversely isotropic electrically conductive plates subjected to electromagnetic and mechanical loads.

The developed models and solution methodology are applied to the problem of the dynamic response of carbon fiber polymer matrix composite plates subjected to transverse impact load and in-plane electromagnetic load. The interacting effects of the electric current (DC, AC, and pulse), external magnetic field, and mechanical load are studied. The results show that current-induced heating can be significant with the highest temperature produced by the DC current. As it was expected, a pulsed electric current produced the lowest heating, which was also strictly limited to the regions immediately adjacent to the electric contact. The results also show that the dynamic mechanical

response of the composite to the combined impact and electromagnetic loads is highly dependent on the characteristics of the electromagnetic field (waveform, duration of application, intensity) with the pulsed electromagnetic fields being the most effective in reducing of vibrations caused by the application of the impact load. In particular, to achieve the maximum reduction in the plate deflection and stress, application of the mechanical load must be coordinated with application of the pulsed electric current, i.e., the maximum in the current should coincide with the maximum in the mechanical load. Moreover, an increase in the magnetic induction tends to reduce the amplitude of the vibrations of the plate with a trend towards a more rapid decay at the stronger magnetic fields. An increase in the electrical conductivity has a similar effect. As for the electric current density, an increase in the electric current density tends to decrease the amplitude of the plate vibrations. Moreover, the effect of the electric current density becomes more pronounced as the magnetic field intensity increases. Overall, this study demonstrates that concurrent application of a pulsed electromagnetic load can effectively mitigate the effects of the impact load in the electrically conductive composite plates.

For the future work, it is recommended to include thermal effects into 2D formulations for transversely isotropic and laminated plates. Although the FEM simulation conducted as a part of this thesis shows that the thermal analysis can be eliminated when the pulsed current is applied, the study of thermal effects on the mechanical response of the composite plate is important in the case of DC and AC electric currents.

APPENDIX

FINAL FORMULATION OF 1D SYSTEM OF EQUATOINS

The Newmark scheme in Eq. (4-1) can be rewritten in the form:

$$
\begin{aligned}
\frac{\partial^2 f_i(y,t+\Delta t)}{\partial t^2} &= \frac{1}{\beta(\Delta t)^2} f_i(y,t+\Delta t) + \xi_i(y,t) \\
\frac{\partial f_i(y,t+\Delta t)}{\partial t} &= \frac{\gamma}{\beta \Delta t} f(y,t+\Delta t) + \zeta_i(y,t)
\end{aligned}
\tag{A-1}
$$

where ξ_i and ζ_i are

$$
\begin{aligned}
\xi_i(y,t) &= \frac{-1}{\beta(\Delta t)^2} f_i(y,t) - \frac{1}{\beta}\left(\frac{1}{\Delta t}\frac{\partial f_i(y,t)}{\partial t} + \left(\frac{1}{2}-\beta\right)\frac{\partial^2 f_i(y,t)}{\partial t^2} \right), \\
\zeta_i(y,t) &= \frac{\partial f_i(y,t)}{\partial t} - \frac{\gamma}{\beta}\frac{\partial f(y,t)}{\partial t} - \frac{\gamma}{\beta \Delta t} f(y,t) + \left(-\frac{\Delta t}{2}\frac{\gamma}{\beta} \right)\frac{\partial^2 f_i(y,t)}{\partial t^2}.
\end{aligned}
\tag{A-2}
$$

Applying the Newmark scheme (A-1) together with the quasilinearization method (4-3) to the system (5-11) and (5-12), the final form of the system of governing partial differential equations for the long thin transversely isotropic plate (1D problem) subjected to the defined electromagnetic loads and time-varying pressure can be derived in the following form:

$$
\begin{aligned}
\frac{\partial g_1^{k+1}(y,t+\Delta t)}{\partial y} &= \frac{1}{hB_{22}} g_4^{k+1}(y,t+\Delta t), \\
\frac{\partial g_2^{k+1}(y,t+\Delta t)}{\partial y} &= g_3^{k+1}(y,t+\Delta t), \\
\frac{\partial g_3^{k+1}(y,t+\Delta t)}{\partial y} &= -\frac{12}{h^3 B_{22}} g_6^{k+1}(y,t+\Delta t),
\end{aligned}
\tag{A-3}
$$

$$\frac{\partial g_4^{k+1}(y,t+\Delta t)}{\partial y} = \left[\frac{\rho h}{\beta \Delta t^2} + \frac{\sigma_x h}{2\beta \Delta t}\left(g_8^k(y,t+\Delta t)\right)^2\right] g_1^{k+1}(y,t+\Delta t)$$

$$- \frac{\sigma_x h}{4\beta \Delta t} B_{y1} g_8^k(y,t+\Delta t) g_2^{k+1}(y,t+\Delta t) - \frac{(\varepsilon_x - \varepsilon_0)h}{4\beta \Delta t} B_{y1} g_7^k(y,t+\Delta t) g_3^{k+1}(y,t+\Delta t)$$

$$+ \frac{(\varepsilon_x - \varepsilon_0)h}{2\beta \Delta t \, B_{22}} g_7^k(y,t+\Delta t) g_8^k(y,t+\Delta t) g_4^{k+1}(y,t+\Delta t)$$

$$+ \left[\sigma_x h g_8^k(y,t+\Delta t) + \frac{(\varepsilon_x - \varepsilon_0)h}{B_{22}} g_8^k(y,t+\Delta t)\left(\frac{g_4^k(y,t+\Delta t)}{2\beta \Delta t} + \zeta_4(y,t)\right)\right.$$

$$\left. - \frac{(\varepsilon_x - \varepsilon_0)h}{2} B_{y1}\left(\frac{g_3^k(y,t+\Delta t)}{2\beta \Delta t} + \zeta_3(y,t)\right)\right] g_7^{k+1}(y,t+\Delta t)$$

$$+ \left[2\sigma_x h g_8^k(y,t+\Delta t)\left(\frac{g_1^k(y,t+\Delta t)}{2\beta \Delta t} + \zeta_1(y,t)\right) + \sigma_x h g_7^k(y,t+\Delta t)\right.$$

$$- \frac{\sigma_x h}{2} B_{y1}\left(\frac{g_2^k(y,t+\Delta t)}{2\beta \Delta t} + \zeta_2(y,t)\right) + h J_x^*(y,t+\Delta t)$$

$$\left. + \frac{(\varepsilon_x - \varepsilon_0)h}{B_{22}} g_7^k(y,t+\Delta t)\left(\frac{g_4^k(y,t+\Delta t)}{2\beta \Delta t} + \zeta_4(y,t)\right)\right] g_8^{k+1}(y,t+\Delta t)$$

$$+ \rho h \xi_1(y,t) - \sigma_x h g_7^k(y,t+\Delta t) g_8^k(y,t+\Delta t) - \sigma_x h \left(g_8^k(y,t+\Delta t)\right)^2 \zeta_1(y,t)$$

$$- \frac{\sigma_x h}{\beta \Delta t}\left(g_8^k(y,t+\Delta t)\right)^2 g_1^k(y,t+\Delta t) + \frac{\sigma_x h}{4\beta \Delta t} B_{y1} g_2^k(y,t+\Delta t) g_8^k(y,t+\Delta t)$$

$$- \frac{(\varepsilon_x - \varepsilon_0)h}{\beta \Delta t B_{22}} g_7^k(y,t+\Delta t) g_8^k(y,t+\Delta t) g_4^k(y,t+\Delta t)$$

$$- \frac{(\varepsilon_x - \varepsilon_0)h}{B_{22}} g_7^k(y,t+\Delta t) g_8^k(y,t+\Delta t)\zeta_4(y,t) + \frac{(\varepsilon_x - \varepsilon_0)h}{4\beta \Delta t} B_{y1} g_3^k(y,t+\Delta t) g_7^k(y,t+\Delta t),$$

$$\frac{\partial g_5^{k+1}(y,t+\Delta t)}{\partial y} = -\frac{\sigma_x h}{4\beta \Delta t} B_{y1} g_8^k(y,t+\Delta t) g_1^{k+1}(y,t+\Delta t)$$

$$+ \frac{h}{\beta \Delta t}\left[\frac{\rho}{\Delta t} + \frac{\sigma_x}{8}\left(B_{y1}^2 + \frac{1}{3} B_{y2}^2\right)\right] g_2^{k+1}(y,t+\Delta t)$$

$$+ \frac{h}{2\beta \Delta t}\left[\frac{\sigma_x h}{12} B_{y2} g_8^k(y,t+\Delta t) - (\varepsilon_x - \varepsilon_0) g_7^k(y,t+\Delta t) g_8^k(y,t+\Delta t)\right] g_3^{k+1}(y,t+\Delta t)$$

$$- h\left[\frac{\sigma_x}{2} B_{y1} + (\varepsilon_x - \varepsilon_0)\left(\frac{g_3^k(y,t+\Delta t)}{2\beta \Delta t} + \zeta_3(y,t)\right) g_8^k(y,t+\Delta t)\right] g_7^{k+1}(y,t+\Delta t)$$

$$-h\left[\left(\left(\varepsilon_x-\varepsilon_0\right)g_7^k(y,t+\Delta t)-\frac{\sigma_x h}{12}B_{y2}\right)\left(\frac{g_3^k(y,t+\Delta t)}{2\beta\Delta t}+\zeta_3(y,t)\right)\right.$$

$$+\frac{\sigma_x}{2}B_{y1}\left(\frac{g_1^k(y,t+\Delta t)}{2\beta\Delta t}+\zeta_1(y,t)\right)\Bigg]g_8^{k+1}(y,t+\Delta t)\Bigg]$$

$$+\rho h\xi_2(y,t)+p(y,t+\Delta t)+\frac{\sigma_x h}{4\beta\Delta t}B_{y1}g_1^k(y,t+\Delta t)g_8^k(y,t+\Delta t)$$

$$+\frac{\sigma_x h}{4}\left(B_{y1}^2+\frac{1}{3}B_{y2}^2\right)\zeta_2(y,t)-\frac{\sigma_x h^2}{24\beta\Delta t}B_{y2}g_3^k(y,t+\Delta t)g_8^k(y,t+\Delta t)$$

$$+\frac{\left(\varepsilon_x-\varepsilon_0\right)h}{\beta\Delta t}\left(+\zeta_3(y,t)\right)g_3^k(y,t+\Delta t)g_7^k(y,t+\Delta t)g_8^k(y,t+\Delta t)$$

$$+\left(\varepsilon_x-\varepsilon_0\right)h\,g_7^k(y,t+\Delta t)g_8^k(y,t+\Delta t)\zeta_3(y,t)-\frac{h}{2}B_{y1}J_x^*(t+\Delta t),$$

$$\frac{\partial g_6^{k+1}(y,t+\Delta t)}{\partial y}=-\frac{\sigma_x h^2}{24\beta\Delta t}B_{y2}g_8^{k+1}(y,t+\Delta t)g_2^{k+1}(y,t+\Delta t)$$

$$-\frac{h^2}{24\beta\Delta t}\left[\frac{2\rho h}{\Delta t}+\left(\varepsilon_x-\varepsilon_0\right)B_{y2}g_7^k(y,t+\Delta t)+\sigma_x h\left(g_8^k(y,t+\Delta t)\right)^2\right]g_3^{k+1}(y,t+\Delta t)$$

$$+\frac{\left(\varepsilon_x-\varepsilon_0\right)}{2\beta\Delta t B_{22}}g_7^k(y,t+\Delta t)g_8^k(y,t+\Delta t)g_6^{k+1}(y,t+\Delta t)$$

$$+g_5^{k+1}(y,t+\Delta t)+\left(\varepsilon_x-\varepsilon_0\right)\left[-\frac{h^2}{12}B_{y2}\left(\frac{g_3^k(y,t+\Delta t)}{2\beta\Delta t}+\zeta_3(y,t)\right)\right.$$

$$+\frac{1}{B_{22}}g_8^k(y,t+\Delta t)\left(\frac{g_6^k(y,t+\Delta t)}{2\beta\Delta t}+\zeta_6(y,t)\right)\Bigg]g_7^{k+1}(y,t+\Delta t)$$

$$+\left[-\frac{\sigma_x h^2}{12}B_{y2}\left(\frac{g_2^k(y,t+\Delta t)}{2\beta\Delta t}+\zeta_2(y,t)\right)-\frac{\sigma_x h^3}{6}g_8^k(y,t+\Delta t)\left(\frac{g_3^k(y,t+\Delta t)}{2\beta\Delta t}+\zeta_3(y,t)\right)\right.$$

$$+\frac{\left(\varepsilon_x-\varepsilon_0\right)}{B_{22}}g_7^k(y,t+\Delta t)\left(\frac{g_6^k(y,t+\Delta t)}{2\beta\Delta t}+\zeta_6(y,t)\right)\Bigg]g_8^{k+1}(y,t+\Delta t)$$

$$-\frac{\rho h^3}{12}\xi_3(y,t)+\frac{\sigma_x h^3}{12}\left(g_8^k(y,t+\Delta t)\right)^2\left(\frac{g_3^k(y,t+\Delta t)}{\beta\Delta t}+\zeta_3(y,t)\right)$$

$$+ \frac{\sigma_x h^2}{24\beta\Delta t} B_{y2} g_2^k(y, t+\Delta t) g_8^k(y, t+\Delta t) + \frac{(\varepsilon_x - \varepsilon_0) h^2}{24\beta\Delta t} B_{y2} g_3^k(y, t+\Delta t) g_7^k(y, t+\Delta t)$$

$$- \frac{(\varepsilon_x - \varepsilon_0)}{B_{22}} g_7^k(y, t+\Delta t) g_8^k(y, t+\Delta t) \left(\frac{g_6^k(y, t+\Delta t)}{\beta\Delta t} + \zeta_6(y, t) \right),$$

$$\frac{\partial g_7^{k+1}(y, t+\Delta t)}{\partial y} = \frac{1}{2\beta\Delta t} g_8^{k+1}(y, t+\Delta t) + \zeta_8(y, t),$$

$$\frac{\partial g_8^{k+1}(y, t+\Delta t)}{\partial y} = \frac{\sigma_x \mu}{2\beta\Delta t} g_8^k(y, t+\Delta t) g_1^{k+1}(y, t+\Delta t) - \frac{\sigma_x \mu}{4\beta\Delta t} B_{y1} g_2^{k+1}(y, t+\Delta t)$$

$$+ \sigma_x \mu \, g_7^{k+1}(y, t+\Delta t) + \sigma_x \mu \left(\frac{g_1^k(y, t+\Delta t)}{2\beta\Delta t} + \zeta_1(y, t) \right) g_8^{k+1}(y, t+\Delta t)$$

$$- \frac{\sigma_x \mu}{2\beta\Delta t} g_1^k(y, t+\Delta t) g_8^k(y, t+\Delta t) - \frac{\sigma_x \mu}{2} B_{y1} \zeta_2(y, t) + \frac{B_{y1}}{h}.$$

REFERENCES

1. Telitchev, I.Y.; Sierakowski, R.L.; Zhupanska, O.I. Low Velocity Impact Testing of Electrified Composites; Part I- Application of An Electric Current. *Experimental Techniques*, **2008**, *32*, 35-38.

2. Telitchev, I.Y.; Sierakowski, R.L.; Zhupanska, O.I. Low Velocity Impact Testing of Electrified Composites; Part II- Experimental Setup and Preliminary Results. *Experimental Techniques*, **2008**, *32(3)*, 53-57.

3. Sierakowski, R.L.; Telitchev, I.Y.; Zhupanska, O.I. On the Impact Response of Electrified Carbon Fiber Polymer Matrix Composites: Effects of Electric Current Intensity and Duration. *Compos. Sci. Tech.*, **2008**, *68(3-4)*, 639-649.

4. Gibson, R.F. A Review of Recent Research on Mechanics of Multifunctional Composite Materials and Structures. *Composite Structures*, **2010**, *92(12)*, 2793-2810.

5. Koratkar, N.A.; Wei, B.Q.; Ajayan, P.M. Multifunctional Structural Reinforcement Featuring Carbon Nanotube Films. *Composites Science and Technology*, **2003**, *63(11)*, 1525-1531.

6. Iijima, S. Helical Microtubules of Graphitic Carbon. *Nature*, **1991**, *354(6348)*, 56-58.

7. Bagchi, A.; Nomura, S. On the Effective Thermal Conductivity of Carbon Nanotube Reinforced Polymer Composites. *Composites Science and Technology*, **2006**, *66(11-12)*, 1703-1712.

8. Sandler, J.; Shaffer, M.S.P.; Prasse, T.; Bauhofer, W.; Schulte, K.; Windle, A.H. Development of a Dispersion Process for Carbon Nanotubes in an Epoxy Matrix and the Resulting Electrical Properties. *Polymer*, **1999**, *40(21)*, 5967-5971.

9. Biercuk, M.J.; Llaguno, M.C.; Radosavljevic, M.; Hyun, J.K.; Johnson, A.T.; Fischer, J.E. Carbon Nanotube Composites for Thermal Management. *Applied Physics Letters Volume*, 2002, 80(15), 2767-2769.

10. Dufresne, A.; Paillet, M.; Putaux, J.L.; Canet, R.; Carmona, F.; Delhaes, P.; Cui, S. Processing and Characterization of Carbon Nanotube/Poly(Styrene-Co-Butyl Acrylate) Nanocomposites. *Journal of Materials Science*, **2002**, *37(18)*, 3915-3923.

11. Chang, T.E.; Kisliuk, A.; Rhodes, S.M.; Brittain, W.J.; Sokolov, A.P. Conductivity and Mechanical Properties of Well-Dispersed Single-Wall Carbon Nanotube/Polystyrene Composite. *Polymer*, **2006**, *47(22)*, 7740-7746.

12. Thostenson, E.T.; Ren, Z.F.; Chou, T.W. Advances in the Science and Technology of Carbon Nanotubes and their Composites: A Review. *Composites Science and Technology,* **2001**, *61(13)*, 1899-1912.

13. Tang, W.Z.; Santare, M.H.; Advani, S.G. Melt Processing and Mechanical Property Characterization of Multi-Walled Carbon Nanotube/High Density Polyethylene (MWNT/HDPE) Composite Films. *Carbon*, **2003**, *41(14)*, 2779-2785.

14. Goze, C.; Vaccarini, L.; Henrard, L.; Bernier, P.; Hemandez, E.; Rubio, A. Elastic and Mechanical Properties of Carbon Nanotubes. *Synthetic Metals*, **1999**, *103(1-3)*, 2500-2501.

15. Wong, E.W.; Sheehan, P.E.; Lieber, C.M. Nanobeam Mechanics: Elasticity, Strength, and Toughness of Nanorods and Nanotubes. *Science*, **1997**, *277(5334)*, 1971-1975.

16. Allaoui, A.; Bai, S.; Cheng, H.M.; Bai, J.B. Mechanical and Electrical Properties of a MWNT/Epoxy Composite. *Composites Science and Technology*, **2002**, *62(15)*, 1993-1998.

17. Yao, Z.H.; Zhu, C.C.; Cheng, M.; Liu, J. Mechanical Properties of Carbon Nanotube by Molecular Dynamics Simulation. *Computational Materials Science*, **2001**, *22(3-4)*, 180-184.

18. Yu, M.F.; Files, B.S.; Arepalli, S.; Ruoff, R.S. Tensile Loading of Ropes of Single Wall Carbon Nanotubes and their Mechanical Properties. *Physical Review Letters*, **2000**, *84(24)*, 5552-5555.

19. Kim, P.; Shi, L.; Majumdar, A.; McEuen, P.L. Thermal Transport Measurements of Individual Multiwalled Nanotubes. *Physical Review Letters*, **2001**, *87(21)*, Article Number: 215502.

20. Berber, S.; Kwon, Y.K.; Tomanek, D. Unusually High Thermal Conductivity of Carbon Nanotubes. *Physical Review Letters*, **2000**, *84(20)*, 4613-4616.

21. Appenzeller, J.; Martel, R.; Derycke, V.; Radosavljević, M.; Wind, S.; Neumayer, D.; Avouris, Ph. Carbon Nanotubes as Potential Building Blocks for Future Nanoelectronics. *Microelectronic Engineering*, **2002**, *64(1-4)*, 391-397.

22. Lourie, O.; Wagner, H.D. Evidence of Stress Transfer and Formation of Fracture Clusters in Carbon Nanotube-Based Composites. *Composites Science and Technology*, **1999**, *59(6)*, 975-977.

23. Kim, Y.A.; Hayashi, T.; Endo, M.; Gotoh, Y.; Wada, N.; Seiyama, J. Fabrication of Aligned Carbon Nanotube-Filled Rubber Composite, *Scripta Materialia*, **2006**, *54(1)*, 31-35.

24. Choi, E.S.; Brooks, J.S.; Eaton DL; Al-Haik, M.S.; Hussaini, M.Y.; Garmestani, H.; Li, D.; Dahmen, K. Enhancement of Thermal and Electrical Properties of Carbon Nanotube Polymer Composites by Magnetic Field Processing. *Journal of Applied Physics*, **2003**, *94(9)*, 6034-6039.

25. Zhao, Z.G.; Ci, L.J.; Cheng, H.M.; Bai, J.B. The Growth of Multi-Walled Carbon Nanotubes with Different Morphologies on Carbon Fibers. *Carbon*, **2005**, *43(3)*, 663-665.

26. Zhao, J.; Liu, L.; Guo, Q.; Shi, J.; Zhai, G.; Song, J.; Liu, Zh. Growth of Carbon Nanotubes on the Surface of Carbon Fibers. *Carbon*, **2008**, *46(2)*, 380-383.

27. Zhu, S.; Su, C.H.; Lehoczky, S.L.; Muntele, I., Ila, D. Carbon Nanotube Growth on Carbon Fibers. *Diamond and Related Materials*, **2003**, *12(10-11)*, 1825-1828.

28. Yen, J.H.; Leu, I.C.; Lin, C.C.; Hon, M.H. Effect of Catalyst Pretreatment on the Growth of Carbon Nanotubes. Carbon Fibers. *Diamond and Related Materials*, **2004**, *13(4-8)*, 1237-1241.

29. Li, W.Z.; Wang, D.Z.; Yang, S.X.; Wen J.G.; Ren, Z.F. Controlled Growth of Carbon Nanotubes on Graphite Foil by Chemical Vapor Deposition, *Chemical Physics Letters*, **2001**, *335(3-4)*, 141-149.

30. De Riccardis, M.F.; Carbone, D.; Makris, T.D.; Giorgi, R.; Lisi, N.; Salernitano, E. Anchorage of Carbon Nanotubes Grown on Carbon Fibres. *Carbon*, **2006**, *44(4)*, 671-674.

31. Mathur, R.B.; Chatterjee, S.; Singh, B.P. Growth of Carbon Nanotubes on Carbon Fibre Substrates to Produce Hybrid/Phenolic Composites with Improved Mechanical Properties. *Composites Science and Technology*, **2008**, *68(7-8)*, 1608-1615.

32. Thostenson, E.T.; Li, W.Z.; Wang, D.Z.; Ren, Z.F.; Chou, T.W. Carbon Nanotube/Carbon Fiber Hybrid Multiscale Composites. *Journal of Applied Physics*, **2002**, *91(9)*, 6034-6037.

33. Vlasveld, D.P.N.; Bersee, H.E.N.; Picken, S.J. Nanocomposite Matrix for Increased Fibre Composite Strength. *Polymer*, **2005**, *46(23)*, 10269-10278.

34. O'Brien, D.J.; Baechle, D.M.; Wetzel. E.D. Multifunctional Structural Composite Capacitors for U.S. Army Applications. SAMPE '06 Fall Technical Conference, Nov. 6-9, 2006.

35. Cho, S.; Lee, J.; Hyun, J.; Paik, K. Study on Epoxy/BaTiO3 Composite Embedded Capacitor Films (ECFs) for Organic Substrate Applications. *Materials Science and Engineering B*, **2004**, *110(3)*, 233-239.

36. Xie, S.; Zhu, B.; Xu, Z.; Xu, Y. Preparation and Properties of Polyimide/LTNO Composite Films with High Dielectric Constant. *Materials Letters*, **2005**, *59(19-20)*, 2403-2407.

37. Kuo, D.; Chang, C.; Su, T.; Wang, W.; Lin, B.; Dielectric Properties of Three Ceramic/Epoxy Composites. Materials *Chemistry and Physics*, **2004**, *85(1)*, 201-206.

38. Xie, S.; Zhu, B.; Wei, X.; Xu, Z.; Xu, Y. Polyimide/BaTiO3 Composites with Controllable Dielectric Properties. *Composites Part A: Applied Science and Manufacturing*, **2005**, *36(8)*, 1152-1157.

39. Chao, F.; Liang, G.; Kong, W.; Zhang, Z.; Wang, J.; Dielectric Properties of Polymer/Ceramic Composites Based on Thermosetting Polymers. *Polymer Bulletin*, **2008**, *60(1)*, 129-136.

40. Li, J.; Ma, P.Ch.; Chow, W.S.; To, C.K.; Tang, B.Z.; Kim, J.K. Correlations between Percolation Threshold, Dispersion State, and Aspect Ratio of Carbon Nanotubes. *Advanced Functional Materials*, **2007**, *17(16)*, 3207-3215.

41. Kirkpatr, S. Percolation and Conduction. *Reviews Of Modern Physics*, **1973**, *45(4)*, 574-588.

42. Celzard, A.; McRae, E.; Deleuze, C.; Dufort, M.; Furdin, G.; Marêché, J.f. Critical Concentration in Percolating Systems Containing a High-Aspect-Ratio Filler. *Physical Review B*, **1996**, *53(10)*, 6209-6214.

43. Martin, C.A.; Sandler, J.K.W.; Shaffer, M.S.P.; Schwarz, M.K.; Bauhofer, W.; Schulte, K.; Windle, A.H. Formation of Percolating Networks in Multi-Wall Carbon-Nanotube-Epoxy Composites. *Composites Science and Technology*, **2004**, *64(15)*, 2309-2316.

44. Skakalova, V.; Dettlaff-Weglikowska, U.; Roth, S. Electrical and Mechanical Properties of Nanocomposites of Single Wall Carbon Nanotubes with PMMA. *Synthetic Metals*, **2005**, *152(1-3)*, 349-352.

45. Tong, X.C. *Advanced Materials and Design for Electromagnetic Interference Shielding*, Taylor & Francis Group: Boca Raton, FL, 2009.

46. Celozzi, S.; Areneo, R.; Lovat, G.; *Electromagnetic Shielding*, John Wiley & Sons, Inc.: Hoboken, NJ, 2008.

47. Lisunova, M.O.; Mamunya, Y.P.; Lebovka, N.I.; Melezhyk, A.V. Percolation Behaviour of Ultrahigh Molecular Weight Polyethylene/Multi-Walled Carbon Nanotubes Composites. *European Polymer Journal*, **2007**, *43(3)*, 949-958.

48. Bose, S.; DeMasiMarcin, J. Thermal Barrier Coating Experience in Gas Turbine engines at Pratt & Whitney. *Journal of Thermal Spray Technology*, **1997**, *6(1)*, 99-104.

49. Drawin, S. Atmospheric Reentry-Degradation of Thermal Protection Shield Materials. *Annales De Chimie-Science Des Materiaux*, **1992**, *17(7-8)*, 455-469.

50. Cahill, D.G.; Goodson, K.; Majumdar, A. Thermometry and Thermal Transport in Micro/Nanoscale Solid-State Devices and Structures. *Journal of Heat Transfer-Transactions of The ASME*, **2002**, *124(2)*, 223-241.

51. Evans, A.G.; Mumm, D.R.; Hutchinson, J.W.; Meier, G.H.; Pettit, F.S. Mechanisms Controlling the Durability of Thermal Barrier Coatings. *Progress in Materials Science*, **2001**, *46(5)*, 505-553.

52. Sommers, A.; Wang, Q.; Han X.; T'Joen, C.; Park, Y.; Jacobi, A. Ceramics and Ceramic Matrix Composites for Heat Exchangers in Advanced Thermal Systems-A Review. *Applied Thermal Engineering*, **2010**, *30(11-12)*, 1277-1291.

53. Wu, G.Z.; Nishida, K.; Takagi, K.; Sano, H.; Yui, H. Rubber as Additives to Lower Thermal Expansion Coefficient Of Plastics: 1. Morphology and Properties. *Polymer*, **2004**, *45(9)*,3085-3090.

54. Choi, T.Y.; Poulikakos, D.; Tharian, J.; Sennhauser, U. Measurement of Thermal Conductivity of Individual Multiwalled Carbon Nanotubes by the 3-Omega Method. *Applied Physics Letters*, **2005**, *87(1)*, Article Number: 013108.

55. Putnam, S.A.; Cahill, D.G.; Ash, B.J.; Schadler, L.S. High-Precision Thermal Conductivity Measurements as a Probe of Polymer/Nanoparticle Interfaces. *Journal Of Applied Physics*, **2003**, *94(10)*, 6785-6788.

56. Che, J.W.; Cagin, T.; Goddard, W.A. Thermal Conductivity of Carbon Nanotubes. *Nanotechnology*, **2000**, *11(2)*, 65-69.

57. Kim, Y.A.; Kamio, S.; Tajiri, T.; Hayashi, T.; Song, S.M.; Endo, M.; Terrones, M.; Dresselhaus, M.S. Enhanced Thermal Conductivity of Carbon Fiber/Phenolic Resin Composites by the Introduction of Carbon Nanotubes. *Applied Physics Letters*, **2007**, *90(9)*, Article Number: 093125.

58. Ganguli S.; Roy A.K.; Anderson D.P. Improved Thermal Conductivity for Chemically Functionalized Exfoliated Graphite/Epoxy Composites. *Carbon*, **2008**, *46(5)*, 806-817.

59. Kessler, S.S.; Spearing, S.M.; Soutis, C. Damage Detection in Composite Materials Using Lamb Wave Methods. *Smart Materials & Structures*, **2002**, *11(2)*, 269-278.

60. Farrar, Ch.R.; Worden K. An Introduction to Structural Health Monitoring. *Philosophical Transactions of The Royal Society A-Mathematical Physical and Engineering Sciences*, **2007**, *365(1851)*, 303-315.

61. Capezzuto, F.; Ciampa, F.; Carotenuto, G.; Meo, M.; Milella, E.; Nicolais, F. A Smart Multifunctional Polymer Nanocomposites Layer for the Estimation of Low-Velocity Impact Damage in Composite Structures. *Composite Structures*, **2010**, *92(8)*, 1913-1919.

62. Housner, G.W.; Bergman, L.A.; Caughey, T.K.; Chassiakos, G.; Claus, R.O.; Masri, S.F.; Skelton, R.E.; Soong, T.T.; Spencer, B.F.; Yao, J.T.P. Structural Control: Past, Present, and Future. *Journal of Engineering Mechanics-ASCE*, **1997**, *123(9)*, 897-971.

63. Truesdell, C.; Toupin, R. The Classical Field Theories. In Handbuch der Physik, S. Flugge (Ed.), Springer: Berlin, 1960, Vol. III/1; p 226-793.

64. Kaliski, S.; Nowacki, W. Excitation of Mechanical-Electromagnetic Waves Induced by a Thermal Shock. *Bull. de l'Academie Polonaise des Sci.*, **1962**, *10*, 25–33.

65. Kaliski, S.; Nowacki, W. Combined Elastic and Electromagnetic Waves Produced by Thermal Shock in the Case of a Medium of Finite Electric Conductivity. *Bull. de l'Academie Polonaise des Sci.*, **1962**, *10*, 159–169.

66. Nowacki, W. Two-Dimensional Problem of Magnetothermoelasticity. I. *Bull. de l'Academie Polonaise des Sci.*, **1962**, *10*, 485–493.

67. Nowacki, W. The Plane Problem of Magnetothermoelasticity. II. *Bull. de l'Academie Polonaise des Sci.*, **1963**, *11*,1–8.

68. Brown, W.F. *Magnetoelastic Interactions*, Springer: Berlin, 1966.

69. Ambartsumyan, S.A.; Belubekyan, M.B.; Bagdasaryan, G.E.; *Magnetoelasticity of Thin Shells and Plates*, Nauka: Moscow, 1977.

70. Eringen, A.C.; Maugin, G.A.; *Electrodynamics of Continua I: Foundations and Solid Media*, Springer-Verlag: New York, 1989.

71. Eringen, A.C.; Maugin, G.A.; *Electrodynamics of Continua II: Fluids and Complex Media*, Springer-Verlag: New York, 1990.

72. Yang, J.S.; Maugin, G.A.; *Mechanics of Electromagnetic Materials and Structures*, IOS Press: Amsterdam, 2000.

73. Brigdanov, I.A.; Dorfmann, A. Mathematical Modeling Of Magneto-Sensitive Elastomers. *Int. J. Solid. Struct.*, **2003**, *40*, 4659–4674.

74. Dorfmann, A.; Ogden, R.W. Nonlinear Magnetoelastic Deformations of Elastomers. *Acta Mech.*, **2004**, *167*, 13–28.

75. Bustamante, R.; Dorfmann, A.; Ogden, R.W.; Universal Relation in Isotropic Nonlinear Magnetoelasticity. *Q. J. Mech. Appl. Math.*, **2006**, *59*, 435-450.

76. Mason, W.P. *Pizoelectric Crystals and Their Applications in Ultrasonics*, Van Nostrand: Princeton, New Jersey, 1950.

77. Barfoot, J.; Taylor, G. *Polar Dielectrics and Their Applications*, Macmillan Press: New York, 1979.

78. Mason, W.P. Piezoelectricity, its History and Applications. *J. Acoust. Soc. Am.*, **1981**, *70*, 1561–1566.

79. Uchino, K. *PZ Actuators and Ultrasonic Motors*, Kluwer Academic: Dordrecht, 1996.

80. Chang, S.H.; Tung, Y.C.; Electro-Elastic Characteristics of Asymmetric Rectangular Piezoelectric Laminate. *IEEE Trans. Ultrason. Ferroelectrics Freq. Contr.*, **1999**, *46*, 950–960.

81. Gopinathan, S.V.; Varadan, V.V.; Varadan, V.K. A Review and Critique of Theories for Piezoelectric Laminates. *Smart Mater. Struct.*, **2000**, *9*, 24–48.

82. Tauchert, T.R.; Ashida, F.; Noda, N.; Adali, S.; Verijentko, V. Developments in Thermopiezoelasticity with Relevance to Smart Composite Structures. *Compos. Struct.*, **2000**, *48*, 31–38.

83. Benveniste, Y. On the Micromechanics of Fibrous Piezoelectric Composites. *Mech. Mater.*, **1994**, *18*, 183–193.

84. Li, J.Y.; Dunn, M.L. Micromechanics of Magnetoelectroelastic Composite Materials: Average Fields and Effective Behavior. J. Intell. *Mater. Syst. Struct.*, **1998**, *9*, 404–416.

85. Chen, Z.R.; Yu, S.W.; Meng, L.; Lin, Y.; Effective Properties of Layered Magneto-Electro-Elastic Composites. *Compos. Struct.*, **2002**, *57*, 177–182.

86. Parkus, H. Magneto-Thermoelasticity, In *Lecture Notes;* CISM, Udine; 2nd edn ed.; Springer: Vienna, 1972.

87. Moon, F.C. *Magnetosolid Mechanics*, Wiley: New York, 1984.

88. Maugin, G.A. *Continuum Mechanics of Electromagnetic Solids*, North-Holland: Amsterdam, 1988.

89. Ulitko, A.F.; Molchenko, L.V.; Kovalchuk, V.F. *Magnetoelasticity of Dynamic Loading*, Lybid: Kiev, 1994.

90. Green, A.E.; Naghdi, P.M. Electromagnetic Effects in the Theory of Shells and Plates. *Philos. Trans. R. Soc. A Phys. Math. Eng. Sci.*, **1983**, *309*, 559–610.

91. Guenneau, S.; Movchan, A.; Poulton, C.; Nicolet, A. Coupling Between Electromagnetic and Mechanical Vibrations of Thin-Walled Structures. *Q. J. Mech. Appl. Math.*, **2004**, *57*, 407–428.

92. Hasanyan, D.J.; Piliposyan, G.T. Modelling and Stability of Magnetosoft Ferromagnetic Plates in a Magnetic Field. *Proc. R. Soc. A*, **2001**, *457*, 2063–2077.

93. Rudnicki, M. Eigenvalue Solutions for Free Motion of Electroconductive Plate in Magnetic Field. *Int. J. Eng. Sci.*, **2002**, *40*, 93–107.

94. Hasanyan, D.; Librescu, L.; Ambur, D.R. A Few Results on the Foundation of the Theory and Behavior of Nonlinear Magnetoelastic Plates Carrying an Electric Current. *Int. J. Eng. Sci.*, **2004**, *42*, 1547–1572.

95. Qin, Z.; Librescu, L.; Hasanyan, D.; Ambur, D.R. Magnetoelastic Modeling of Circular Cylindrical Shells Immersed in a Magnetic Field. Part I: Magnetoelastic Loads Considering Finite Dimensional Effects. *Int. J. Eng. Sci.*, **2003**, *41*, 2005–2022.

96. Librescu, L.; Hasanyan, D.; Ambur, D.R. Electromagnetically Conducting Elastic Plates in a Magnetic Field: Modeling and Dynamic Implications. *Int. J. Non Lin. Mech.*, **2004**, *39*, 723–739.

97. Dai, H.L.; Wang, X. Magnetoelastodynamic Stress and Perturbation of Magnetic Field Vector in an Orthotropic Laminated Hollow Cylinder. *Int. J. Eng. Sci.*, **2006**, *44*, 365–378.

98. Librescu, L.; Hasanyan, D.; Qin, Z.; Ambur, D.R. Nonlinear Magnetothermoelasticity of Anisotropic Plates Immersed In A Magnetic Field. *J. Therm. Stress.*, **2003**, *26*, 1277–1304.

99. Hasanyan, D.; Librescu, L.; Qin, Zh.; Ambur, D.R. Magneto-Thermo-Elastokinetics of Geometrically Nonlinear Laminated Composite Plates. Part 1: Foundation of Theory. *J. Sound Vib.*, **2005**, *287(1-2)*, 153-175.

100. Qin, Z.; Hasanyan, D.; Librescu, L.; Ambur, D.R. Magneto-Thermo-Elastokinetics of Geometrically Nonlinear Laminated Composite Plates. Part 2: Vibration and Wave Propagation. *J. Sound Vib.*, **2005**, *287(1-2)*, 177–201.

101. Zhupanska, O.I.; Sierakowski, R.L. Mechanical response of composites in the presence of an electromagnetic field. In: *Proceeding of 46th AIAA/ASME/ASCE/AHS/ASC Structures, Structural Dynamics & Materials Conference*, Paper # AIAA 2005-1949, 2005.

102. Zhupanska, O.I.; Sierakowski, R.L. Effects of an Electromagnetic Field on the Mechanical Response of Composites. *J. Compos. Mater.*, **2007**, *41*, 633–652.

103. Zhupanska, O.I.; Sierakowski, R.L. Electro-Thermo-Mechanical Coupling in Carbon Fiber Polymer Matrix Composites. *Acta Mech.*, **2011**, *218*, 219-232.

104. Panofsky, W.K.H.; Phillips, M. *Classical Electricity and Magnetism*, Addison-Wesley: New York, 1962.

105. Sedov, L.I. *A Course in Continuum Mechanics*, Vol. 1; Wolters-Noordhoff: Groningen, 1971.

106. Reddy, J.N. *Theory and Analysis of Elastic Plates*, Taylor & Francis: Philadelphia, PA, 1999.

107. Ambartsumyan, S.A. *Theory of Anisotropic Plates*, Technomic: Stamford, 1970.

108. Szilard, R. *Theories and Applications of Plate Analysis: Classical, Numerical, and Engineering Methods*, John Wiley & Sons: New York, 2004.

109. Incropera, F.P.; DeWitt D.P. *Fundamentals of Heat and Mass Transfer*, John Wiley & Sons: New York, 2007.

110. Newmark, N.M. A Method of Computation for Structural Dynamics. *J. Eng. Mech. Div. Proc. ASCE*, **1959**, *85*, 67-97.

111. Bellman, R.F.; Kalaba, R.E. *Quasilinearization and Nonlinear Boundary-Value Problems*, American Elsevier Publishing Company, Inc.: New York, 1969.

112. Kubíček, M.; Hlaváček, V. *Numerical Solution of Nonlinear Boundary Value Problems with Applications*, Prentice-Hall, Inc.: Englewood Cliffs, New Jersey, 1983.

113. Atkinson, K.E.; Han, W.; Stewart, D.E. *Numerical Solutions of Ordinary Differential Equations*, John Wiley & Sons, Inc: Hoboken, New Jersey, 2009.

114. Roberts, S.M.; Shipman, J.S. *Two-Point Boundary Value Problems: Shooting Methods*, American Elsevier Publishing Company, Inc.: New York, 1972.

115. Kincaid, D.R.; Cheney, E.W. *Numerical Analysis: Mathematics of Scientific Computing*, 3rd ed.; American Mathematical Society: Providence, Rhode Island, 2002.

116. Scott, M.R.; Watts, H.A. Computational Solution of Linear Two-Point Boundary Value Problem via Orthonormalization. *Siam J. Numer. Anal.*, **1977**, *14*, 40-70.

117. Godunov, S.K. On the Numerical Solution of Boundary Value Problems for System of Linear Ordinary Differential Equations. *Uspekhi Mat. Nauk*, **1961**, *16*, 171-174.

118. Conte, S.D. The Numerical Solution of Linear Boundary Value Problems. *SIAM Rev.*, **1966**, *8*, 309-321.

119. Mol'chenko, L.V.; Loos, I.I. Magnetoelastic Nonlinear Deformation of a Conical Shell of Variable Stiffness. *Int. Appl. Mech.*, **1999**, *35*, 1111-1116.

120. Householder, A.S. *The Numerical Treatment of a Single Nonlinear Equation*, McGraw-Hill: New York, 1970.

121. Higham, N.J. *Accuracy and Stability of Numerical Algorithms*, 2nd ed.; Society for Industrial and Applied Mathematics: Philadelphia, 2002.

122. Trefethen, L.N.; Bau III, D. *Numerical Linear Algebra*, Society for Industrial and Applied Mathematics: Philadelphia, 1997.

123. Rice, J.R. Experiments on Gram-Schmidt Orthogonalization. *Math. Comp.*, **1966**, *20*, 325-328.

124. Giraud, L.; Langou, J.; Rozloznik, M. The Loss of Orthogonality in the Gram-Schmidt Orthogonalization Process. *Comput. Math. Appl.*, **2005**, *50*, 1069-1075.

125. Ruhe, A. Numerical Aspects of Gram-Schmidt Orthogonalization of Vectors. *Lin. Algebra Appl.*, **1983**, *52-3*, 591-601.

126. Meyer, G.H. Continuous Orthonormalization for Boundary-Value-Problems. *J. Comput. Phys.,* **1986**, *62*, 248-262.

127. van Loon, P.M.; Mattheij, R.M.M. Stable Continuous Orthonormalisation Techniques For Linear Boundary Value Problems. *J. Austral. Math. Soc. Ser. B*, **1988**, *29*, 282-295.

128. Sadiku M.N.O.; Obiozor C.N. A Simple Introduction to the Method of Lines. *International Journal of Electrical Engineering Education*, **2000**, *37(3)*, 282-296.

129. Zafarulla, A. Application of Method of Lines to Parabolic Partial Differential Equations with Error Estimates. *Journal of The ACM*, **1970**, *17(2)*, 294-302.

130. Jones D. J.; South Jr., J.C.; Klunker E.B. On the Numerical Solution of Elliptic Partial Differential Equations by the Method of Lines. *J. Comput. Phys.*, **1972**, *9*, 496–527.

131. Chen, H.H.; Yeh, S.F.; Chou ,Y.H.; Hsieh, R.C. Finite-Element Method-Method of Lines Approach for the Analysis of Three-Dimensional Electromagnetic Cavities. *IET Microwaves Antennas & Propagation*, **2007**, *1(3)*, 751-756.

132. Schiesser, W.E.; Griffiths, G.W. *A Compendium of Partial Differential Equation Models: Method of Lines Analysis with MATLAB*, Cambridge University Press: New York, USA, 2009.

133. Ramachandran, P.A. Method of Lines with Boundary Elements for 1-D Transient Diffusion-Reaction Problems. *Numerical Methods for Partial Differential Equations*, **2006**, *22(4)*, 831-846.

134. Saucez, P.; Schiesser, W.E.; Vande Wouwer, A. Upwinding in the Method of Lines. *Mathematics and Computers in Simulation*, **2001**, *56(2)*, 171-185.

135. Johnson, K.L. *Contact Mechanics*, Cambridge University Press: Cambridge, 1985.

136. Ogasawara, T.; Hirano, Y.; Yoshimura, A., Coupled Thermal-electrical Analysis for Carbon Fiber/Epoxy Composites Exposed to Simulated Lightning Current. *Compos. Appl. Sci. Manuf.*, **2010**, *41(8)*, 973-981.

137. Zantout, A.E.; Zhupanska, O.I. On the Electrical Resistance of Carbon Fiber Polymer Matrix Composites. *Composites Part A: Applied Science and Manufacturing*, **2010**, *41*, 1719-1727.

138. Timoshenko, S.; Woinowsky-Krieger, S. *Theory of Plates and Shells*, 2nd Edition; McGraw-Hill Book Co., Inc.: New York, 1959.

139. Ventsel, E.; Krauthammer, T. *Thin Plates and Shells: Theory: Analysis, and Applications*, Marcel Dekker, Inc.: New York, 2001.

140. Pan, E.; Han, F. Exact Solution for Functionally Graded and Layered Magneto-Electro-Elastic Plates. *International Journal of Engineering Science*, **2005**, *43*, 321-339.

141. Pan, E.; Heyliger, P.R. Free Vibrations of Simply Supported and Multilayered Magneto-Electro-Elastic Plates. *Journal of Sound and Vibration*, **2002**, *253*, 429-442.

142. Pan, E.; Heyliger, P.R. Exact Solution for Magneto-Electro-Elastic Laminates in Cylindrical Bending. *Journal of Solids and Structures*, **2003**, *40*, 6859-6876.

143. Wang, R.; Han, Q.; Pan, E. An Analytical Solution for a Multilayered Magneto-Electro-Elastic Circular Plate under Simply Supported Lateral Boundary Conditions. *Smart Materials and Structures*, **2010**, *19(6)*, 065025.

144. Zhou H.M.; Xuan L.M.; Li C.; Wei, J. Numerical Simulation of Nonlinear Magnetic-Mechanical-Electric Coupling Effect in Laminated Magnetoelectric Composites. *Journal of Magnetism and Magnetic Materials*, **2011**, *323(22)*, 2802-2807.

145. Jones, R.M. *Mechanics of Composite Materials*, 2nd Edition; Taylor & Frances, Inc.: Ann Arbor, 1998.